CRACK INITIATION AND GROWTH IN SHAPE MEMORY ALLOYS

by

Fatma Mutlu

B.S., Mechanical Engineering, Fırat University, 2009

M.S., Mechanical Engineering, Boğaziçi University, 2016

Submitted to the Institute for Graduate Studies in
Science and Engineering in partial fulfillment of
the requirements for the degree of
Doctor of Philosophy

Graduate Program in Mechanical Engineering

Boğaziçi University

2023

ACKNOWLEDGEMENTS

First and foremost, I am deeply indebted to my supervisor, Prof Günay Anlaş, for his unwavering guidance, patience, and mentorship. His expertise, insightful feedback and constructive criticism have been pivotal in shaping the direction of my research and refining my academic skills. I am profoundly thankful to Prof Hüseyin Şehitoğlu from the University of Illinois at Urbana-Champaign for his mentorship, and for providing the resources, facilities, and academic environment that enabled me to carry out my research effectively.

I would also like to extend my thanks to the members of my thesis committee, Assist Prof Sertan Alkan, Prof Kutay Orakçal, and Prof Ziad Moumni for their insightful comments, suggestions, and time they dedicated to reviewing and evaluating my work.

The High Temperature Materials Laboratory of the University of Illinois at Urbana-Champaign has been a supportive academic environment for me. I am truly grateful for the support from Dr. Sidharth Ravi who has shared his knowledge and experiences on crack growth of shape memory alloys, and has always been there to help me when I needed during the experiments. I appreciate the friendly work environment provided by Orçun Koray Çelebi and Görkem Gengör, and Jad Yaacoub, who helped me with the experiments early in my research.

I extend my heartfelt appreciation to Dr. Gülcan Özerim Bekiloğlu and Hasan Eren Bekiloğlu, my dear friends and colleagues, both within and outside the university. I am truly thankful for their true friendship and presence in my academic and personal life.

My gratitude extends to the faculty of Mechanical Engineering Department at Boğaziçi University, whose dedication to education provided an inspiring environment in which to pursue my studies. I would like to express my thanks to our department

secretaries Seher Yıldız and Özlem Ulufer Oral for always being helpful and for their friendship during my time at the department.

My family deserve my deepest thanks for their unwavering love, encouragement, and patience throughout this academic journey. Their belief in me sustained me through the challenges and motivated me to persevere.

Thank you.

ABSTRACT

CRACK INITIATION AND GROWTH IN SHAPE MEMORY ALLOYS

The aim of this thesis is to study the crack initiation and growth in shape memory alloys (SMAs), with emphasis given to martensitic transformation in front of the crack tip and non-transforming phase interactions along the crack path. In the first part, the effect of phase transformation on the fracture of polycrystalline NiTi SMAs is examined to introduce the complexities encountered in transforming materials. Fracture experiments are conducted at two different loading rates, and crack initiation and growth are monitored: In all samples, the crack starts and grows at a straight angle from the notch. Later, the J-Integral is evaluated experimentally and numerically. At a low loading rate the driving mechanism for resistance to fracture is phase transformation, but at a higher loading rate heat dissipation becomes more prominent due to higher magnitude of latent heat release. In the second part, crack initiation and growth in single-crystal CoNiAl SMAs are investigated using cyclic loading experiments. In crack growth tests, cracks initiate and grow at an angle similar to the martensite band angle of tensile specimens. Crack initiation angles of superelastic CoNiAl samples are calculated analytically and numerically, and the results are found to be in good agreement with the experiments. Stress intensity factors (SIFs) and crack growth rates (da/dN) are calculated for growing cracks, the behavior of which are investigated by examining the test samples with an optical microscope: When non-transforming secondary phase regions are encountered, cracks slow down/stop and SIFs increase/decrease. Overall, it is found that the non-transforming phase acts as a barrier against crack growth and improves the fracture resistance of the SMA. The results of the study underline the importance of including the effects of phase transformation and non-transforming microstructural barriers for a better understanding of the fracture behavior of SMAs.

ÖZET

ŞEKİL HAFIZALI ALAŞIMLARDA ÇATLAK BAŞLAMASI VE BÜYÜMESİ

Bu tezin temel amacı, çatlak ucunun önündeki martensitik dönüşüme ve çatlak yolu boyunca dönüşmeyen faz etkileşimlerine vurgu yaparak, şekil hafızalı alaşımlarda (ŞHA'lar) çatlak başlangıcını ve büyümesini incelemektir. İlk bölümde, faz dönüşümünün polikristalin NiTi ŞHA'ların kırılması üzerindeki etkisi, faz dönüşüm malzemelerinde karşılaşılan karmaşıklıkları tanıtmak için incelenmiştir. Kırılma deneyleri iki farklı yükleme hızında gerçekleştirilir ve çatlak başlangıcı ve büyümesi izlenir: Tüm numunelerde çatlak çentikten düz bir açıyla başlar ve büyür. Daha sonra J-İntegrali deneysel ve ABAQUS ile sayısal olarak değerlendirilmiştir. Düşük yükleme hızında kırılmaya karşı direncin tahrik mekanizması faz dönüşümüdür, ancak daha yüksek yükleme hızında gizli ısı salınımının büyüklüğü nedeniyle ısı yayılımı daha belirgin hale gelir. İkinci bölümde tek kristalli CoNiAl ŞHA'larda çatlak başlangıcı ve büyümesi döngüsel yükleme deneyleriyle incelenmiştir. Çatlak büyüme testlerinde çatlaklar, çekme numunelerinin martenzit bant açısına benzer bir açıyla başlar ve büyür. Süperelastik CoNiAl numunelerinin çatlak başlangıç açıları analitik ve ABAQUS ile sayısal olarak hesaplanır, sonuçlar deneylerle iyi bir uyum içindedir. Büyüyen çatlaklar için gerilim şiddet faktörü (GŞF) ve çatlak büyüme hızı (da/dN) hesaplanır, ve davranışları test numuneleri optik mikroskopla incelenerek araştırılır: Dönüşmeyen ikincil faz bölgeleriyle karşılaşıldığında çatlaklar yavaşlar/durur ve GŞF'ler artar/azalır. Genel olarak, dönüşmeyen fazın çatlak büyümesine karşı bir bariyer görevi gördüğü ve ŞHA'ların kırılma direncini arttırdığı bulunmuştur. Çalışmanın sonuçları, ŞHA'ların kırılma davranışının doğru belirlenmesi için faz dönüşümünden ve dönüşmeyen mikroyapısal bariyerlerden gelen etkilerin dahil edilmesinin öneminin altını çizmektedir.

TABLE OF CONTENTS

ACKNOWLEDGEMENTS . . . iii
ABSTRACT . . . v
ÖZET . . . vi
LIST OF FIGURES . . . x
LIST OF TABLES . . . xvii
LIST OF SYMBOLS . . . xviii
LIST OF ACRONYMS/ABBREVIATIONS . . . xxi
1. INTRODUCTION . . . 1
1.1. Shape Memory Alloys (SMAs) . . . 1
1.1.1. Superelasticity . . . 5
1.1.2. Shape Memory Effect . . . 5
1.2. Single Crystal and Polycrystalline SMAs . . . 6
1.2.1. Single Crystal CoNiAl . . . 7
1.2.2. Polycrystalline NiTi . . . 10
1.3. Fracture of Shape Memory Alloys . . . 12
1.3.1. Experimental Studies . . . 12
1.3.2. Numerical Studies . . . 17
1.4. Motivation of the Study . . . 23
1.5. Outline of the Thesis . . . 25
2. CRACK INITIATION AND GROWTH IN NiTi SHAPE MEMORY ALLOYS 27
2.1. Introduction . . . 27
2.2. Experimental Evaluation of the J-Integral . . . 28
2.2.1. Specimen and Experiments . . . 28
2.2.2. Crack Initiation in NiTi Specimens . . . 29
2.2.3. Evaluation of the Stress Intensity Factors and J-Integrals . . . 31
2.3. Evaluation of the J-Integral Using Finite Elements . . . 36
2.3.1. Finite Elements Model (ABAQUS) . . . 36
2.3.2. Evaluation of the Energy Release Rate . . . 38
2.3.2.1. Stored Energy in Shape Memory Alloys . . . 39

2.3.2.2. Dissipated Energies in Shape Memory Alloys 39
2.3.2.3. $\mathcal{J}$-Integral Calculations 40
2.3.3. J-Integral From ABAQUS, $\mathcal{J}$ 44
2.4. Summary and Conclusions 46
3. CRACK INITIATION ANGLE IN SINGLE CRYSTAL SHAPE MEMORY ALLOYS 50
3.1. Introduction 50
3.2. Experimental Observation of Crack Initiation From the Notch 52
3.2.1. Material and Specimens 52
3.2.2. Experimental Set-up 53
3.2.3. Mechanical Behavior of CoNiAl 54
3.3. Crack Initiation Angle Evaluation 56
3.4. Crack Initiation Angle Calculations 60
3.4.1. Stress Field in Anisotropic Media Around a Crack 62
3.4.2. U-notches 63
3.4.3. Analytical Crack Initiation Angle Calculations 65
3.4.3.1. Generalized Maximum Tangential Stress (GMTS) Criterion 65
3.4.3.2. Maximum Energy Release Rate (MERR) Criterion . . 67
3.4.3.3. Strain Energy Density (SED) Criterion 70
3.4.4. Prediction of the Crack Initiation Angle Using Finite Elements . 73
3.4.4.1. Finite Elements Model 73
3.4.4.2. Tangential Stress Field Around the Notch & Crack . . 75
3.4.4.3. Strain Energy Density Distribution 77
3.4.4.4. Determination of Martensitic Transformation Region . 78
3.4.4.5. Calculation of Energy Release Rate as a Function of Crack Initiation Angle 81
3.5. Summary and Conclusions 83
4. CRACK GROWTH IN SINGLE CRYSTAL SHAPE MEMORY ALLOYS . 85
4.1. Introduction 85
4.2. Digital Image Correlation 86
4.3. Results and Discussion of Crack Growth 89

4.3.1. Superelastic Case 1 89
4.3.2. Superelastic Case 2 95
4.3.3. Shape Memory Case 101
4.4. Summary and Conclusions 107
5. SUMMARY AND CONCLUSIONS 109
REFERENCES 114
APPENDIX A: COPYRIGHTS 135

LIST OF FIGURES

Figure 1.1. Stress-strain behavior of shape memory alloys under low, moderate, and high testing temperatures [1]. 1

Figure 1.2. Martensitic reorientation behavior with loading shown on stress-temperature diagram [2]. 2

Figure 1.3. The effect of testing temperature in stress-strain behavior of shape memory alloys [1]. 3

Figure 1.4. Unloading from detwinned martensite to twinned martensite, and recovery of austenitic phase with heating as shown on stress-temperature diagram [2]. 3

Figure 1.5. Martensitic transformation from austenite to detwinned martensite with loading as shown on stress-temperature diagram at temperatures above A_f [2]. 4

Figure 1.6. CoNiAl crystal structure. (a) B2 austenite, (b) $L1_0$ martensite, where Al atoms are sketched with large black circles, and the blue circles represent the Co-Ni elements. (c) A1 γ-phase structure that consist of Co-Ni-Al elements. 8

Figure 1.7. Cubic–tetragonal lattice correspondences for austenite to martensite transformation. 9

Figure 1.8. Crack interaction with secondary phase particles; from Kumar and Curtin [24]. 10

Figure 1.9. NiTi crystal structure. (a) B2 austenite, (b) B19′ martensite. . . . 11

Figure 2.1. Geometry of the NiTi specimen (all dimensions are in mm). The specimen is loaded by P from the pin holes. 28

Figure 2.2. Crack initiation from the notch in polycrystalline NiTi CT specimen. 30

Figure 2.3. Crack growth in polycrystalline NiTi CT specimen. 30

Figure 2.4. Load vs. Load Line Displacement (LLD) for 0.1 mm/min loading rate. 32

Figure 2.5. Load vs. Load Line Displacement (LLD) for 0.5 mm/min loading rate. 32

Figure 2.6. Load vs. Crack Mouth Opening Displacement (CMOD) for 0.1 mm/min loading rate. 34
Figure 2.7. Load vs. Crack Mouth Opening Displacement (CMOD) for 0.5 mm/min loading rate. 35
Figure 2.8. Mesh, boundary conditions, and loading of the CT specimen finite element model. 37
Figure 2.9. Martensitic transformation region around the crack tip of the 0.1 mm/min loading rate material model. 42
Figure 2.10. Martensitic transformation region around the crack tip of the 0.5 mm/min loading rate material model. 42
Figure 2.11. Temperature field around the crack tip, 0.1 mm/min loading rate (K). 43
Figure 2.12. Temperature field around the crack tip, 0.5 mm/min loading rate (K). 44
Figure 3.1. Sketch of the dog bone specimen used for mechanical behavior determination tests. 53
Figure 3.2. Test set-up. DIC camera, light source, heating tapes, the specimen position, and the temperature control unit. 54
Figure 3.3. Stress–Strain behavior of the superelastic specimen (SE), T= 50 ^oC in tension. The strain is calculated from the mean of ϵ_{yy} extracted from the black framed region. 55
Figure 3.4. Stress – Strain behavior of the shape memory specimen (SM), T= 20 ^oC. The strain is calculated from the mean of the strains, ϵ_{yy}, extracted from the black framed region. 56
Figure 3.5. Edge-notched dog-bone specimen. A 0.5 mm notch is cut at the mid-section. 56
Figure 3.6. Crack initiation in the first superelastic specimen (SE1): Crack length = 0.027 mm. 57
Figure 3.7. Crack initiation in the second superelastic specimen (SE2): Crack length = 0.0246 mm. 58
Figure 3.8. Crack initiation in the third superelastic specimen (SE3): Crack length = 0.073 mm. 58

Figure 3.9. The initial and effective cracks in the shape memory specimen (SM): The effective crack length=0.0358 mm. 59
Figure 3.10. (a) Crack initiation in the first specimen, $\theta_{SE1} \approxeq 43°$; (b) the third specimen, $\theta_{SE3} \approxeq 44°$. (c) Initiation of the first crack in the second specimen, $\theta_{SE2,1} \approxeq -42°$; (d) second crack from the notch in the second specimen, $\theta_{SE2,2} \approxeq 44°$ 60
Figure 3.11. (a) Martensite localization band at $\approxeq 41°$. (b) Sketch of the notch. Material orientation angle $\phi = 41°$, and $\sigma_0 = 85$ MPa. x & y are material coordinates; x' & y' notch configuration coordinates (x' is along the notch). 61
Figure 3.12. Representation of the control volume for critical region ahead of the notch. θ_c is the fracture angle from the notch tip. 64
Figure 3.13. Distribution of tangential stress around the crack tip for anisotropic superelastic material, maximum $\sigma_{\theta\theta}$ occurs at $\theta_c \approxeq 42.3^o$. 66
Figure 3.14. Distribution of tangential stress around the crack tip for anisotropic superelastic material $\theta_c \approxeq 42.3^o$; polar plot. 67
Figure 3.15. Distribution of energy release rates around the crack tip as a function of θ, the maximum occurs at $\theta_c \approxeq 41.6°$. 69
Figure 3.16. Distribution of energy release rates around the crack tip as a function of θ, the maximum occurs at $\theta_c \approxeq 41.6°$; polar plot. 69
Figure 3.17. Distribution of strain energy density around the crack tip for anisotropic superelastic material, maximum occurs at $\theta_c \approxeq 40.9^o$. 72
Figure 3.18. Distribution of strain energy density around the crack tip for anisotropic superelastic material; polar plot. 73
Figure 3.19. Geometry, mesh, and loading of the finite element model. Plane stress assumption. Global and material coordinates presented in Figure 3.11 are used. 74
Figure 3.20. Tangential stress contours around the notched specimen model. Anisotropic superelastic material, maximum occurs at $\theta_c \approxeq 41.3°$. . 75

Figure 3.21. Tangential stress contours. Crack propagation from the pre-crack (a=0.015 mm). Anisotropic superelastic material model, $\theta_c \approxeq 41^\circ$ measured from the crack tip to the maximum point on the stress contour with respect to the global x-direction. 76
Figure 3.22. Tangential stress contours around the notch. Isotropic superelastic material model, $\theta_c = 0^\circ$. 77
Figure 3.23. Strain energy density (SENER) around the notch. Anisotropic superelastic material model, $\theta_c \approxeq 38^\circ$. 78
Figure 3.24. Equivalent strain contours around the notch. Anisotropic superelastic material model. 79
Figure 3.25. Equivalent strain contours around the pre-crack and the notch. Anisotropic superelastic material model. 80
Figure 3.26. Martensite transformation contours (MVF) around the notch. Anisotropic superelastic material model. 80
Figure 3.27. Martensite transformation contours (MVF) contours around the pre-crack and the notch. Anisotropic superelastic material model. 81
Figure 3.28. Distribution of energy release rate around the crack tip for anisotropic superelastic material obtained from finite elements analyses. Maximum of $\mathcal{G}$ is found at angle $\theta_c \approxeq 41.2^\circ$. 82
Figure 3.29. Martensite band angle in the tension specimen and a crack emanating from the notch, which have approximately the same angle, ϕ. 83
Figure 4.1. Crack tip configuration presented in polar coordinates. 87
Figure 4.2. Effective stress intensity factor vs. crack length after crack initiation (SE1). Corresponding crack growth rates (da/dN) are given in 10^{-8} m/cycle. Numbers in parentheses correspond to the effective crack in the crack growth sequence in Figure 4.3. 89
Figure 4.3. Sketch of crack growth path from the notch (SE1). Numbers indicate sequences of crack growth. The γ-phase region around the notch is shown by the dashed line. The specimen fails at $\approx$ 36000 cycles. 90

Figure 4.4. Crack initiation and following advancement in the first superelastic specimen (SE1). (a) DIC image showing kinking in the crack growth direction ("1" → "1′" → "1″"). (b) New crack forms ("2"). (c)"1″" and "2" advance. 91

Figure 4.5. Effective stress intensity factor vs. crack length (SE1). Corresponding crack growth rates (da/dN) are given in 10^{-8} m/cycle. Numbers in parentheses correspond to the effective crack in the crack growth sequence in Figure 4.3. 92

Figure 4.6. Optical microscopy image of the specimen SE1 taken after failure showing the cracks "1″" and "2" merging at "3". γ-phase borders are shown with black dashed lines. Inset shows the ruptured specimen and the area to which the microscopic image corresponds. 93

Figure 4.7. Cracks stop at γ-phase boundaries. Inset shows the ruptured specimen and the area to which the microscopic image corresponds (SE1). Numbers correspond to the effective crack in the crack growth sequence given in Figure 4.3. 93

Figure 4.8. Microscopic images around the ruptured notch showing γ-phase (SE1). (a) The top with γ-phase thickness of $\approx 12\mu m$, (b) the bottom with $\approx 11\mu m$ thickness."i" indicates crack initiation inside γ-phase, and "1" corresponds to the first crack in Figure 4.3. . . . 94

Figure 4.9. Sketch of the crack advancement (SE2): Cracks initiate and advance from the notch as shown. Dotted line around the notch shows the γ-phase region. The specimen fails from the "second crack" when the crack length is 0.095 mm, and 1664 cycles after crack the initiation. 95

Figure 4.10. Effective stress intensity factor vs. crack length (SE2). Corresponding crack growth rates (da/dN) are given in 10^{-8} m/cycle. Results are for the main crack obtained from the area (AOI) that is shown in Figure 4.11. 96

Figure 4.11. DIC image just before failure (SE2). Inset shows the DIC image of the second crack after failure. 97

Figure 4.12. Optical microscopy of the main crack (SE2). γ-phase borders at the notch are shown with black dashed lines. Inset shows the ruptured specimen, and the area to which the microscopic image corresponds. 97

Figure 4.13. Equivalent strain (ϵ_{eq}) plots around the main crack tip after the crack stops (SE2). (a) Just after crack stops, (b) $\approx$ 300 cycles after crack stops. Results are obtained from the AOI in Figure 4.11. . . 98

Figure 4.14. Crack initiation at the notch (SE2). (a) Second crack, (b) main crack. Inset shows the areas which correspond to the microscopic images are taken. 99

Figure 4.15. Sketch of the growth path of the effective crack (SM): Numbers indicate the sequences of crack advancement. Dotted line around the notch shows the γ-phase region. The specimen fails after $\approx$ 24000 cycles when the crack length increases to $\approx$ 0.8 mm. 101

Figure 4.16. Effective stress intensity factor vs. crack length after crack initiation (SM). Corresponding crack growth rates (da/dN) are given in 10^{-8} m/cycle. Numbers in parentheses correspond to the crack growth sequences of the effective crack in Figure 4.15. 102

Figure 4.17. Optical microscopy images around the ruptured notch (a) the top, (b) the bottom (SM). Inset shows the ruptured specimen and the areas to which the microscopic images correspond. 103

Figure 4.18. Crack growth in the shape memory specimen (SM). (a) DIC image showing a new crack formation ("8"). (b) The main crack and the new crack merge. 104

Figure 4.19. Crack growth in the shape memory specimen (SM). Optical microscopy image taken around the two cracks ("5" and "8") that merge at "9" and"10": (a) The top, (b) the bottom part of the ruptured specimen. γ-phase borders are shown with black dashed lines. Inset shows the ruptured specimen and the area to which the microscopic images corresponds. 104

Figure 4.20. Effective stress intensity factor vs. crack length (SM). Corresponding crack growth rates (da/dN) are given in 10^{-8} m/cycle. Numbers in parentheses correspond to the crack growth sequences of the effective crack in Figure 4.15. 105
Figure 4.21. (a) Vertical displacement contours corresponding to Figure 4.18-(a), (b) to Figure 4.18-(b) (full lines: u_y from Equation. 4.2, dotted lines: DIC)(SM). 106
Figure 4.22. (a) ϵ_{yy} contours corresponding to Figure 4.18-(a), and (b) to Figure 4.18-(b), respectively (SM). 106
Figure A.1. Proof of permission for reuse of Figure 1.1 135
Figure A.2. Proof of permission for reuse of Figure 1.3 136
Figure A.3. Proof of permission for reuse of Figure 1.2 and 1.4 137
Figure A.4. Proof of permission for reuse of Figure 1.5 138
Figure A.5. Proof of permission for reuse of Figure 1.8 139

LIST OF TABLES

Table 2.1. Maximum Load & Displacement data from Load-Displacement curves and COD gauge, with a_0: the initial crack lengths. 29

Table 2.2. J-Integrals and stress intensity factors calculated using the load line displacement. 33

Table 2.3. J-Integrals and stress intensity factors calculated using the crack mouth opening displacement obtained from the COD gauge. 34

Table 2.4. NiTi finite element model material properties for the 0.1 mm/min loading rate experiment [42]. 37

Table 2.5. NiTi finite element model material properties for the 0.5 mm/min loading rate experiment [42]. 38

Table 2.6. Energy release rates calculated from FE results accounting for the stored and dissipated energies that affect crack growth. 41

Table 2.7. The far field (austenitic region) $\mathcal{J}$-Integrals obtained from ABAQUS. 46

Table 2.8. J-Integrals calculated from Load-Displacement curves in Figures 2.4, 2.5, 2.6 & 2.7, and the J-Integral test software results (J_{E1820}). 47

Table 2.9. Energy release rates, ($\frac{\Delta U}{\Delta A}$), calculated from finite elements, and the far field $\mathcal{J}$-Integral from ABAQUS. 47

Table 3.1. Compliance matrix components in material coordinates. 62

Table 3.2. Finite element model material properties of the CoNiAl SMA. . . . 74

Table 3.3. Comparison of critical crack initiation/growth angles from experiments and finite element analyses ($\approxeq \theta_c^\circ$). 84

Table 4.1. Compliance components calculated using Equations (4.1)-(4.5). DIC data are obtained from the area (AOI) in Figure 4.11. 100

LIST OF SYMBOLS

a	Crack Length
a_0	Initial Notch Length
a_{ij}	Compliance Matrix Components
A	Austenite
$A1$	Face Centered Cubic
A_1, B_u, B_v	Rigid Body Rotation/Translation Parameters
A_f	Austenite Finish Temperature
A_s	Austenite Start Temperature
B, B_N	Specimen Thickness
b_0	Uncracked Ligament Length
$B2$	Body Centered Cubic
$C_A, (\frac{\delta\sigma}{\delta T})_L$	Clausius - Clapeyron Constant for Austenite
$C_M, (\frac{\delta\sigma}{\delta T})_U$	Clausius - Clapeyron Constant for Martensite
E	Young's Modulus
E_A	Young's Modulus of Austenite
E_M	Young's Modulus of Martensite
$\mathcal{G}$	Energy Release Rate
Im	Imaginary Part of a Complex Number
J_{dis}	Dissipation Component of J-Integral
J_{el}	Elastic Component of J-Integral
$\mathcal{J}$	$\mathcal{J}-$Integral
K	Stress Intensity Factor
K_c	Fracture Toughness
K_I	Mode-I Stress Intensity Factor
K_{Ic}	Mode-I Critical Stress Intensity Factor
K_{II}	Mode-II Stress Intensity Factor
K_{eff}	Effective Stress Intensity Factor
K_Q	Mode-I Critical Stress Intensity Factor for Plane Strain
$k^{(k)}$	Stress Intensity Factor Vector in Kink Coordinates

L	Elastic Material Property Tensor
$L1_0$	Face Centered Tetragonal
M	Martensite
M_d	Martensite Desist Temperature
M_f	Martensite Finish Temperature
M_s	Martensite Start Temperature
P_{max}	Maximum Applied Load
P_Q	Critical Load
$q,\ r_0$	Notch Geometry Parameters
r	Radial Polar Coordinate
Re	Real Part of a Complex Number
S	Strain Energy Density Factor
s_i	Material Parameters in Crack Configuration
S_{ij}	Compliance Matrix Components in Kink Coordinates
t	Specimen Thickness
T	Temperature
T_0	Ambient Temperature
$T-$stress	Stress Component Parallel to the Crack Plane
u, u_x	Displacement Component in x-Direction
U_Q	Heat Dissipation Energy
U_{SE}	Elastic Strain Energy
U_{tr}	Transformation Energy
v, u_y	Displacement Component in y-Direction
w	Elastic Strain Energy Density
W	Specimen Width
W_{ext}	Work of External Forces
W_s	Fracture Work
χ	U-notch Parameter
ϵ_{eqv}	Equivalent Strain
ϵ_{MF}	Martensite Transformation Finish Strain

ϵ_{MS}	Martensite Transformation Start Strain
$\epsilon_{xx}, \epsilon_{yy}, \epsilon_{xy}$	Strain Field Components in Cartesian Coordinates
$\epsilon_{rr}, \epsilon_{\theta\theta}, \epsilon_{r\theta}$	Strain Field Components in Cylindrical Coordinates
ϕ	Material Orientation Angle
γ	Notch Opening Angle
Γ	Contour Around the Crack Tip
λ	Mode Mixity Parameter
Λ	U-Notch Parameter
μ_i	Material Parameters in Material Configuration
ν	Poisson's Ratio
ν_A	Austenite Poisson's Ratio
ν_M	Martensite Poisson's Ratio
Π	Potential Energy
ρ_0	Notch Radius
σ_{AF}	Austenite Transformation Finish Stress
σ_{AS}	Austenite Transformation Start Stress
σ_{MF}	Martensite Transformation Finish Stress
σ_{MS}	Martensite Transformation Start Stress
σ_{ORI}^{f}	Martensite Reorientation Finish Stress
σ_{ORI}^{s}	Martensite Reorientation Start Stress
σ_{UTS}	Ultimate Tensile Strength
σ_{YS}^{M}	Martensite Yield Stress
$\sigma_{xx}, \sigma_{yy}, \sigma_{zz}$	Principal Stress Field Components in Cartesian Coordinates
$\sigma_{rr}, \sigma_{\theta\theta}, \sigma_{zz}$	Principal Stress Field Components in Cylindrical Coordinates
$\sigma_{xy}, \tau_{xz}, \tau_{yz}$	Shear Stresses in Cartesian Coordinates
$\sigma_{r\theta}, \tau_{rz}, \tau_{\theta z}$	Shear Stresses in Cylindrical Coordinates
θ	Angular Polar Coordinate
θ_c	Critical Crack Initiation Angle

LIST OF ACRONYMS/ABBREVIATIONS

AOI	Area of Interest
ASTM	American Society for Testing and Material
BCC	Body Centered Cubic
CCD	Charge Coupled Device
CoNiAl	Cobalt Nickel Aluminum
CT	Compact Tension
CMOD	Crack Mouth Opening Displacement
COD	Crack Opening Displacement
CTOD	Crack Tip Opening Displacement
DIC	Digital Image Correlation
DSC	Differential Scanning Calorimetry
EDM	Electrical Discharge Machining
FCC	Face Centered Cubic
FCM	Face Centered Monoclinic
FCT	Face Centered Tetragonal
Fe-SMAs	Iron-based Shape Memory Alloys
FSMA	Ferromagnetic Shape Memory Alloys
FE	Finite Elements
FEA	Finite Element Analysis
FEM	Finite Element Method
GMTS	Generalized Maximum Tangential Stress
LEFM	Linear Elastic Fracture Mechanics
LLD	Load Line Displacement
MERR	Maximum Energy Release Rate
MSED	Maximum Strain Energy Density
MTS	Maximum Tangential Stress
MVF	Martensite Volume Fraction
NiTi	Nickel Titanium
NOL	Naval Ordinance Laboratory

NSIF	Notch Stress Intensity Factor
SE	Super Elasticity/Elastic
SED	Strain Energy Density
SIF	Stress Intensity Factor
SIM	Stress Induced Martensite
SM	Shape Memory
SMA	Shape Memory Alloy
SME	Shape Memory Effect
TWSME	Two Way Shape Memory Effect
UMAT	User Defined Material Subroutine

1. INTRODUCTION

1.1. Shape Memory Alloys (SMAs)

Shape Memory Alloys (SMAs) are smart materials that can withstand large deformations through solid-to-solid diffusionless martensitic transformation & reorientation. Upon an application of loading at a certain temperature, the SMA deforms, then returns to its' original shape with removal of the load which is known as Superelasticity (SE). The Shape Memory Effect (SME) occurs at a constant loading with a change in temperature.

Temperature plays a significant role in shape memory effect and superelasticity behavior. Once the temperature range for SME and SE is exceeded, the ability for shape recovery is lost and only the deformation via slip is possible, no martensitic transformation nor reorientation will occur. In Figure 1.1, the effect of test temperature on stress-strain behavior of shape memory alloys are illustrated [1].

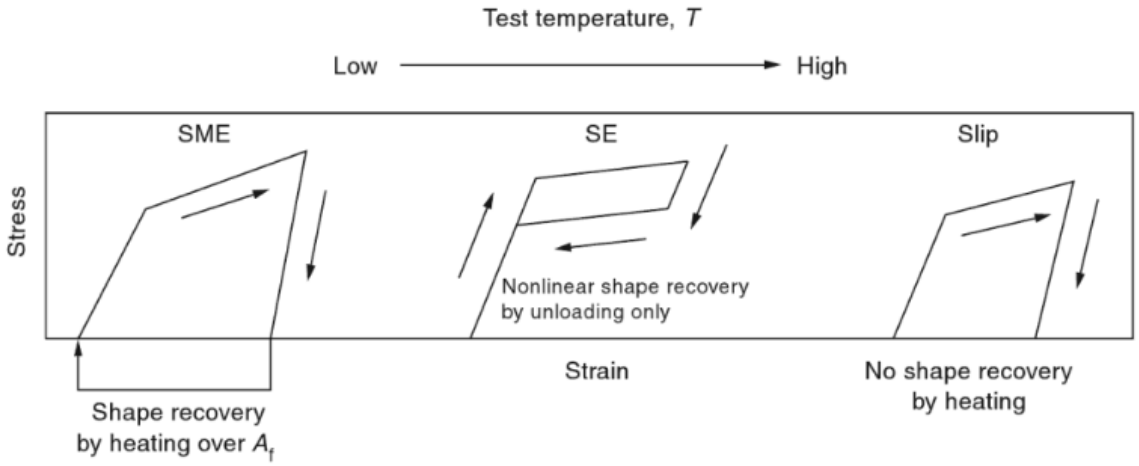

Figure 1.1. Stress-strain behavior of shape memory alloys under low, moderate, and high testing temperatures [1].

There are two crystallographic phases that can be observed in shape memory alloys: the martensitic phase and the austenitic phase. These phases are temperature-dependent and each one has unique thermal transition temperatures: martensite start (M_s), martensite finish (M_f), austenite start (A_s), and austenite finish (A_f) temperature. The test temperature range (T) the material is in, determines the crystallographic phase, and the respective deformation behavior under loading. The crystallographic phase is martensite when the test temperature is lower than the martensite finish temperature ($T < M_f$), between the martensite finish and martensite start ($M_f < T < M_s$), and higher than the martensite start but lower than the austenite start temperature ($M_s < T < A_s$). In these temperature ranges, deformation occurs via the shape memory effect phenomenon and the initial twinned martensite phase undergoes martensitic re-orientation into detwinned martensite with applied loading (see Figure 1.2). The initial shape can be recovered with application of heating above austenite finish temperature. This behavior is shown on stress-strain diagrams in Figures 1.3 (a), (b), and (c) and on stress-temperature diagram in Figure 1.4.

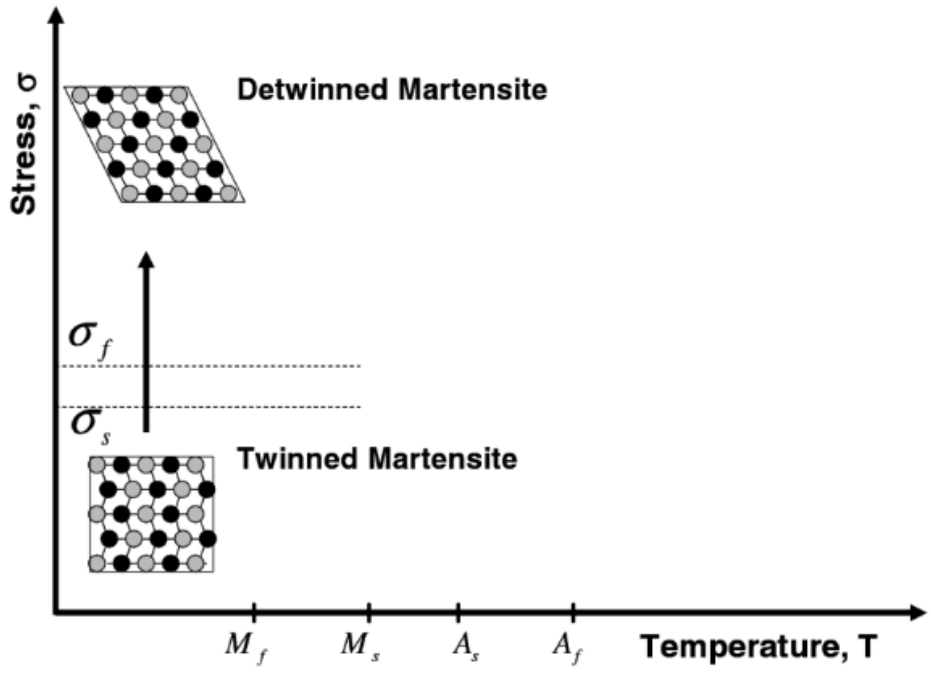

Figure 1.2. Martensitic reorientation behavior with loading shown on stress-temperature diagram [2].

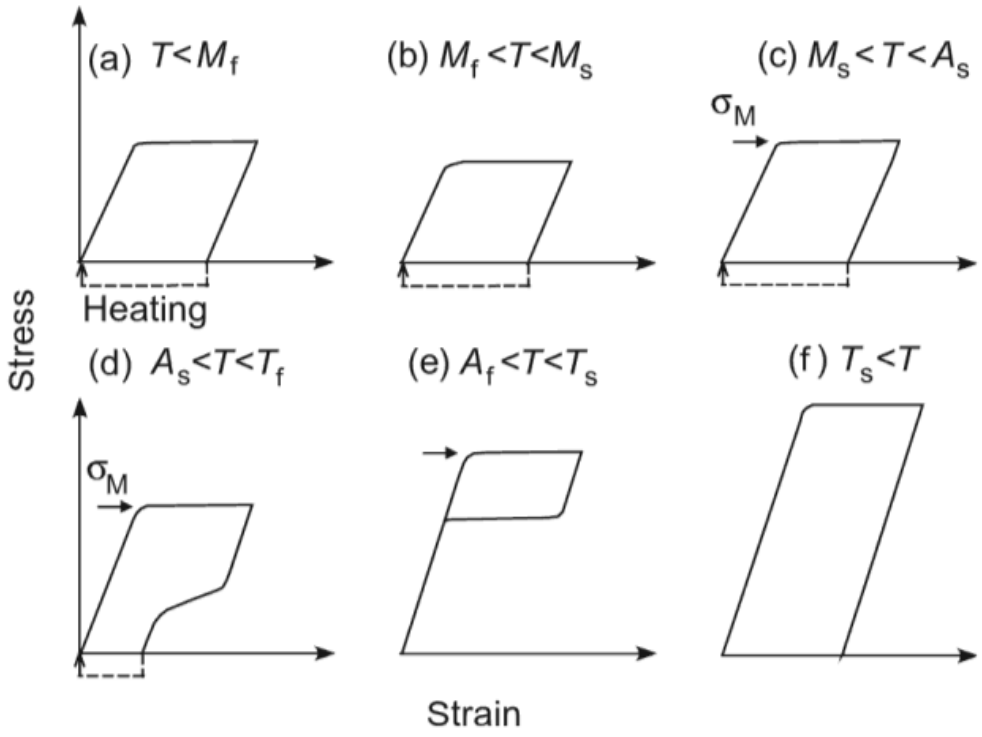

Figure 1.3. The effect of testing temperature in stress-strain behavior of shape memory alloys [1].

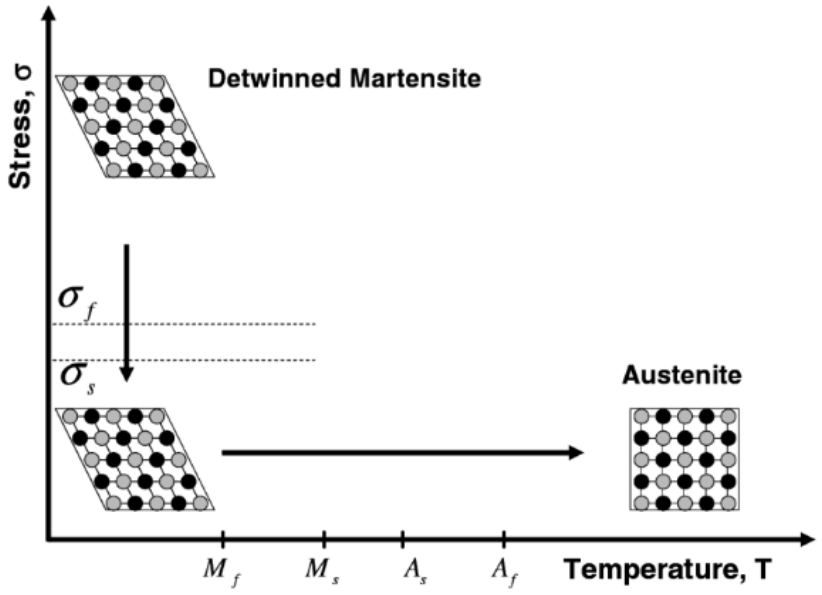

Figure 1.4. Unloading from detwinned martensite to twinned martensite, and recovery of austenitic phase with heating as shown on stress-temperature diagram [2].

When the test temperature is in the range $A_s < T < A_f$, both the martensitic and austenitic crystallographic phases may occur simultaneously, and both martensitic reorientation and austenite to martensite transformation occur under loading. The austenite phase can be obtained partially via superelasticity upon release of loading, and with heating (see Figure 1.3 (d)).

Perfect shape recovery is obtained in the temperature range, $A_f < T < M_d$ (where M_d –or T_s as defined by [1]– is known as the martensite desist temperature, above temperatures of which austenite is the stable phase, and martensite transformation is not possible) with the release of loading as shown in Figure 1.3 (e). In this case, the initial crystallographic phase is austenite, which transforms to detwinned martensite with loading and reverts back to austenite upon release of load (see the stress-temperature diagram presented in Figure 1.5 for loading condition at temperatures above the A_f temperature).

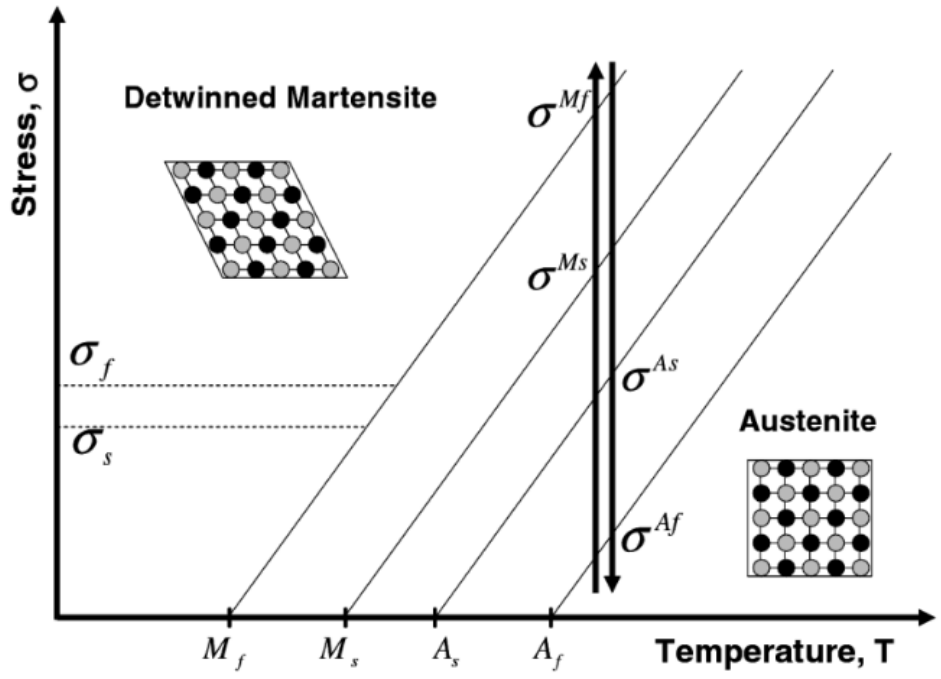

Figure 1.5. Martensitic transformation from austenite to detwinned martensite with loading as shown on stress-temperature diagram at temperatures above A_f [2].

Finally, when the testing temperature is higher than the martensite desist temperature ($M_d < T$), as presented in Figure 1.3 (f), the material undergoes plastic deformation and the initial shape cannot be recovered either through unloading or with application of heat.

1.1.1. Superelasticity

Superelasticity is one of the most interesting capabilities of SMAs which gives them the ability to undergo large strains as large as 20% without plasticity. Superelasticity, or pseudoelasticity (PE) is the term that is used to define the shape memory alloys' ability to deform up to very high strains when loaded, which can return to 0% strain upon the release of loading.

Superelastic shape memory alloys are in the austenitic phase at temperatures higher than the austenite finish temperature (A_f). The superelastic deformation occurs with the material undergoing solid-to-solid transformation from austenite to martensite phase. Transformation from austenite to martensite, which is also known as the forward transformation, starts when the martensite start stress (σ_{MS}) is reached, and the martensitic volume in the material gradually increases. This increase continues until stress value reaches the martensite finish stress (σ_{MF}), thereafter the phase of the material becomes purely martensitic, and the deformation continues elastically. Further loading past the yield stress of martensite (σ_{YS}^{M}) results in plastic deformation. If the load is released before reaching martensite yield stress, the material starts transforming back to austenite with the decrease of stress down to austenite start stress (σ_{AS}), and becomes fully austenitic after passing the austenite finish stress (σ_{AF}). Martensite to austenite transformation mechanism is also known as the reverse transformation.

1.1.2. Shape Memory Effect

Shape memory effect is the mechanism that is known to allow the recovery from the deformation upon application of external heat. Shape memory alloys with SME capabilities can undergo large strains, and return to 0% strain upon heating.

The shape memory alloy with SME is in the martensitic phase before the application of loading. It transforms to twinned martensitic phase when cooled down to a temperature lower than the martensite finish temperature (M_f). When it is loaded, initially it deforms in the elastic region until reaching the martensite reorientation start stress (σ^s_{ORI}), after which the twinned martensite starts to transform to the detwinned martensite and when the stress reaches the martensite reorientation finish stress (σ^f_{ORI}), the phase is completely detwinned martensite. However, in this case, with unloading before yield stress, a transformation back to initial shape cannot be obtained. Only the elastic detwinned martensite strain is recovered, and the material stays deformed; the residual strain can be recovered upon heating. Since the martensitic phase is not stable at high temperatures, heating over austenite finish temperature transforms the martensite back to austenite, and the strain is recovered.

1.2. Single Crystal and Polycrystalline SMAs

After shape memory alloys' discovery in the 1930s, many variants with different constituent elements with various combinations of them have been developed to obtain cost efficiency, increase their practicability, larger shape recovery capabilities, etc.

Initial attempts were focused on shape memory and superelasticity behaviors. However, later researchers turned their attention to the microstructural properties of the shape memory alloys. It was found that the SMAs with large grain sizes are more inclined to cracking, and have poor fracture toughness, which improves with decreasing grain sizes. This behavior is attributed to the grain boundaries which provides the crack an easier propagation path. To circumvent the influence of grain boundaries, single crystal shape memory alloys were produced, which proved to have better mechanical and fracture behaviors.

Single crystal shape memory alloys have superior fracture properties to polycrystals, but this superiority is highly dependent on the crystal orientation, and constituent alloying elements. Single crystal SMAs have varying properties with respect to the loading direction orientation, which may result in increased ductility or brittleness.

In this work, both polycrystalline and single crystal shape memory alloys are studied on the example materials of Nickel-Titanium (NiTi) and Cobalt-Nickel-Aluminum (CoNiAl), respectively. In Sections 1.2.1 and 1.2.2, the materials used in this study are discussed.

1.2.1. Single Crystal CoNiAl

CoNiAl alloys belong to the category of ferromagnetic shape memory alloys (FSMAs), in addition to superelasticity and shape memory properties, they have ferromagnetism capabilities, that is, martensitic reorientation can be achieved under the effect of a magnetic field. CoNiAl FSMAs are one of the preferred materials for the investigations of this study. However, ferromagnetism is not within the scope of this study, so discussions on the details and properties of ferromagnetic transformation will be skipped.

CoNiAl SMAs have substantial potential for actuator applications owing to their fast actuation times, large recoverable strains, wide superelastic windows, small hysteresis, high temperature recoverability [3–6], and when compared to several other shape memory alloys, have considerable cost efficiency and better mechanical properties [5].

An important property of CoNiAl is that the transformation temperatures, A_s (Austenite start), M_s (Martensite start), A_f (Austenite finish), and M_f (Martensite finish) can be changed with heat treatment and also with changing the composition of the constitutive elements Co and Al, that the latter can vary from 20 to 30 at.% [6–10], so that one can obtain superelastic behavior at room temperature [9]. Also it was reported that the volume change of CoNiAl is substantially higher during transformation than traditional shape memory materials [4, 11].

Polycrystalline CoNiAl alloys are brittle and inclined to develop intergranular fracture while the single crystal CoNiAl have exceptional shape memory properties [12]. Single crystal CoNiAl alloys are reported to have superelastic tensile strains as high as

8% [9] and show better strain recovery when compared with the polycrystals and multi-crystals [5]. The [001] orientation has the least number of available slip systems than other orientations which results in harder slip activation [4, 5, 9]. The insufficiency of dislocation due to harder activation of slip systems might delay phase transformation, but provide almost perfect pseudo-elasticity and lower residual strains than any other orientation in single crystal CoNiAl SMAs [13].

CoNiAl shape memory alloys have a narrow thermal hysteresis which is less than 30°C, and an unusually large pseudoelastic window that martensite desist (M_d) to austenite finish (A_f) temperature differential is significantly high (> 100°C) which depends on the composition and heat treatment [3, 4, 13–15]. A recent work on [100] oriented $Co_{35}Ni_{35}Al_{30}$ single crystals showed a superelastic temperature range around 265 °C [16]. In CoNiAl, martensitic transformation occurs from body centered cubic (BCC) austenite to face centered tetragonal (FCT) martensite. Heat treatment in these alloys results in formation of a secondary phase, which has disordered face centered cubic (FCC) structured particles. BCC, FCT [4], and FCC crystal structures in this type of SMAs are sketched in Figure 1.6. Cubic to tetragonal deformation is accommodated by multiple martensite variants through three lattice correspondences as shown in Figure 1.7 [17].

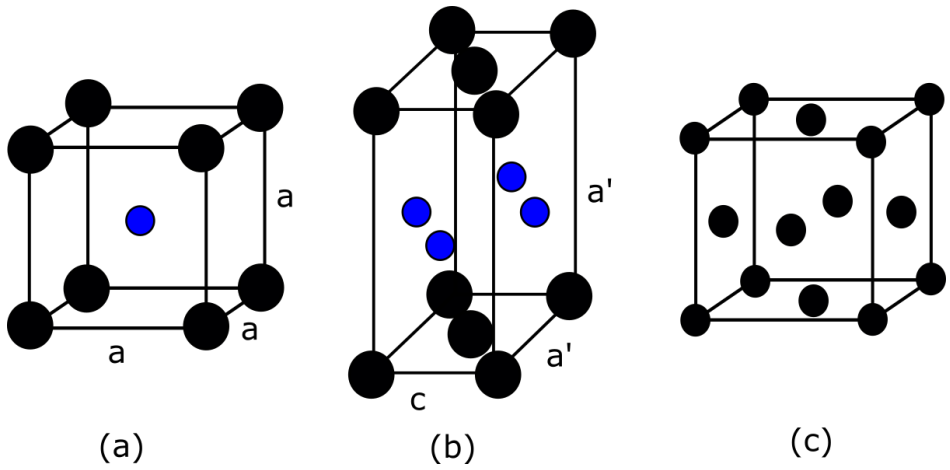

Figure 1.6. CoNiAl crystal structure. (a) B2 austenite, (b) $L1_0$ martensite, where Al atoms are sketched with large black circles, and the blue circles represent the Co-Ni elements. (c) A1 γ-phase structure that consist of Co-Ni-Al elements.

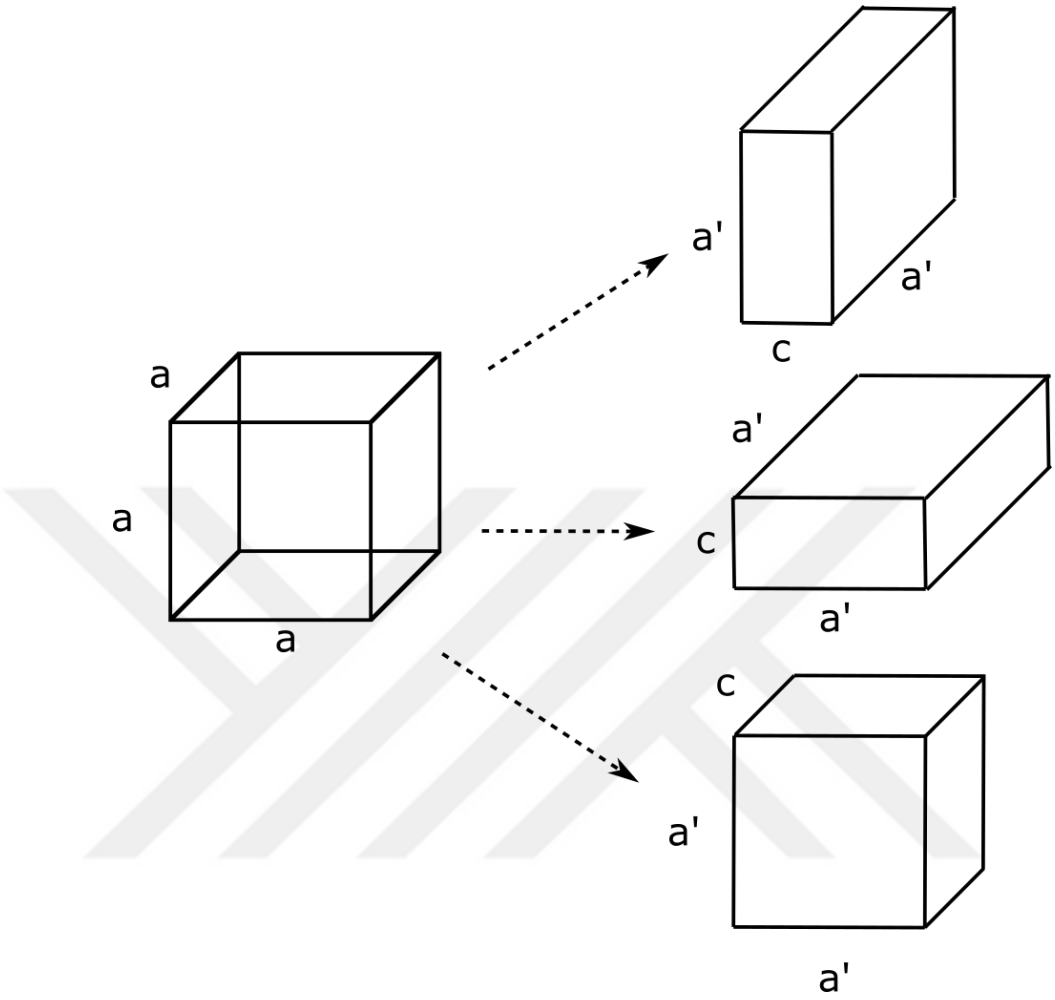

Figure 1.7. Cubic–tetragonal lattice correspondences for austenite to martensite transformation.

Works on polycrystalline and single crystals with various directions report the presence of a secondary phase (γ-phase) [6, 18–20]. Presence of γ-phase increases the resistance to fracture that results in large tensile transformation strains, and raises the ductility, but does not undergo forward martensitic transformation [3, 6–9, 18–21]. Volume fraction of the secondary phase (γ-phase), which is dependent on the annealing temperature and duration, affects the tensile strength, elongation, superelastic properties and shape memory strain recovery of the alloy [6, 22]. These advantages of two-phase CoNiAl alloys give them significant consideration for shape memory alloy applications [6].

Similar crack growth behavior is expected for all crystallographic orientations of CoNiAl SMAs. However, the stress intensity factors and crack growth rates might differ since single crystal CoNiAl SMAs' behavior has a strong crystallographic orientation dependence [14, 23].

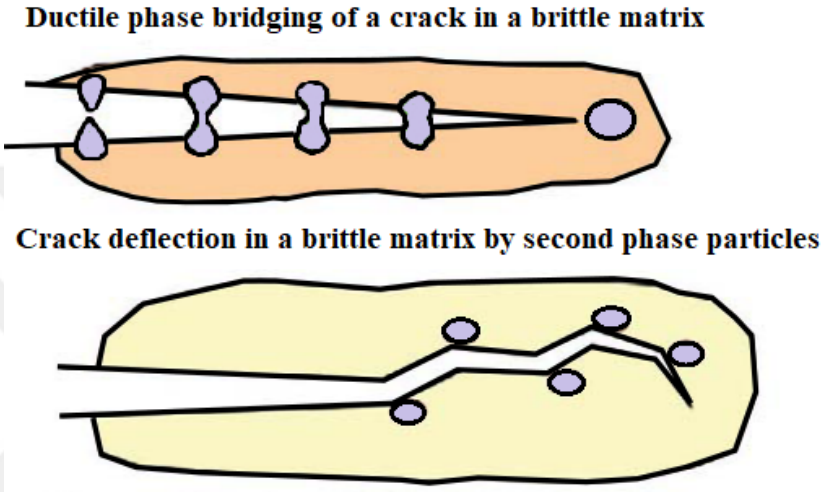

Figure 1.8. Crack interaction with secondary phase particles; from Kumar and Curtin [24].

When the γ-phase size is small relative to the crack length, the crack either cuts through or bends around the γ-phase region, which depends on the stress distribution at the crack tip. If the γ-phase is large, it fatigues and eventually breaks after sufficient cyclic loading. In their review paper on crack interactions with local microstructures, Kumar and Curtin [24] explain the mechanisms that are caused by crack-ductile secondary phase interactions. As seen in Figure 1.8, ductile secondary phases can stop and deflect a growing crack (sketch at the bottom), or the crack can cut through the secondary phases (sketch at the top).

1.2.2. Polycrystalline NiTi

Nickel-Titanium (NiTi), also known as NiTi-NOL, was discovered by the U.S. Naval Ordnance Laboratory (-NOL) in 1963, then attracted great attention and became

one of the most studied SMAs in engineering and medicine fields owing to its curious behavior under stress & heat. NiTi SMAs have been considered for use in medical applications such as stents and implants due to their high corrosion & wear resistance, bio-compatibility properties, and consequently have become the most commercially available ones.

Atomic composition of Nickel-Titanium has an effect on the phase transition temperatures of the NiTi SMAs. With an increase in the Ni concentration larger than 50 at.% in the alloy, the martensite start (M_s) and additionally the A_s, A_f, M_f transformation temperatures and also the thermal hysteresis width of martensitic transformation decrease [25].

In the equiatomic NiTi SMAs, the martensitic transformation occurs from B2 cubic austenite to B19′ monoclinic martensite structure. Crystal structures in this type of SMAs are sketched in Figure 1.9 [26].

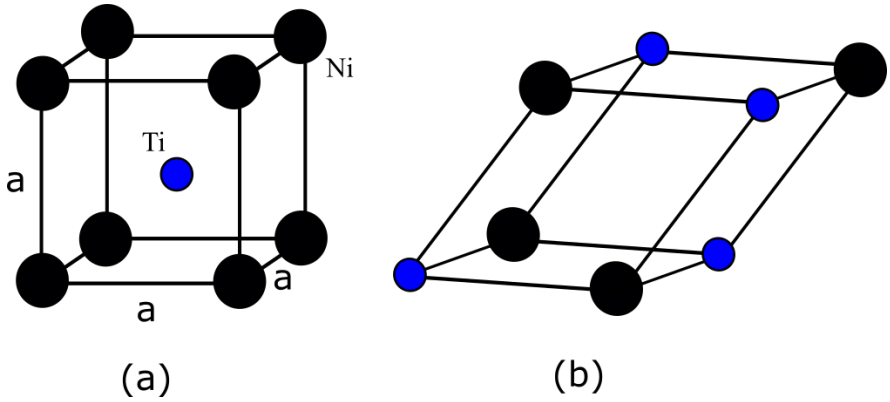

Figure 1.9. NiTi crystal structure. (a) B2 austenite, (b) B19′ martensite.

It is possible to manipulate the mechanical and material characteristics of NiTi-based shape memory alloys by adding different alloying elements. Some examples that give advantageous shape memory effect, low stress hysteresis, wide temperature hysteresis, or high transformation temperatures to the alloys are the addition of copper (Cu), iron (Fe), chromium (Cr), palladium (Pd), platinum (Pt), hafnium (Hf), nio-

bium (Nb), cobalt (Co), zirconium (Zr) etc. usually with the expense of nickel atomic concentration [27, 28].

1.3. Fracture of Shape Memory Alloys

Minor differences in manufacturing processes such as the percentage of alloying components, heat treatment procedures, microstructural properties make substantial changes in the mechanical and fracture behavior of SMAs, the latter of which has gained more concern due to its potential to result in catastrophic failure. Many researchers studied the fracture behavior of shape memory alloys under different conditions. In the following Sections 1.3.1 and 1.3.2, a literature review will be given on experimental and numerical works on the fracture of shape memory alloys reported to date.

1.3.1. Experimental Studies

In their study, Mc Kelvey and Ritchie [29] analyzed the fatigue crack growth characteristics of superelastic NiTiNOL specimens. According to their report, NiTi exhibited the weakest resistance to fatigue crack growth in comparison to other biomedical implant alloys.

Daly *et al.* [30] examined the fracture characteristics of thin NiTi sheets when subjected to Mode I loading. They utilized the digital image correlation (DIC) method to determine the strain fields on the specimen surface and computed the stress intensity factor (SIF) using linear elastic fracture mechanics (LEFM). Additionally, they established a correlation between the size of the phase transformation area and the SIF. Their findings suggest that the phase transformation process increases the resistance to fracture near the crack tip, leading to an overall toughening effect.

Robertson *et al.* [31] utilized X-ray diffraction to analyze the strain field near the edge-cracked NiTi specimens' crack tip. Their findings revealed that stress levels around the crack tip decrease as a result of phase transformation, leading to an improvement in the fracture toughness.

In a study by Jiang *et al.* [32], four-point bending fracture tests were conducted under both dynamic and quasi-static loading conditions. Their findings revealed distinct fracture mechanisms for each scenario. It was noted that the fracture toughness of NiTi SMA increased as the loading rate increased. Two possible explanations for this difference were proposed. Firstly, under dynamic loading, the material's phase at fracture was found to differ from that observed in quasi-static loading. Secondly, the loading rate appeared to impact the mechanical behavior of austenite, making it more ductile and stronger during dynamic loading conditions. As a result, the material's fracture toughness increased compared to quasi-static loading.

Wang *et al.* [33] conducted an experiment to determine the fracture toughness. They used compact tension (CT) specimens with pre-existing fatigue cracks and calculated the stress intensity factor. Their findings revealed that during fatigue cracking, a small area around the crack tip partially transforms into martensite. Furthermore, they noted that if the crack growth is rapid, the small area around the tip of the crack always transforms entirely into martensite.

In their experiments, Gollerthan *et al.* [34] utilized NiTi CT specimens and determined the critical stress intensity factor, K_Q, by applying the empirical formulas provided in the ASTM E399 document [35]. By integrating K_Q with Irwin's plasticity corrected equation, they were able to accurately estimate the extent of the phase transformation zone at the tip of the crack. Their observations revealed a high degree of agreement between the two.

In a study conducted by Gloanec *et al.* [36] , the crack initiation and propagation mechanism of polycrystalline TiNi shape memory alloys was investigated through low cycle fatigue tests on cylindrical rods. According to their report, micro cracks were found to initiate and propagate from the interfaces between martensite-martensite or austenite-martensite phases.

In their work, Maletta *et al.* [37] reported the fracture behavior of shape memory alloys under the effect of temperature. They performed fracture experiments on

single edge cracked superelastic NiTi specimens under three different testing temperatures. They reported in contrary to the previous works that martensitic transformation around the crack tip does not result in a toughening on the fracture behavior. Their stress intensity factor results from experiments obtained via DIC and analytically calculated ones were in good agreement. Additionally, in the testing temperature range of their experiments, they found increasing temperature does not effect the fracture toughness, and the fracture parameters are independent of the temperature changes.

Ungár *et al.* [38] studied the contributions from martensitic transformation and plastic deformation to fracture of superelastic NiTi SMAs. They conducted crack propagation tests and examined the fracture surface with x-ray diffraction. They found a plastic zone close to the fatigue pre-crack, and residual martensite phase that did not transform back to austenite after unloading, limited to a few grains in a very small region. Additionally, they report that residual martensite is also dependent on crack growth rate: At static loading and stable crack growth, amount of residual martensite increases; while at higher growth rates during unstable crack growth, martensitic transformation is hindered, so a smaller amount of residual martensite is found.

Katanchi *et al.* [39] conducted standard fracture tests on Compact Tension (CT) specimens at different mixed mode loading conditions. They calculated the mixed mode fracture toughness of NiTi for loading angles of 0 to 90° degrees experimentally and numerically using finite elements, obtained the highest effective stress intensity factor at 45° that also gave the maximum energy release rate. Their examinations on the fracture surfaces using Scattered Electron Microscopy (SEM) after rupture showed the roughness of the fracture surface increased with increasing loading angle.

Haghgouyan *et al.* [40] proposed a new method for measurement of fracture toughness of shape memory alloys, which is built upon the ASTM J-Integral testing standard. They conducted fracture tests at shape memory, superelastic and stable austenitic phase regimes using NiTi compact tension specimens. In their J-Integral measurements, they use the combined effects of elastic and inelastic part of the load-displacement curves, and report the critical J values as a fracture toughness parameter.

They reported that fracture toughness of the superelastic and shape memory materials do not have a considerable difference, while the austenitic material has a significantly higher fracture toughness than the transformed and reoriented martensite.

Young *et al.* [41] experimentally investigated the temperature effects on the fracture toughness of a high-temperature NiTiHf SMA. They conducted fracture experiments under five different temperatures that correspond to the martensitic, transforming austenitic and non-transforming austenitic temperature ranges following the ASTM E1820 standard procedure. They reported that the martensitic transformation results in fracture toughening due to the dissipated energy. They calculated the highest stress intensity factors and J-integrals for the temperatures when the material can undergo stress induced martensitic transformation.

In a previous work by Mutlu *et al.* [42], fracture toughness tests were conducted on superelastic NiTi compact tension specimens under different loading rates in the quasi-static range. Digital image correlation and infrared thermography results showed that the martensitic transformation area decreases, and the temperature increases around the crack tip. On the other hand, the stress intensity factors showed an increasing-decreasing trend with increasing loading rate. The tests on dog-bone tension specimens showed Lüders like localized strain band formations, which increased in number with increasing loading rate. However, a similar localized band formation was not present in the fracture specimens, which is believed to be a result of the polycrstalline material. Fracture follows an almost straight path between the grain boundaries, with the influence of the small grain sizes the material behaves isotropically.

In another study by Haghgouyan *et al.* [43], fatigue crack growth of shape memory alloys is reported. They conducted cyclic loading tests using NiTiHf compact tension specimens, under both mechanical and thermal loading. They presented the corresponding cyclic J-Integral values with respect to crack growth rates, and successfully obtained the initiation thresholds, and stable crack growth behaviors of each loading case.

In a study by Makkar *et al.* [44], results of fracture experiments conducted on NiTi compact tension specimens to determine their fracture resistance behavior under thermo-mechanical coupling were reported. The specimens were subjected to isothermal mechanical and isobaric thermal loading, and they calculated contour-independent J-integral values. According to their findings, the fracture toughness of the NiTi SMA increases with increasing crack length when subjected to either isothermal mechanical or isobaric thermal loading. However, they observed that the increase in fracture toughness is lower under isobaric thermal loading compared to isothermal mechanical loading.

In their experimental and numerical work, Jape *et al.* [45] investigated the crack growth of shape memory alloy CT specimens with thermal loading under a constant load. They observed that crack propagation occurs during cooling period after the specimen temperature reaches a specific value. Their numerical simulations showed good agreement with the experimental results. They found that the residual martensite behind the growing crack tip gives rise to a shielding effect which results in stable crack propagation, while the martensitic transformation in front of the crack tip enhances the fracture toughness.

Researchers Seyedzavvar *et al.* [46] conducted fracture tests on butterfly-shaped NiTi SMA specimens using mixed mode loading at different temperatures and angles of 0, 45, and 90°. Their findings revealed that fracture toughness was notably lower at low temperatures below the martensite finish temperature, compared to temperatures higher than the austenite finish temperature, for loadings at 0 and 45°. Additionally, their numerical calculations using the finite element method showed that the energy release rate increased from mode-I loading to mixed mode loading, but decreased under mode-II loading with increasing temperature.

Usha *et al.* [47] worked on the fracture toughness determination of copper-based (Cu-based) SMAs with the addition of silver (Ag) element to the alloy. They conducted fracture tests on single edge cracked three-point bending specimens following ASTM standards. Their results showed that the fracture toughness of the Cu-Al-Mn-

Ag shape memory alloy increases as a result of Ag-addition. They observed that the Ag particles fill in the micro-voids that naturally form inside the Cu-Al-Mn matrix, reducing the micro-cracking behavior. Additionally, they found that an increase in the Ag-concentration in the alloy led to a decrease in the grain sizes, which also increased fracture toughness.

1.3.2. Numerical Studies

In their study, Stam and van der Giessen [48] examined the impact of partial or complete reversibility of stress-induced phase transformation on the size and shape of the transformation zone around the crack tip and toughness during crack growth in zirconium ceramics and SMAs. They conducted finite element analyses and utilized the constitutive equations suggested by Sun and Hwang [49]. Their findings indicated that irreversible phase transformations lead to an increase in the material's toughness.

Birman [50] studied the fracture behavior of an SMA plate subjected to Mode-I loading. The aim was to determine the size of the stress-induced phase transformation region in front of the crack and its impact on the stress intensity factor using the constitutive model proposed by Tanaka and Sato [51]. Based on the findings, Birman concluded that the phase transformation effect is not significant and that the stress intensity factor can be calculated using the material properties of austenite.

Yi and Gao [52] conducted a study on the impact of the phase transformation of SMAs on fracture toughness under Mode I loading. They used Eshelby's [53] inclusion and weight function method, along with Sun and Hwang's [54] constitutive model. The transformation region's shape and size were analyzed for stationary and steadily advancing cracks. The researchers concluded that martensite transformation led to a decrease in stress intensity factor and an increase in toughness. They also found that an increase in temperature caused the crack tip SIF to decrease. Additionally, they showed that a larger ratio of elastic moduli between the martensite and austenite phases caused the crack tip stress intensity factor to decrease.

A study conducted by Yan *et al.* [55] explored the impact of volume contracting transformation on the toughness of superelastic SMAs. Using the finite element method, they analyzed transformation-induced SIF for a quasi-static advancing crack and calculated the crack tip SIF using the equations proposed by Mc Meeking and Evans [56] and Hutchinson [57]. Their findings showed that even a small transformation volume contraction strain could lead to an increase in effective stress intensity near an advancing crack, resulting in reduced SMA toughness. While volume-expanding transformation may increase the toughness, reverse transformation has a negligible effect on transformation-induced SIF as it only partially occurs in the wake of an advancing crack tip. However, it may significantly reduce toughness in the wake of the crack tip.

In his study, Wang [58] analyzed the impact of various notch geometries on the fracture behavior of NiTi SMA through the finite element method (FEM). He computed the stress-strain distributions and phase transformation region sizes around the crack tip and discovered that the stresses around the crack tip increase when the notch geometry is changed from blunt to sharp. Wang's research findings revealed that the transformation zone shape remains unaffected by the notch geometry, but the size of the transformation zone around the crack tip is smaller for sharp cracks. Additionally, a plastic zone develops around the tip of a sharp crack at lower loads when compared to blunt notches.

In a study conducted by Freed and Banks-Sills [59], the behavior of a slowly propagating crack in an SMA plate under plane strain conditions and Mode I loading was computationally investigated. By assuming a small-scale transformation zone and using the transformation surface equation proposed by Panoskaltsis *et al.* [60] and the asymptotic stress equations, they were able to calculate the phase transformation region. Their findings revealed that the transformation zone shapes around the crack tip were similar to the plastic zone shape in plastically deformed materials. They concluded that the critical steady-state SIF increases due to phase transformation and the difference between the elastic moduli of the initial and the deformed phases. Interestingly, their results supported the idea that reversible phase transformation can actually reduce toughening.

A method for identifying the phase transformation region near a Mode I crack tip was presented by Lexcellent and Tiebaud in their study [61]. They utilized Raniecki and Lexcellent's model [62] and crack tip stress equations, along with calculating a stress intensity factor similar to Freed and Banks-Sills' [59] approach. They compared their analytical results to Robertson *et al.* [31]'s experimental results and discovered a noteworthy discrepancy.

According to the research conducted by Falvo *et al.* [63], the size of the fully martensitic region was determined using asymptotic crack tip equations for the $\theta = 0$ scenario. Irwin's plasticity corrected formula was utilized to determine the size of the plastic zone. In addition to this, finite element analyses were conducted and the results were compared to the analytical findings. Ultimately, the study concluded that Irwin's formula yields results that are in close agreement with the finite element results.

In their study, Maletta and Young [64] utilized an analytical method proposed by Maletta and Furgiuele [65] to compute the size of the phase transformation region in an infinite NiTi plate with a Mode I center crack, under plane strain conditions. To calculate the stress intensity factor, they employed Irwin's formula and far-field stress values. Comparing their analytical results with Gollerthan *et al.*'s [66] experimental results, they concluded that Gollerthan *et al.*'s findings were in between their own calculations for plane stress and strain conditions. Additionally, they identified that the phase transformation strain and the plateau stress had an impact on the phase transformation size, with an increase in transformation strain and a decrease in plateau stress resulting in a larger phase transformation region.

Baxevanis and Lagoudas [67] conducted an analysis on the fracture behavior of a superelastic SMA infinite plate in their study . The study involved subjecting a center-cracked plate to Mode I loading under plane stress condition. To calculate the J-integral, crack mouth opening displacement (CMOD), and phase transformation size based on the far-field stresses, they utilized the Dugdale [68] assumption and presented an expression. Their findings revealed that when the stress level surpasses the yield stress, the transformation strain increases, causing an increase in the size of the phase

transformation region. Furthermore, they concluded that the plastic zone size decreases due to the phase transformation at the crack tip.

In their study, Ardakani *et al.* [69] utilized XFEM to examine the fracture behavior of SMAs and took into account the effects of thermo-mechanical coupling. Through various simulations, they altered the thermodynamic properties of the material, such as the transformation stress and maximum transformation strain, to observe changes in the phase transformation region for a central crack under Mode I loading. Their findings revealed that the stress field, temperature, and size of the phase transformation zone surrounding the crack tip were strongly influenced by the loading rate. Additionally, they noted that higher loading rates resulted in an increase in forward transformation stress (A→M) and SMA material hardness. The width of the austenite and martensite regions also differed significantly between high and slow loading rates. Specifically, in the case of slow loading rates, the full martensite and transformation zones were larger compared to high loading rates.

Ardakani *et al.* [70] later investigated the effects of thermomechanical coupling on the region around the crack tip numerically through finite element analyses. They performed simulations at different loading rates and initial crack angles, calculated the extent of phase transformation regions and J-Integrals. They reported that with increasing loading rates the amount of latent heat release increases, increasing the forward transformation stress, as a result the transformation zone decreases in size. The differences found in the crack tip fields with mixed mode loading are found to be a result of different shapes of transformation regions.

Haghgouyan *et al.* [71] investigated the crack growth behavior of NiTi SMAs using the virtual crack closure technique through finite element analyses. They defined the material and cracking behavior using the experimentally obtained uniaxial tension material properties and fracture toughness (energy release rate) values. Their simulation results could capture the fracture behavior better than ones obtained with the linear elastic fracture mechanics approach.

Simoes and Martínez-Pañeda [72] proposed a phase-field model to formulate the fatigue and fracture behavior of shape memory alloys. Their model accurately depicts the effects of martensitic phase transformation at the fracture energy. They performed finite elements simulations by implementing their model, and the findings showed inelastic energy dissipation with martensitic transformation that leads to fracture toughening. They reported that at low temperatures stress induced transformation have more impact on fracture toughening. The simulations that were preformed to determine the fatigue behavior of biomedical stents were successful in inducing crack initiation and growth.

Xiong *et al.* [73] investigated the effects of crystallographic orientation and temperature on the crack propagation behavior of single crystal NiTi shape memory alloys. Finite element simulations were performed at different ambient temperatures with the consideration of six martensite variants and at five different crystallographic orientations using a phase field model on models that undergo martensitic transformation and re-orientation. Effects from plastic deformation and latent heat generation with martensitic transformation were neglected. They reported the fracture toughening effects from martensitic transformation and re-orientation formations around the crack tip. Their results from simulations show that both martensitic transformation and re-orientation during crack growth reduces the stress intensity factors at the crack tip, and cause fracture toughening, which is also dependent on the crystallographic orientation direction of applied loading.

In their paper, Hasan *et al.* [74] presented a phase-field model that predicts the fracture behavior of shape memory alloys. They used the finite elements software ABAQUS with the definition of a user material subroutine. In their simulations only the elastic strain energy contribution to crack initiation and growth is taken into account, and neglected the phase transformation effects. Their model effectively replicates the results of experiments conducted on SMAs.

Crack initiation and growth of NiTi shape memory alloys in the presence of amorphous phases was studied numerically by Zhang *et al.* [75]. They performed

simulations via ABAQUS utilizing the extended finite element method. Their results showed that cracks initiate at the amorphous phase boundaries with the NiTi material matrix in the smooth specimens. But if a pre-crack is introduced inside the NiTi matrix close to the amorphous phase, crack propagation is hindered by its' presence and making it difficult to pass through the amorphous phase region.

The fracture behavior of NiTi SMAs under impact loading conditions was studied by Cui *et al.* [76] through the use of experimental and numerical methods. They conducted split Hopkinson compression bar dynamic fracture tests on edge cracked three-point bending NiTi specimens and reported the crack growth rate as a function of impact loading rate. Their observations post failure using scanning electron microscopy (SEM) and transmission electron microscopy (TEM) on the fracture surfaces showed brittle cracking. They also utilized the finite elements method via ABAQUS and simulated the crack growth on a model that considers both plastic behavior and superelasticity. Simulation results proved to be in good agreement with the experimental data.

Voyiadjis *et al.* [77] investigated the effect of titanium-rich areas on the fracture behavior of NiTi SMAs. They carried out experiments on notched NiTi bars, and performed numerical analyses utilizing the finite element method. In the FE analyses, a micro-mechanical model that is based on the Gurson-Tvergaard-Needleman model is used. In the FE model, the Ti-rich regions were placed randomly as a different material that undergoes plastic deformation inside the superelastic SMA matrix. Their results showed that crack initiation is strongly affected by the presence of Ti-rich areas. Cracks were observed to initiate close to these areas, and resulting in accelerated cracking.

In a recent study by Sgambitterra *et al.* [78], a new method is proposed to determine the fatigue crack growth behavior of NiTi SMAs using an energy approach. They utilize the strain energy around the crack tip within the fully transformed region obtained via finite element analyzes and experimental load-displacement hysteresis curves measured from the loading pins to calculate the dissipation energy. Their results are in good agreement, and show the crack growth behavior of NiTi SMAs as a function

of dissipated strain energy.

In their paper, Xie *et al.* [79] reported the effect of crystal orientation on fracture of NiTi SMAs using molecular dynamics simulations. Their results showed that the cracking behavior at the atomic scale depends on the different anisotropic properties of crystallographic orientations. Apparently, different crack orientations can have brittle or ductile fracture behavior depending on the micro-structure at the crack tip.

1.4. Motivation of the Study

Although there are a number of studies on the determination of fatigue, fracture and crack initiation/propagation behavior of shape memory alloys, literature up to date still does not cover all the factors that affect SMAs' fracture mechanisms. SMAs cracking behavior are influenced by many factors: Crystal structure (polycrystalline & single crystal), martensitic transformation, ambient temperature, superelasticity & shape memory effect, microstructural barriers, constituent elements of the alloy, latent heat, grain size, crystal orientation, loading rate, etc.

Most of the previous studies on fracture behavior of polycrystalline SMAs focus on determination of the phase transformation effects. Phase transformation expends energy, which otherwise would go into crack initiation and subsequent propagation. The amount of dissipated energy due to phase transformation affects the toughness of the shape memory alloy: Shape memory alloys with large martensitic phase regions have higher resistance to fracture. In addition as a result of phase transformation, a significant amount of heat is released. The stress-induced martensitic transformation process is exothermic, and latent heat is released, which becomes more prominent at high loading rates. At high loading rates, the heat transfer to the surroundings is affected and this has a direct effect on cracks behavior. In this work, the energies that influence the fracture behavior of polycrystalline NiTi SMAs are investigated through J-Integral calculations, including elastic strain energy, and the dissipated energies via phase transformation and latent heat. Finite elements analyses are performed, the results of which are compared to the data obtained from J-Integral tests conducted at

two different loading rates. The separate and combined effects of phase transformation and latent heat dissipation on the energy release rates are determined.

In single-crystal SMAs, the crack initiates and then grows in the direction of the austenite–martensite band boundary where strain localization occurs. The martensitic transformation band angles are strongly influenced by the orientation dependent properties of single crystal SMA, which also affect the crack initiation angles. After initiation, the crack usually grows along an angle similar to the first crack from the notch. Since the crack angle is an important parameter in determining the fracture behavior of shape memory alloys, the calculation of the crack initiation angle is of great importance. However, there is no complete study on the determination of crack initiation angle in single crystal shape memory alloys utilizing experimental, analytical and computational analyses. In the present work, following experimental observations, the crack initiation angles in edge-notched single crystal CoNiAl shape memory alloys are calculated analytically using the Maximum Tangential Stress (MTS), Strain Energy Density (SED), and the Maximum Energy Release Rate (MERR) Criterion; and determined numerically by Finite Element Method (FEM) according to MTS, SED, and MERR Criteria.

Fracture of SMAs is also affected by the inhomogeneities which are caused by non-transforming phases that form inside the SMA matrix. These non-transforming phases often form due to heat treatment or alloying processes. Depending on their material properties, sizes and positions within the SMA material, the secondary phases may enhance or deteriorate the fracture toughness of the shape memory alloys. Tougher secondary phases may inhibit crack initiation/propagation, but often cause an unpredictable crack path. Although there are some works reporting an improvement in fracture toughness of shape memory alloys in the presence of secondary phases on growing crack paths, there is no complete work on the evaluation of crack initiation and growth behavior with detailed fracture parameter and crack growth rate calculations. In this study, the mechanisms that affect fatigue crack initiation and subsequent crack growth of single crystal CoNiAl shape memory alloys are investigated for the first time, emphasizing their behavior in the presence of a non-transforming secondary phase that

act as a microstructural barrier.

The findings of this study are expected to contribute to the literature on crack initiation and growth behavior of shape memory alloys.

1.5. Outline of the Thesis

In Chapter 2, the energies that are stored or dissipated that affect crack initiation of shape memory alloys are studied experimentally and numerically through the utilization of the J-Integral. Initially, fatigue pre-cracks are formed in the specimens via cyclic loading. Straight cracks initiated from the notches in all the specimens with 0° angles with the x-coordinate, and later propagated following a straight path. Two experiments are conducted following ASTM E1820 at different quasi-static loading rates on polycrystalline NiTi compact tension specimens. Both the crack opening and load line displacements are recorded along with the loading. J-Integrals are calculated from the areas under the load-displacement curves utilizing the basic test method (the area method) accounting for the elastic and plastic parts of the curves. Next, finite elements analyses are performed using the built-in material subroutine for shape memory alloys in ABAQUS defining the material properties of superelastic NiTi SMAs loaded under two different loading rates. For each loading rate, two models are constructed with a small increase in their crack lengths. The elastic strain energy, transformation dissipation energy, and externally applied works are extracted; heat dissipation energies are calculated from the temperature results. The change of potential energies with respect to the change in the crack surface area ($\frac{\Delta \Pi}{\Delta A}$, the energy release rates) are calculated from the analysis results. The potential energies are calculated first using only the elastic strain energy, then with the addition of the phase transformation and latent heat dissipation energies. The results are compared and discussed.

As a follow up to the work done in Chapter 2, an attempt is made in Chapter 3 to analytically and numerically calculate the crack initiation angles of superelastic specimens obtained from fatigue crack growth experiments. Single crystal CoNiAl SMA with [100] crystallographic orientation is taken as an example material for the investiga-

tions. Initially, tensile tests at shape memory and superelastic regimes are conducted on heat treated dog-bone specimens, and the mechanical properties are determined. Next, fatigue crack growth tests are conducted on single edge-notched specimens. Crack initiation and growth rate is monitored, and images for Digital Image Correlation (DIC) are captured through a Charge Coupled Device (CCD) camera. All the specimens tested have shown to have a similar cracking angle. It is discussed in the introduction part of the Chapter 3, the cracking angle of the edge-notched specimens is approximately the same with the martensite band angle that formed in the tension specimen. Taking this martensite band angle as the material orientation direction, crack initiation angles are calculated analytically utilizing the Maximum Tangential Stress (MTS), Strain Energy Density (SED), and Maximum Energy Release Rate (MERR) criteria that are proposed for non-transforming anisotropic solid materials. For completion of the study, crack initiation angles are also calculated computationally using finite elements method (FEM) according to the MTS, SED, and MERR criteria. FE models are constructed using the built-in material subroutine for shape memory alloys in ABAQUS. The material properties of the anisotropic superelastic CoNiAl are defined to the models with a material orientation angle, which is the martensite band angle. Analytical and numerical calculation results are compared with the experimental data.

Chapter 4 consists of the determination of fatigue crack growth behavior of shape memory alloys that have non-transforming secondary phase formations along the crack path. The fracture parameters are calculated at each step for a growing crack by fitting the displacement data from DIC to the anisotropic crack tip displacement equations. Stress intensity factors and crack growth rates of specimens tested at superelastic and shape memory regimes are reported. Due to the interesting behavior of increasing/decreasing stress intensity factors and crack growth rates, test specimens are examined post failure with optical microscopy to determine the curious crack growth behavior.

Finally, in Chapter 5, an overall discussion on the findings of the study, and conclusions to the work are given.

2. CRACK INITIATION AND GROWTH IN NiTi SHAPE MEMORY ALLOYS

2.1. Introduction

Depending on the heat treatment, material properties and grain sizes, polycrystal SMAs have usually two dominant fracture mechanisms. Crack path either follows the grain boundaries, or the shear band–matrix interfaces [36,80,81]. The anisotropic stress state in solid media often causes crack kinking. The kinked crack initiation in isotropic materials is usually a result of applied mixed mode loading conditions, and the fracture angle can be predicted using the equations of Erdogan and Sih [82] with reasonable accuracy. However, determination of fracture angle is more complicated for anisotropic materials, and the directional behavior of material properties plays an important role, and requires the knowledge of anisotropic orientation directions.

In this part, the crack initiation and the phase transformation in a polycrystalline SMA will be studied. The fracture parameters will be obtained through experiments and computations. An energy based approach will be used to determine the fracture behavior of polycrystalline NiTi SMA. The whole process will be taken into account, and an energy balance will be written with the total work being equal to the sum of the dissipated and stored energies [83,84]. The dissipated energy consists of the energy that goes into phase transformation, the heating due to thermoplastic effects, and heating due to martensite transformation & reorientation. When the heat transferred to the surroundings, mostly through convection, is not enough to balance the dissipation, the temperature increases and affects the mechanical behavior of the SMA. Stored energy on the other hand, consists of the energy stored in dislocations related to plastic deformation, free energy caused by phase transformation & reorientation of martensite, and latent heat. If the dissipated and the stored energies are quantified properly, then the energy available for the crack initiation and the fracture may be correctly determined.

In the subsequent sections, first the energy release rate will be determined experimentally; then, the martensitic phase transformation zone around crack tip, the dissipation energy, and the energy release rate will be evaluated computationally. Since the behavior is expected to be different, experiments and computations will be conducted at different loading rates [42]. The fracture behavior is determined by the combined effects of the energy lost to transformation, the temperature increase, the dissipation, and micro level mechanisms.

2.2. Experimental Evaluation of the J-Integral

2.2.1. Specimen and Experiments

The fracture experiments are conducted with INSTRON-8801 hydraulic machine with a 10 kN load cell using NiTi compact tension (CT) specimens following the procedure outlined by ASTM E1820 [85] - Standard Test Method for Measurement of Fracture Toughness, for J-Integral calculations. The samples for the fracture tests are cut using electrical discharge machining (EDM). Figure 2.1 presents the drawing and the photo of the test specimen.

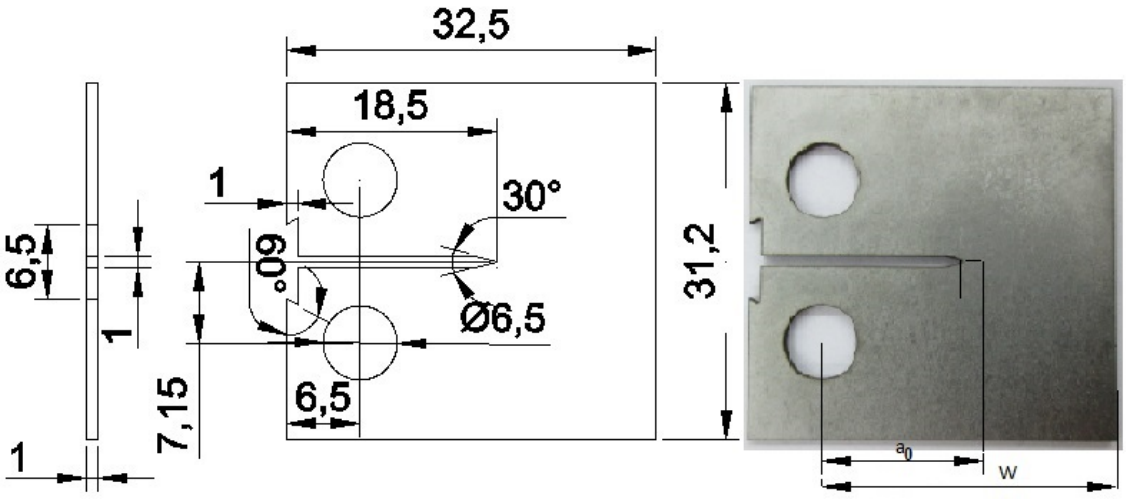

Figure 2.1. Geometry of the NiTi specimen (all dimensions are in mm). The specimen is loaded by P from the pin holes.

The specimen is loaded in tension under displacement control for which a crack opening displacement (COD) gauge is used. The load line displacemnt (LLD), and the load P are directly obtained from the testing machine Instron 8801, and the crack mouth opening displacement (CMOD) is measured using the COD gauge.

Before conducting the experiments, the CT specimen is fatigue pre-cracked under 1 Hz for 5000 cycles to a crack length a_0 (see Figure 2.1). Fatigue cycling was done under force control with a sinusoidal waveform in the load range of 0 N to 250 N. The pre-crack sizes (a_0) are measured using the Olympus 100AL optical microscope after cyclic loading tests. The maximum load (P_{max}), maximum displacement (v_{max}), and the pre-crack sizes (a_0) are tabulated in Table 2.1.

Table 2.1. Maximum Load & Displacement data from Load-Displacement curves and COD gauge, with a_0: the initial crack lengths.

Loading Rate (mm/min)	$\boldsymbol{a_0}$ **(mm)**	$\boldsymbol{P_{max}}$ **(N)**	$\boldsymbol{v_{max}}$**–LLD (mm)**	$\boldsymbol{v_{max}}$**–CMOD (mm)**
0.1	12.949	570.5	0.3875	0.4748
0.5	13.010	591.3	0.4163	0.5029

Experiments are conducted at two different loading rates: 0.1 and 0.5 mm/min, and force displacement curves are plotted. J-Integrals corresponding to the maximum loads (P_{max}) are calculated using the equations given by ASTM E1820 [85].

2.2.2. Crack Initiation in NiTi Specimens

In both the specimens cracks initiated from the notch at an angle of 0° with the x-coordinate as shown in Figure 2.2. Later, the crack followed a straight path when more load is applied during the experiments (see Figure 2.3).

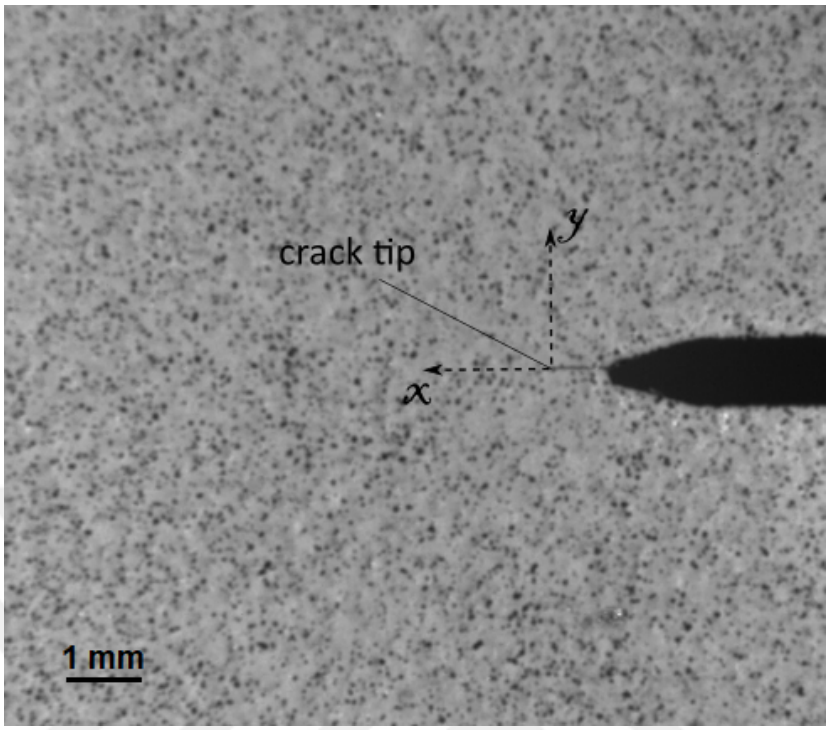

Figure 2.2. Crack initiation from the notch in polycrystalline NiTi CT specimen.

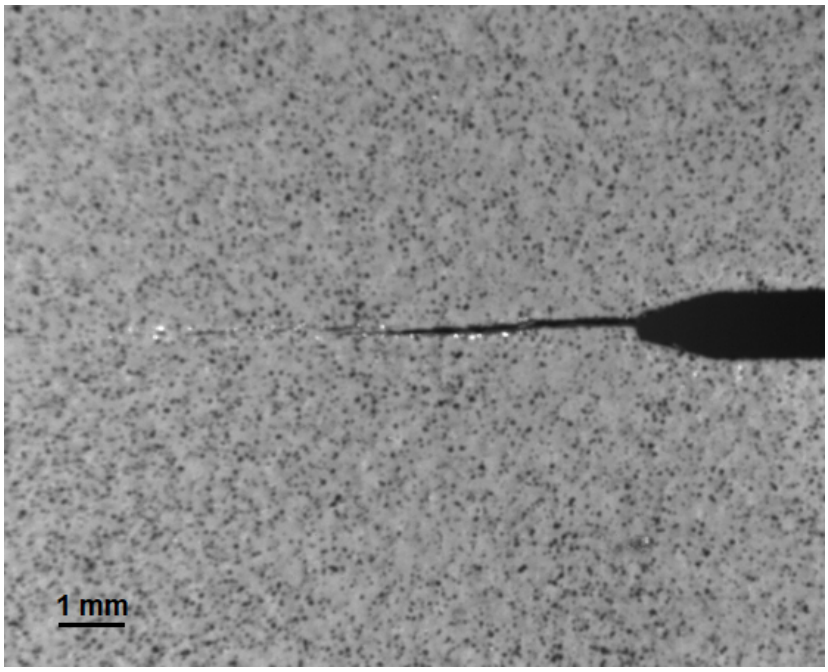

Figure 2.3. Crack growth in polycrystalline NiTi CT specimen.

2.2.3. Evaluation of the Stress Intensity Factors and J-Integrals

The stress intensity factor is evaluated from P_{max} applied to the specimen and a_0 that are given in Table 2.1, using the equation below [85]:

$$K = \frac{P}{\sqrt{BB_N}\sqrt{W}} \cdot f\left(\frac{a}{W}\right), \tag{2.1}$$

where

$$\begin{aligned} f\left(\frac{a}{W}\right) &= \frac{\left(2+\frac{a}{W}\right)}{\left(1-\frac{a}{W}\right)^{\frac{3}{2}}} \cdot \left[0.886 + 4.64\left(\frac{a}{W}\right) - 13.32\left(\frac{a}{W}\right)^2\right. \\ &+ \left. 14.72\left(\frac{a}{W}\right)^3 - 5.6\left(\frac{a}{W}\right)^4\right]. \end{aligned} \tag{2.2}$$

Here, a is the crack length, W is the specimen width measured from the center-line of the holes to the specimen edge as seen in Figure 2.1, and B is the specimen thickness. For the specimen used in our experiments $B_N = B = 1$.

The J-Integral is calculated as follows:

$$J = J_{el} + J_{dis}, \tag{2.3}$$

here; J_{el} is the elastic component of J, and J_{dis} is the part that corresponds to dissipation.

J-Integral calculations are done following the Basic Test Method from the ASTM E1820 for the compact tension specimen at a point corresponding to the maximum displacement and load ($v_{max} - LLD$ & P_{max} – given in Table 2.1) on the specimen force versus load-line displacement curves shown in Figures 2.4 and 2.5.

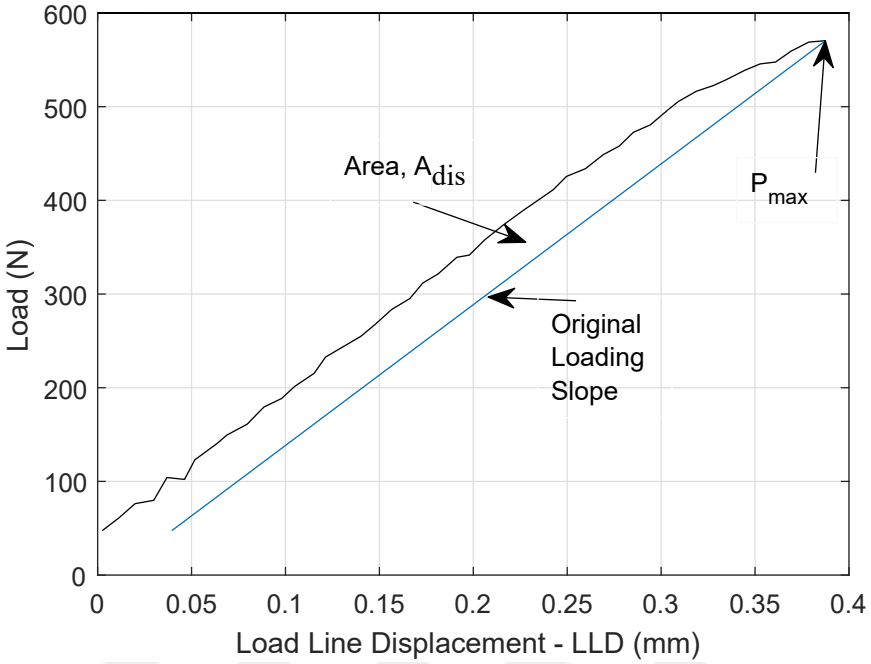

Figure 2.4. Load vs. Load Line Displacement (LLD) for 0.1 mm/min loading rate.

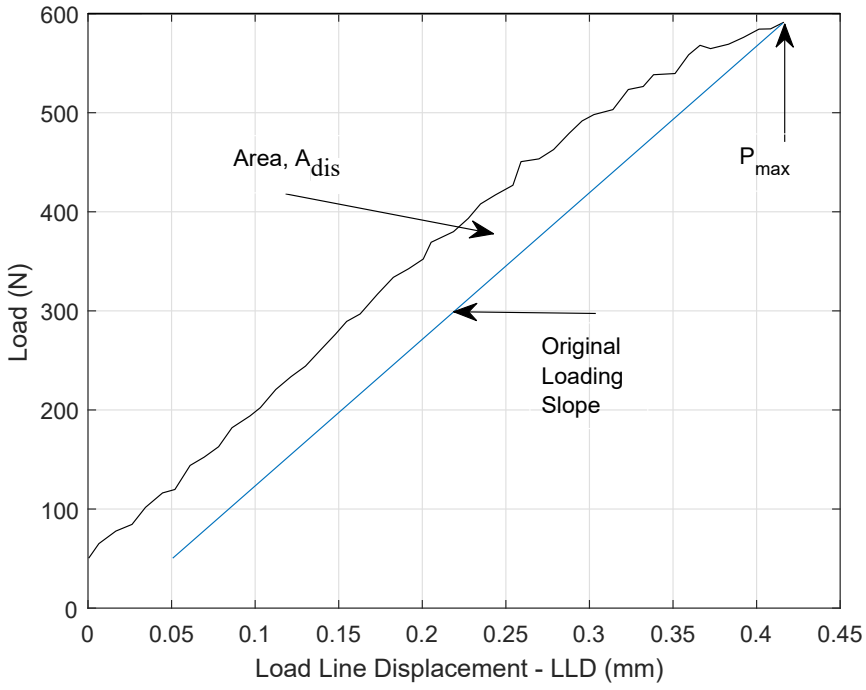

Figure 2.5. Load vs. Load Line Displacement (LLD) for 0.5 mm/min loading rate.

Elastic parts of the J-Integrals, J_{el} are calculated as follows:

$$J_{el} = \frac{K^2(1-\nu^2)}{E}, \tag{2.4}$$

where K is the stress intensity factor calculated from Equation (2.1), with $a = a_0$, given in Table 2.1; and J_{dis} as,

$$J_{dis} = \frac{\eta_{dis} A_{dis}}{B_N b_0}, \tag{2.5}$$

A_{dis} are the areas shown in Figures 2.4 and 2.5; B_N is the specimen thickness. For the specimen used in the present experiments,

$$B_N = B = 1; \tag{2.6}$$

$$b_0 = W - a_0, \tag{2.7}$$

which is the uncracked ligament, and

$$\eta_{dis} = 2 + \frac{0.522 b_0}{W}. \tag{2.8}$$

Resulting A_{dis}, J_{el}, J_{dis}, J, and K are tabulated in Table 2.2.

Table 2.2. J-Integrals and stress intensity factors calculated using the load line displacement.

Loading Rate **(mm/min)**	$\boldsymbol{A_{dis}}$ $\boldsymbol{(N \cdot mm)}$	$\boldsymbol{J_{el}}$ $\boldsymbol{(kJ/m^2)}$	$\boldsymbol{J_{dis}}$ $\boldsymbol{(kJ/m^2)}$	$\boldsymbol{J}$ $\boldsymbol{(kJ/m^2)}$	$\boldsymbol{K}$ $\boldsymbol{(MPa\sqrt{m})}$
0.1	20.5	16.6	3.56	20.1	34.0
0.5	29.8	18.1	5.19	23.3	35.5

The J-Integrals are also calculated using the maximum crack mouth opening displacement obtained from the COD gauge, and the corresponding results are tabulated in Table 2.3. Force versus the CMOD curves are plotted in Figures 2.6 and 2.7.

Table 2.3. J-Integrals and stress intensity factors calculated using the crack mouth opening displacement obtained from the COD gauge.

Loading Rate (mm/min)	A_{dis} $(N \cdot mm)$	J_{el} (kJ/m^2)	J_{dis} (kJ/m^2)	J (kJ/m^2)	K $(MPa\sqrt{m})$
0.1	34.5	16.6	5.98	22.6	34.0
0.5	47.9	18.1	8.34	26.4	35.5

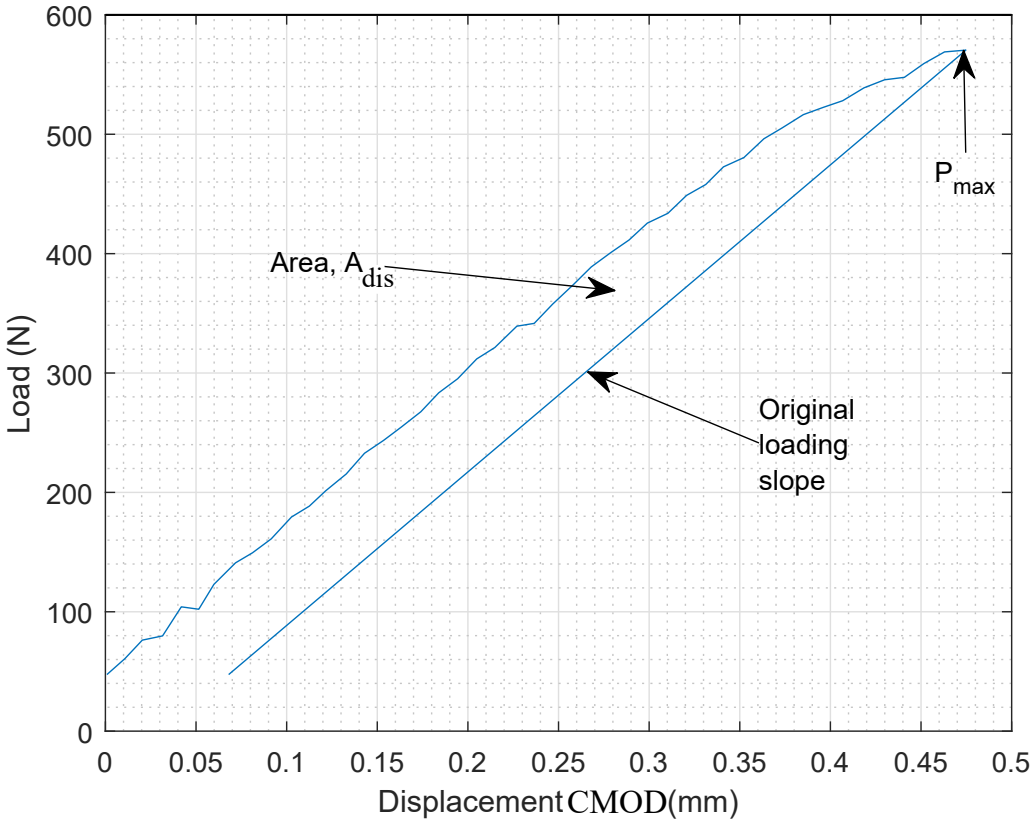

Figure 2.6. Load vs. Crack Mouth Opening Displacement (CMOD) for 0.1 mm/min loading rate.

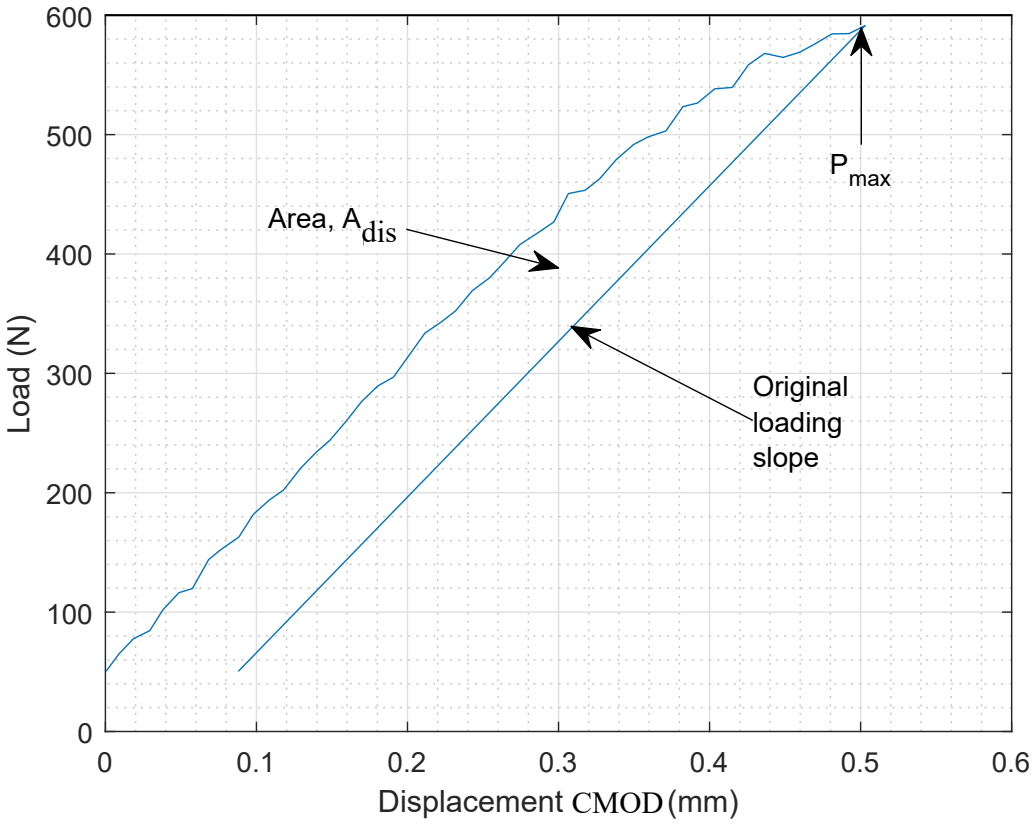

Figure 2.7. Load vs. Crack Mouth Opening Displacement (CMOD) for 0.5 mm/min loading rate.

J-Integrals presented in Tables 2.2 and 2.3 are the values that correspond to the maximum loads the specimens can withstand. From the experiments, only one J vs. Δa point is obtained. Results of the experiments showed that using a COD gauge for displacement control does not give good results for higher loading rates due to the inertia of the clips attached to the specimen. As a result, only the quasi-static loading rate test results are presented in this part of the study.

J-Integral calculations are done using both the load line displacement and the crack mouth opening displacement results. However, results from load line displacement data still should be interpreted with caution since the displacement control was done with the crack opening displacement gauge.

Results of the experiments suggest that optical measurement systems such as DIC are better suited for experiments that are sensitive to loading rates. With DIC, one can create a virtual extensiometer, and obtain more accurate and reliable results. Local strain rate determination has high importance in fracture testing, since the strain rate at the fracture process zone is always higher than the applied rate as a result of the crack tip singularity.

2.3. Evaluation of the J-Integral Using Finite Elements

In Section 2.2, the results of J-Integral experiments are presented.But, the obtained displacement data from COD gauges do not have high accuracy due to the inertia of the gauge clips. In this section, an attempt is made to determine energy release rates and J-Integrals using finite elements. By modeling the exact specimen dimensions and the conditions of the aforementioned experiments with ABAQUS, crack growth of NiTi CT specimens will be determined via J-integral and energy release rate. In the following, first the finite elements model used in ABAQUS is introduced. The material properties and the loading conditions that are applied to the problem geometry are discussed.

2.3.1. Finite Elements Model (ABAQUS)

Finite element models of the specimens are built using eight-node thermally coupled brick, trilinear displacement and temperature (C3D8T) elements. Only half of the plate is modeled using symmetry, a finer mesh is applied around the crack tip with an approximate element size of 0.025 mm. The plates are loaded with a concentrated load at the pin holes of the CT specimens up to the maximum load applied in the experiments. The mesh, loading, and the boundary conditions used in ABAQUS are shown in Figure 2.8.

The problem geometry and the corresponding dimensions are the same for all the models, a photo and the sketch of the samples may be seen in Figure 2.1. Only the crack lengths are changed to obtain the exact geometries of the specimens used

in J-Integral experiments (see Table 2.1). NiTi material properties are defined using the built-in material subroutine for SMAs [86] with the material properties obtained from tension experiments of the isotropic superelastic NiTi [42]. The SMA material properties are tabulated in Tables 2.4 and 2.5.

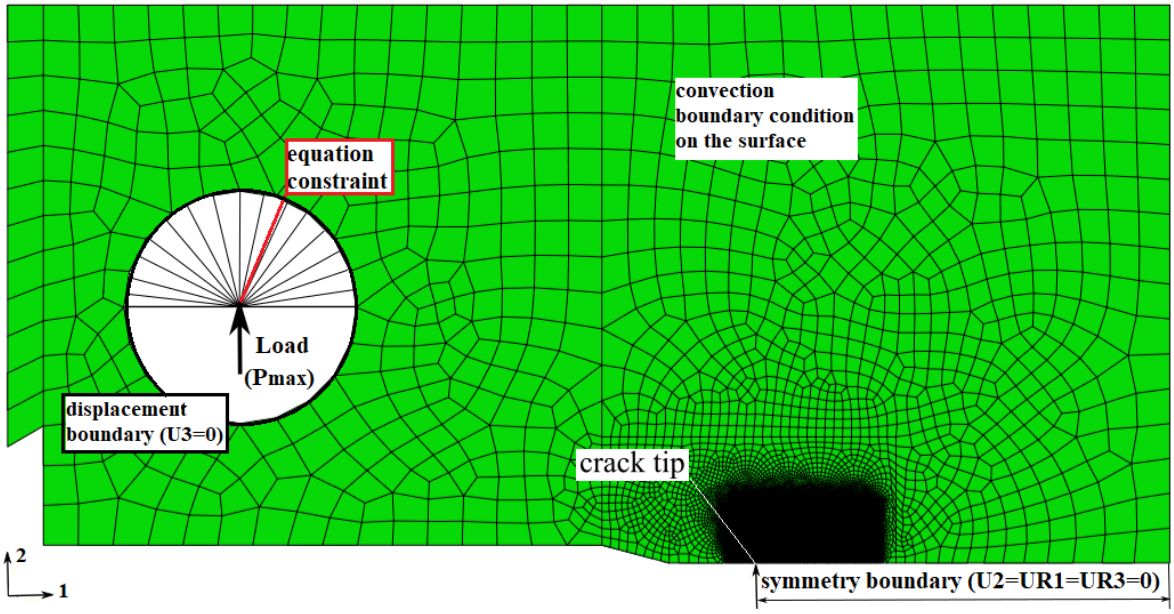

Figure 2.8. Mesh, boundary conditions, and loading of the CT specimen finite element model.

Table 2.4. NiTi finite element model material properties for the 0.1 mm/min loading rate experiment [42].

E_A (MPa)	ν_A	E_M (MPa)	ν_M	ϵ^L	σ^S_{tL} (MPa)	σ^E_{tL} (MPa)	σ^S_{tU} (MPa)
61600	0.33	45800	0.33	0.0635	470	495	220
σ^E_{tU} (MPa)	σ^S_{cL} (MPa)	T_0 (K)	$(\frac{\delta\sigma}{\delta T})_L$ (MPa/K)	$(\frac{\delta\sigma}{\delta T})_U$ (MPa/K)	σ^P_1 (MPa)	ϵ_1	
216	600	299.15	6.95	7.3	1000	0.085	
c_p $(J/kg \cdot K)$	k $(W/m \cdot K)$	h_{air} $(W/m^2 \cdot K)$					
440	18	50					

Table 2.5. NiTi finite element model material properties for the 0.5 mm/min loading rate experiment [42].

E_A (MPa)	ν_A	E_M (MPa)	ν_M	ϵ^L	σ^S_{tL} (MPa)	σ^E_{tL} (MPa)	σ^S_{tU} (MPa)
61700	0.33	45700	0.33	0.0663	501	549	184
σ^E_{tU} (MPa)	σ^S_{cL} (MPa)	T_0 (K)	$(\frac{\delta\sigma}{\delta T})_L$ (MPa/K)	$(\frac{\delta\sigma}{\delta T})_U$ (MPa/K)	σ^P_1 (MPa)	ϵ_1	
139	600	299.15	6.95	7.3	1000	0.09	
c_p $(J/kg \cdot K)$	k $(W/m \cdot K)$	h_{air} $(W/m^2 \cdot K)$					
440	18	50					

Next, simulations are conducted for the two models with two different crack lengths: the initial pre-crack, and the crack length the experiment software measured to calculate the J-Integral value following the ASTM E1820 test method [85]. The Strain Energy (ALLSE), Plastic Dissipation Energy (ALLPD) which corresponds to the transformation energy for the superelastic materials in ABAQUS, External Work (ALLWK), and far-field J-Integral values are extracted from the "History Output" results of ABAQUS.

2.3.2. Evaluation of the Energy Release Rate

The energy release rate is defined as the change of potential energy with respect to the change in the crack surface area, that is equal to the rate of energy required to create new crack surfaces [87] and shown as follows:

$$\mathcal{G} = -\frac{\Delta \Pi}{\Delta A} = \frac{\Delta W_s}{\Delta A}, \tag{2.9}$$

where W_s is the fracture work needed for forming new crack surfaces; ΔA is the increase in crack surface area and is calculated by multiplying the increase in crack length by

the plate thickness,

$$\Delta A = \Delta a \cdot t; \tag{2.10}$$

and Π is the potential energy: the energy available for an increment of crack growth, which is defined for linear elastic bodies as:

$$\Pi = U_{SE} - W_{ext}. \tag{2.11}$$

Here, U_{SE} is the elastic strain energy stored in the system, and W_{ext} is the work of external forces applied. For a linear elastic body the potential energy equals to the elastic strain energy that is stored in the system;

$$\Pi = -U_{SE}; \tag{2.12}$$

and the energy release rate can be calculated as follows:

$$\mathcal{G} = -\frac{\Delta \Pi}{\Delta A} = \frac{\Delta U_{SE}}{\Delta A}. \tag{2.13}$$

2.3.2.1. Stored Energy in Shape Memory Alloys. For superelastic shape memory alloys with negligible plastic deformation, the stored energies consists of the elastic strain energy (U_{SE}) and the reversible part of the transformation energy (U_{tr}). For a crack under cyclic loading some of the transformation energy can be recovered via reverse transformation. However for a over-loaded crack (that is loaded until fracture-no unloading case), the energy that goes to martensitic transformation cannot be recovered, so all of the transformation energy contributes only to the dissipated energy from the body.

2.3.2.2. Dissipated Energies in Shape Memory Alloys. Latent heat and hysteretic dissipation are the most significant contributors to dissipated energy in a superelastic

body. In this study, the hysteretic dissipation (energy dissipation via martensitic transformation around the crack tip) is taken directly from ABAQUS that is the output parameter ALLPD; and the heat dissipation energy (U_Q) from the system is calculated as the energy required to increase the temperature of the body by an increment of "ΔT": temperature increase in the body released as a result of martensitic transformation, the mean surface temperature increase of the plate obtained from ABAQUS .

2.3.2.3. $\mathcal{J}$-Integral Calculations. The differences in the energies, ($\frac{\Delta U}{\Delta A}$), are obtained from different finite element models by increasing the crack length by an increment of "Δa" (see Table 2.7) from the initial crack lengths (a_0 in Table 2.1). The values obtained using this method are also defined as the energy release rates. However, they do not relate to the "energy released from the body when the crack grows", but "differences in the energies absorbed by the body near the cracks with a crack growth length of Δa". Energy release rate from here on is shown with "$\mathcal{J}$" which is defined for non-linear elastic materials, instead of $\mathcal{G}$ that corresponds to the linear elastic materials [87]. "$\mathcal{J}$" here also differs from the "J" that was used to define the experimentally measured J-Integrals in the previous Section 2.2.

In the following, the potential energy is calculated accounting for the elastic strain energy, transformation energy, and heat dissipation energy as follows:

$$\Pi = U_{SE} + U_{tr} + U_Q - W_{ext}. \tag{2.14}$$

Dividing by ΔA, the differences in the crack surface areas, the energy release rate ($\mathcal{J}$) becomes:

$$\mathcal{J} = \frac{\Delta W_s}{\Delta a \cdot t} = -\frac{\Delta \Pi}{\Delta a \cdot t} = \frac{\Delta U_{SE}}{\Delta A} + \frac{\Delta U_{tr}}{\Delta A} + \frac{\Delta U_Q}{\Delta A} - \frac{\Delta W_{ext}}{\Delta A}. \tag{2.15}$$

Energy release rates are calculated assuming different stored and dissipated energies to see the differences in energies that contribute to crack growth. In the first case, only the elastic strain energy is taken into account. Then, calculations are repeated

with the addition of transformation, and later heat dissipation energies to the potential energy function (Equation (2.14)). Results are tabulated in Table 2.6.

Table 2.6. Energy release rates calculated from FE results accounting for the stored and dissipated energies that affect crack growth.

Loading Rate (mm/min)	$\frac{\Delta U(SE-W_{ext})}{\Delta A}$ (kJ/m^2)	$\frac{\Delta U(SE+tr-W_{ext})}{\Delta A}$ (kJ/m^2)	$\frac{\Delta U(SE+tr+Q-W_{ext})}{\Delta A}$ (kJ/m^2)
0.1	28.96	1.81	32.41
0.5	29.49	1.71	48.1

The results of only the elastic strain energy assumption, $(\frac{\Delta U(SE-W_{ext})}{\Delta A})$, show that the magnitude of energy release rate increases with increasing loading rate, which is simply the result of the higher martensitic transformation start stress of the 0.5 mm/min loading rate case (see Tables 2.4 and 2.5). This is due to ABAQUS's assumption that takes the martensite transformation start stress as the yield point, after which plasticity occurs and the energy is dissipated via plastic deformation. As a result, a higher elastic strain energy is stored in the plate that was modeled with the material properties of the higher loading rate case.

Next, calculations are repeated accounting for the transformation energy along with the elastic strain energy. Results from calculations for this case (given in the column $\frac{\Delta U(SE+tr-W_{ext})}{\Delta A}$ of the Table 2.6) show a decreasing trend with increasing loading rate. This decrease is due to the different sizes of transformation areas, that result in different amounts of energy dissipation. The martensitic transformation regions around the crack tips for the two models are presented in Figures 2.9 and 2.10. The energy release rate of the lower loading rate material model is higher due to the larger transformation region, hence the higher energy dissipation via martensitic transformation.

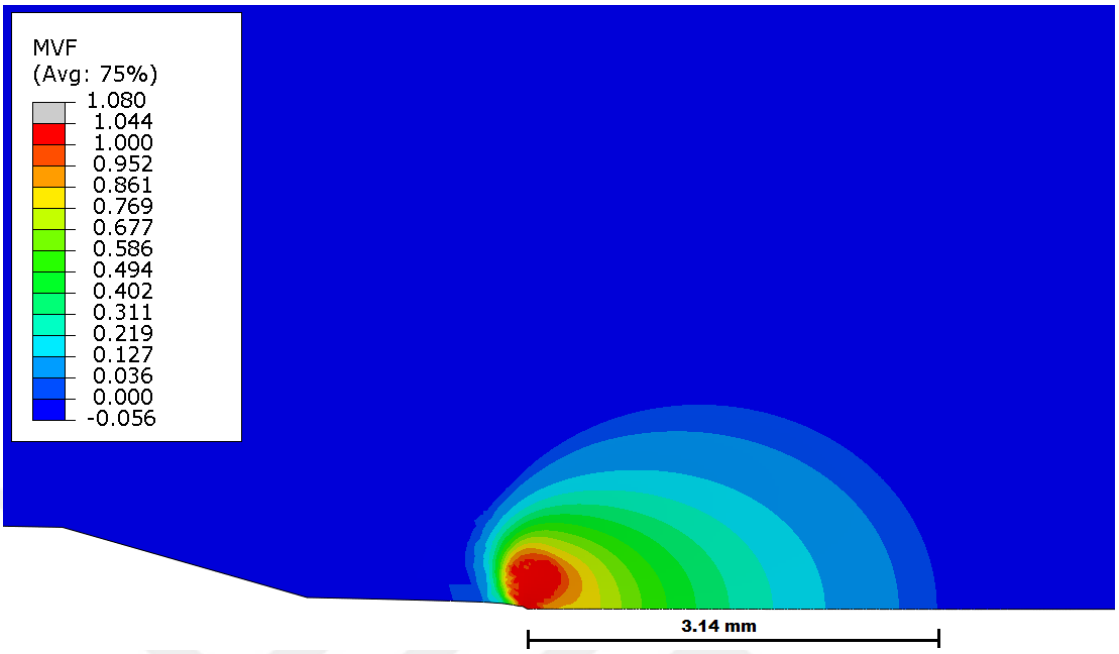

Figure 2.9. Martensitic transformation region around the crack tip of the 0.1 mm/min loading rate material model.

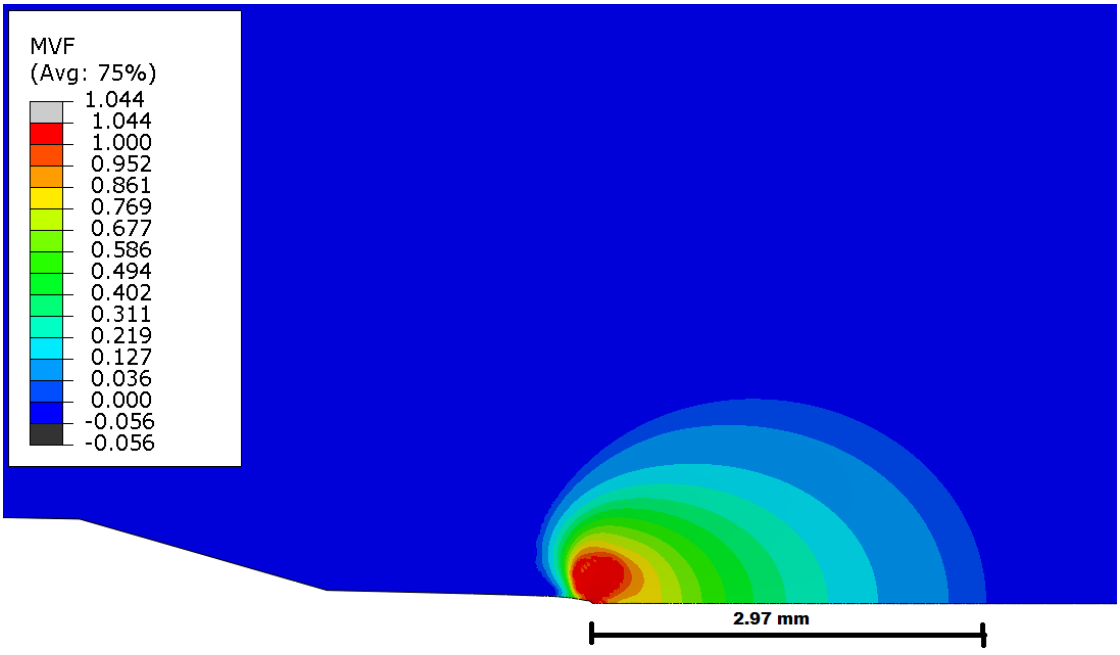

Figure 2.10. Martensitic transformation region around the crack tip of the 0.5 mm/min loading rate material model.

It should be noted here that the magnitudes of energy release rates that are calculated accounting for the dissipated energy with martensitic transformation are lower than the ones calculated only assuming the elastic strain energy. The reason for this is that, the energy release rate calculated from the elastic strain energy relates to the "energy released from the body with crack growth", hence the negative value. But the former corresponds to the "absorbed energy by the body near the crack tip", which means that a large part of the energy of the system is lost due to martensitic transformation which results in a lower amount of energy available for crack growth. As a result, more force needs to be applied for further crack growth to occur.

In the last column of the Table 2.6, the energy release rates calculated with by incorporating both the energies dissipated by transformation and heat into the elastic strain energy for potential energy determination ($\frac{\boldsymbol{\Delta U(SE+tr+Q-W_{ext})}}{\boldsymbol{\Delta A}}$) are tabulated. Results of this case show that the energy release rate of the higher loading rate material model is higher than the lower loading rate material model.

In Figures 2.11 and 2.12 temperature fields around the crack tips of the two plates at the time of maximum loading P_{max} for each case are plotted.



Figure 2.11. Temperature field around the crack tip, 0.1 mm/min loading rate (K).

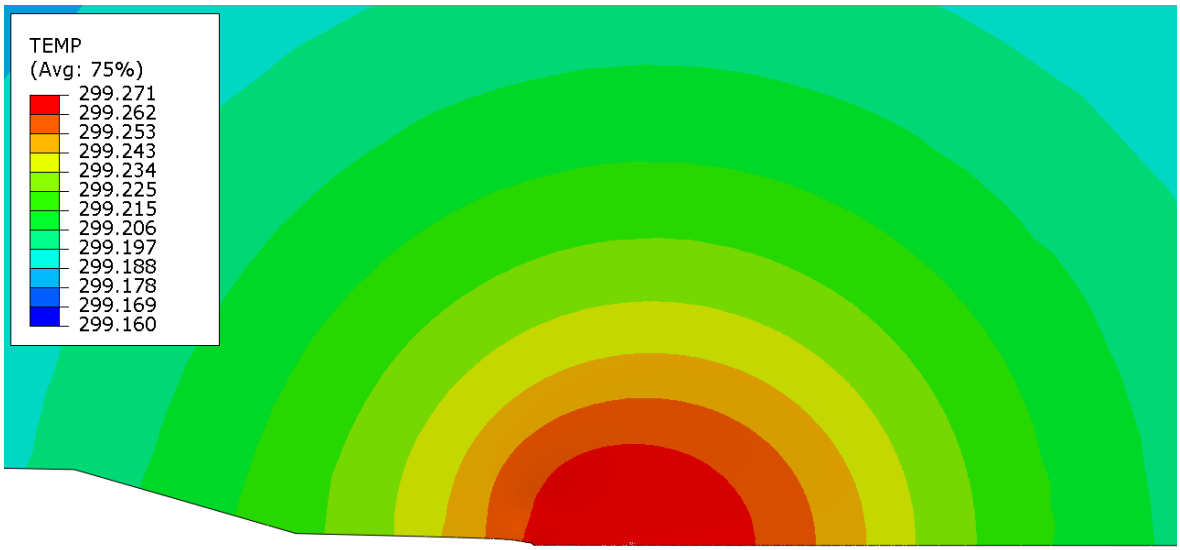

Figure 2.12. Temperature field around the crack tip, 0.5 mm/min loading rate (K).

It is seen that the temperature increase around the crack tip of the 0.5 mm/min loading rate material model is higher, which results in a higher heat dissipation energy from the plate. As a result, the energy release rate increases, and the amount of energy available for crack growth decreases.

Here, it can be observed that the heated region around the crack tip of the 0.1 mm/min loading rate case is larger due to the longer time available for conduction heat transfer inside the plate [42]. Heat loss to the surroundings via convection were found to be negligible due to the low magnitudes of temperature increase in the both plates, which are around 0.1 K.

2.3.3. J-Integral From ABAQUS, $\mathcal{J}$

ABAQUS calculates the $\mathcal{J}$-Integral along a contour "Γ" around the crack as:

$$\mathcal{J} = \int_{\Gamma} \left(w \, \mathrm{d}y - T_i \frac{\delta u_i}{\delta x} \, \mathrm{d}s \right); \tag{2.16}$$

which is equal to the energy release rate for linear or non-linear materials under quasi-static loading [87].

In Equation (2.16), w is the elastic strain energy density plus the plastic dissipation for non-linear materials [88], and is defined as follows:

$$w = \int_0^{\epsilon_{ij}} \sigma_{ij} \, \mathrm{d}\epsilon_{ij}, \tag{2.17}$$

where ϵ_{ij} and σ_{ij} are the strain and stress tensors, respectively; and

$$T_i = \sigma_{ij} n_j, \tag{2.18}$$

which is the traction vector acting on the contour boundary, with n_j, the normal of the contour boundary. Additionally, u_i is the displacement vector; x & y are the crack configuration coordinates; $\mathrm{d}s$ is a length increment along the contour.

For shape memory alloys, $\mathcal{J}$-Integral is contour dependent due to the phase transformation region around the crack tip, which becomes contour independent (converges to a constant value) outside of the transformation region where the material is homogeneous and in fully austenitic phase. Although phase transformation around the crack tip has a significant effect on the energy release rate of shape memory alloys, the phase transformation region coincides with the crack tip singularity field. To circumvent the effects of crack tip singularities, the far-field $\mathcal{J}$-Integrals will be reported here.

The values of far-field $\mathcal{J}$-Integrals ($\mathcal{J}^A_{FE}$) that are taken from the outside of the transformation region where the phase is fully austenitic are tabulated in Table 2.7 for the final crack lengths with growths of "Δa" in addition to the initial crack lengths a_0 presented in Table 2.1. "Δa" is the difference between the final crack length that is given by the J-Integral testing software, and the initial crack length.

Table 2.7. The far field (austenitic region) $\mathcal{J}$-Integrals obtained from ABAQUS.

Loading Rate (mm/min)	$\boldsymbol{\Delta a}$ **(mm)**	**CTOD (mm)**	**CMOD (mm)**	$\boldsymbol{\mathcal{J}^{A}_{FE}}$ $\boldsymbol{(kJ/m^2)}$
0.1	0.735	0.035	0.576	52.1
0.5	0.998	0.035	0.588	55.04

The results tabulated in Table 2.7 show an increase in the energy release rate with increasing loading rate. It should be noted that, the presented $\mathcal{J}$-Integral values belong to the far-field contours where no martensitic transformation is present. So the increase in the energy release rates depend more on the higher P_{max} value, longer crack length, and higher transformation stresses. Still, since these parameters are directly dependent on the loading rate, and taken from the corresponding experimental results, the increase in energy release rate can be attributed to the increasing loading rate.

The crack mouth opening displacement measured under 0.5 mm/min loading rate is larger than the test conducted at 0.1 mm/min loading rate due to the larger crack length, and also due to the maximum load (P_{max}) the specimen can undergo (see Table 2.1). It should be noted that the CMOD values of the finite element models are higher than the experiment results measured with the COD gauge. This is thought to be the result of the low measuring capacity of the COD gauge due to the inertia of the knife-edge clips.

2.4. Summary and Conclusions

In this chapter, the J-Integrals are evaluated experimentally and calculated computationally for the SMA. Experiments are based on the ASTM E1820 [85], which is used for fracture toughness determination of non-transforming materials. Two experiments are conducted on compact tension specimens at different quasi-static loading rates of 0.1 and 0.5 mm/min. Both load-line and crack mouth opening displacements

are recorded along with the loading. Load-displacement curves are plotted which are then used for the calculation of the J-Integrals following Equations (2.4) and (2.5) that include both the elastic and plastic parts of the curves plotted in Figures 2.4, 2.5, 2.6 & 2.7. The J-Integrals are calculated using crack mouth opening and load-line displacements, and the values are given in Table 2.8 along with the testing software results.

Table 2.8. J-Integrals calculated from Load-Displacement curves in Figures 2.4, 2.5, 2.6 & 2.7, and the J-Integral test software results (J_{E1820}).

Loading Rate (mm/min)	$\boldsymbol{J_{CMOD}}$ $\boldsymbol{(kJ/m^2)}$	$\boldsymbol{J_{LLD}}$ $\boldsymbol{(kJ/m^2)}$	$\boldsymbol{J_{E1820}}$ $\boldsymbol{(kJ/m^2)}$
0.1	22.6	20.1	29.02
0.5	26.4	23.3	28.29

The software uses the linear compliance method from ASTM E1820 standard [85] to calculate the J-Integral, and estimates the J slightly higher than $\boldsymbol{J_{CMOD}}$ & $\boldsymbol{J_{LLD}}$ that are calculated using the area method. However, it can be seen that the area method is better in predicting the effect of loading rate.

After the experiments, the energies are computed using ABAQUS, the far-field $\mathcal{J}$-Integral values are extracted, and the results are tabulated in Table 2.9.

Table 2.9. Energy release rates, ($\frac{\Delta U}{\Delta A}$), calculated from finite elements, and the far field $\mathcal{J}$-Integral from ABAQUS.

Loading Rate (mm/min)	$\boldsymbol{\frac{\Delta U(W_{ext}-SE)}{\Delta A}}$ $\boldsymbol{(kJ/m^2)}$	$\boldsymbol{\frac{\Delta U(SE+tr-W_{ext})}{\Delta A}}$ $\boldsymbol{(kJ/m^2)}$	$\boldsymbol{\frac{\Delta U(SE+tr+Q-W_{ext})}{\Delta A}}$ $\boldsymbol{(kJ/m^2)}$	$\boldsymbol{\mathcal{J}_{FE}}$ $\boldsymbol{(kJ/m^2)}$
0.1	28.96	1.81	32.41	52.1
0.5	29.49	1.71	48.1	55.04

The far-field $\mathcal{J}$-Integral reported by ABAQUS and the energy release rates calculated accounting for both the phase transformation ("ALLPD" in ABAQUS) and heat dissipation (Q) energies are found to be approximately of the same order, and an increasing trend with increasing loading rate is obtained. The reason for the differences is thought to come from the different methods used for the calculations.

Although both correspond to the energy release rates, ABAQUS calculates the $\mathcal{J}$-Integral from the energies released from the body in a contour. In the other method however, the differences in energies absorbed by the whole body with an increase in the crack length of an amount of Δa are calculated. Additionally, the $\mathcal{J}$-Integral values from ABAQUS belong to the austenitic phase where no transformation occurs, but $\frac{\Delta U(SE+tr+Q-W_{ext})}{\Delta A}$ results account for the transformation and heat dissipation energies. Therefore, the increase in the energy release rate with increasing loading rate is more significant in the latter case.

It is also worth noting that, the energy release rate calculated that accounts for both the phase transformation (tr) and heat dissipation (Q) energies of the 0.5 mm/min loading rate case is approximately the same with the far-field $\mathcal{J}$-Integral ABAQUS reports. It is discussed in the literature that the austenitic phase of the shape memory alloys has higher fracture toughness than the martensitic phase [40]. The results of far-field $\mathcal{J}$-Integrals that were taken from contours outside the transformation region, are higher than the energy release rates calculated accounting for martensitic transformation. The energy release rate in the case of the higher loading rate case comes closer to the $\mathcal{J}$-Integral value of the austenitic phase as a result of higher magnitude of dissipative energies.

In previous studies conducted for fracture behavior determination of shape memory alloys, it has been reported that phase transformation and generation of latent heat under isothermal conditions are important contributors to the fracture toughness [30, 89–91]. Since some of the energy of the system is lost to phase transformation and to generation of heat, the energy required for crack propagation decreases, resulting in a delay in fracture and thus an increase in fracture toughness.

The results of this chapter support previous reports on the effects of phase transformation and heat generation on the fracture behavior of shape memory alloys. It is found that the energy release rates calculated taking the transformation (U_{tr}) and the heat dissipation (U_Q) energies into account give comparatively higher results, indicating an increase in fracture toughness. A considerable amount of energy goes to phase transformation and heat generation, latter of which is found to affect the energy release rate more than the former. Since the amount of heat dissipation is lower at low loading rates, the energy release rate of the plate loaded under a higher loading rate increases significantly due to higher heat dissipation energy.

Experimental results obtained from the specimen loaded at the lower loading rate have better correspondence to the FE results of energy release rates calculated including the effects from transformation and heat dissipation than the higher loading rate specimens results, which is the result of higher magnitude of latent heat dissipation; experiments significantly underestimate the energy release rate of the high loading rate specimen. The energy release rates calculated with only the elastic strain (SE) energies show a nearly perfect match to the experimental data calculated by the testing software (given as J_{E1820} in Table 2.8). However, for transforming materials, using only the elastic strain energy (SE) and neglecting the dissipative terms in the study of fracture behavior is not reliable, and will underestimate the resistance to fracture. The dissipated energies should not be neglected in the calculations for the determination of fracture behavior of shape memory alloys.

On the other hand, although a macroscopic approach that uses energy release rate gives an idea on fracture resistance, it misses local effects around the crack tip that affects the crack growth behavior. In the following chapters, experimental and computational work will be done to study the effect of phase transformation and microstructural formations around the crack tip.

3. CRACK INITIATION ANGLE IN SINGLE CRYSTAL SHAPE MEMORY ALLOYS

3.1. Introduction

The single crystal SMAs are free from the effect of grain boundaries. As a result, martensite localization remain the most important feature on fracture mechanism of single crystal SMAs. In single-crystal SMAs, the transformation zone grows from martensitic variants. The crack initiates from the austenite-martensite or the martensite-martensite interface of the larger transformation area and grows [91]. The growing crack angle depends on the crystallographic orientation with respect to the notch which also affects the formation of martensitic transformation band angles [92]. Under cyclic loading, the austenite-martensite interface of the active martensite variant undergoes fatigue and a crack starts due to the continuous forward/reverse transformation in the martensite band. The deformation follows martensite bands where the strain is the highest, and fracture occurs along the austenite-martensite interface where high shear stresses form resulting in eventual failure [93].

In the literature, there are some experimental studies on single crystal shape memory alloys that discuss how the direction of martensite bands can have an influence on crack initiation and growth. Tests on CuAlNi single crystal specimens with varying initial notch orientations show that the final crack direction has approximately the same angle from the initial martensite band directions [92]. The growing crack angle depends on the crystallographic orientation with respect to the notch, which also affects the formation of martensitic transformation band angles. Experiments on tensile and notched specimens, show that the first martensite variant activated in the tensile specimen has the same magnitude of angle as the fracture angle [94]. In an experimental work on NiMnGa ferromagnetic SMAs, the fracture behavior is found to strongly dependent on martensitic transformation: the fracture surface was parallel to one of the martensite variant directions [95]. Experiments conducted on single crystal

NiTi specimens showed Luders-band formations in the tension specimen at 28°, and martensitic plates at the notch confined in an area between ±23°. Further loading resulted in a crack initiation from the notch tip, that propagated at 25°, also suggesting that the crack propagates approximately along the austenite-martensite interface [96].

In their computational work on single crystal and poly-crystalline CuAlBe SMAs, Cisse and Zaeem [91] used finite elements (COMSOL) and reported that in both the single crystal and poly-crystalline edge cracked/notched plates, deformation and crack propagation is influenced by the crystallographic orientation. In the poly-crystalline models, they expect the crack initiation to be affected by the orientation of the grain in which the crack tip is located. Also, the martensitic transformation and subsequent crack propagation is disturbed by different grain orientations around the crack tip resulting in a more unpredictable crack propagation angle. Amin-Ahmadi *et al.* [81] studied crack propagation behavior of polycrystalline NiTiHf shape memory alloys on post-mortem TEM samples, and reported that the crack propagates along a martensite band. The only work that combines analytical calculations using the strain energy density criterion with computational analyses via finite elements software ABAQUS, studies on an isotropic NiTi SMA material under mixed mode loading is the one reported by Mirsayar and Hartl [97].

During cyclic loading, the austenite-martensite interface parallel to the active martensite variant undergoes fatigue and a crack starts due to the continuous forward/reverse transformation in the martensite band. Deformation follows martensite bands where the strain is the highest, so one can expect fracture to occur parallel to the austenite-martensite interface where high shear stresses form. Stress concentrations occur at the austenite-martensite interfaces, resulting in eventual failure [93].

Fatigue crack growth tests on single crystal CoNiAl shape memory alloys also show that the crack grows along a similar angle to the initial crack from the notch despite some deviations due to micro-structural barriers [98]. Since the crack growth angle is an important parameter in determining the fracture behavior of shape memory alloys, the determination of the crack initiation angle is of great importance.

There are several works on the calculation of crack initiation angle in isotropic non-transforming materials that use maximum tangential stress [82], and strain energy density criteria [99] with modifications done to account for anisotropy [100]. However, there is not any complete work on the determination of crack initiation angle in single crystal shape memory alloys.

Single crystal CoNiAl shape memory alloy is used in this study. The single crystal CoNiAl specimen behaves anisotropically when loaded. In CoNiAl shape memory alloys, martensitic transformation occurs from body centered cubic austenite to face centered tetragonal martensite. Cubic to tetragonal deformation is accommodated by multiple martensite variants, usually one of them dominating, causing the macroscopically visible martensitic band on tension specimens [101]. In single crystal shape memory alloys, anisotropic material properties also strongly influence the martensitic transformation, and consequently affect the fracture behavior.

In this chapter, first experiments are conducted to observe the crack initiation in edge notched single crystal CoNiAl specimes. Following the experimental observation, the crack initiation angles are calculated analytically using the Generalized Maximum Tangential Stress (GMTS), the Maximum Energy Release Rate (MERR), and Strain Energy Density (SED) Criteria. Also, the edge notched cracked specimen is studied in detail using finite elements (ABAQUS). The martensite band angle is defined as a material anisotropy direction in the superelastic FE model, and the full strain, stress fields are plotted together with the transformation region. Results are found to be in accordance with the experimental observations and analytical calculations.

3.2. Experimental Observation of Crack Initiation From the Notch

3.2.1. Material and Specimens

CoNiAl samples are cut using Electric Discharge Machining (EDM) from single crystal $Co_{36}Ni_{35}Al_{29}(at.\%)$ bulk material (grown using the Bridgman technique in an inert environment). The [100] crystallographic orientation is chosen for the experi-

ments. Austenite finish (A_f) and martensite start (M_s) temperatures of the material as obtained from Differential Scanning Calorimetry (DSC) are A_f=40°C, and M_s=10°C, respectively [4]. The micro-structure consists of a cobalt rich secondary (γ) phase, and a matrix which is austenitic crystal in the super-elastic case, and martensitic upon transformation. The secondary phase does not undergo any phase transformation or reorientation [4]. To understand the mechanical behavior of the material, the dog-bone specimen shown in Figures 3.3 and 3.4 is used. Test specimens used for material characterization have a width=2.93 mm, a thickness=1.38 mm, and a gauge length=8 mm. A sketch of the tension specimens used for mechanical behavior determination tests is presented in Figure 3.1.

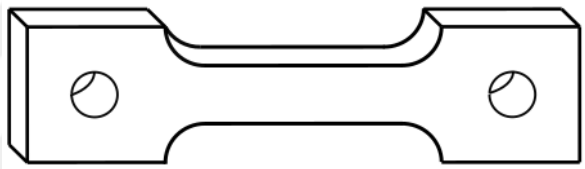

Figure 3.1. Sketch of the dog bone specimen used for mechanical behavior determination tests.

All the test specimens are homogenized at 1275 ^oC for 24 hours in a vacuum furnace, and left to cool in air. After the heat treatment, the material exhibits shape memory behavior at room temperature (T = 20 to 25 ^oC), and superelastic behavior at T = 50 ^oC in tension. All specimens are polished to a mirror surface finish using SiC paper up to P4000 and 1 μm suspended alumina, and a fine speckle pattern is obtained by air blasting 1000 grit SiC powder on the polished surface for full-field displacement and strain measurements using DIC.

3.2.2. Experimental Set-up

The experiments are conducted using a servo-hydraulic load frame equipped with a digital controller, and a computer program is used to control the load frame and to synchronize the acquisition of the DIC images that are captured with a CCD camera.

The digital camera has a resolution of 1600 x 1200 pixels, with a maximum frame rate of 15 fps, and an adjustable lens with a 12X magnification range and 2X adapter. For the image correlation and the strain calculations, a commercial software – Vic2d from Correlated Solutions, is used. Strains are monitored with DIC during the entire loading and unloading processes. The experimental set-up can be seen in Figure 3.2.

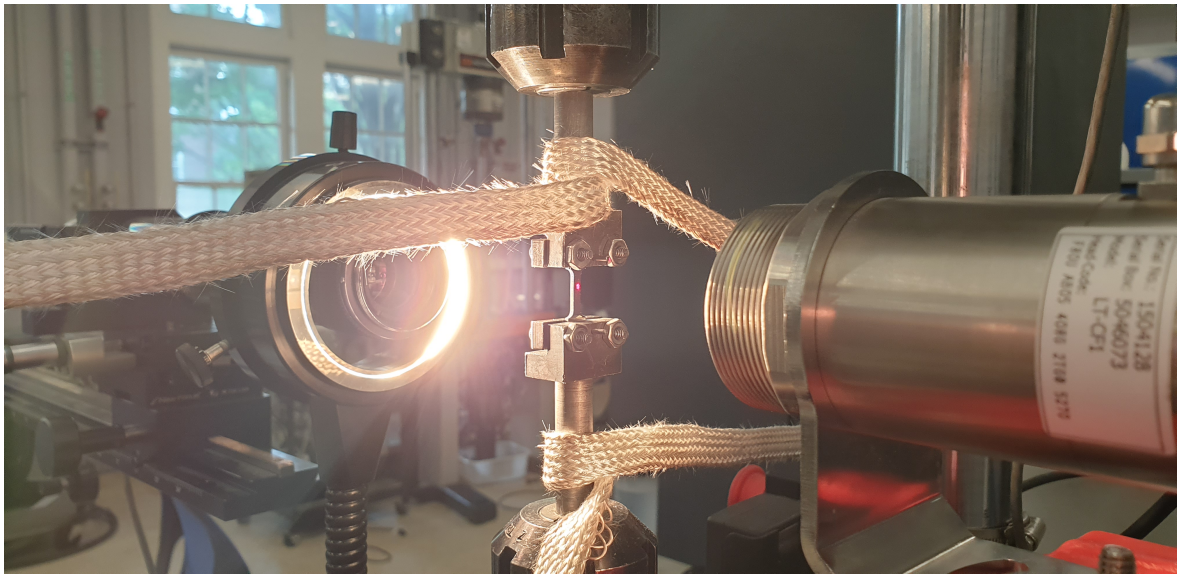

Figure 3.2. Test set-up. DIC camera, light source, heating tapes, the specimen position, and the temperature control unit.

3.2.3. Mechanical Behavior of CoNiAl

The first experiment is conducted at T = 50 ^oC. The specimen is heated to 50 ^oC using heating tapes. Then the specimen is loaded under position control to 0.25 mm elongation to observe the superelastic behavior and the hysteresis. In Figure 3.3 the stress & local strain diagram is plotted.

The strains are extracted from a region where they are maximum, namely the area of interest (AOI), shown with the black rectangle. Around the crack tip, as a result of martensitic phase transformation comparatively large strains occur before failure. As shown in Figure 3.3, the local strain is around 5%, while the global strain is

lower than 2%. A strain recovery of more than 90% proves a superelastic behavior; the material was in the austenitic phase at the beginning of the experiment and underwent martensitic transformation with forward transformation that started around a stress value of 115 MPa.

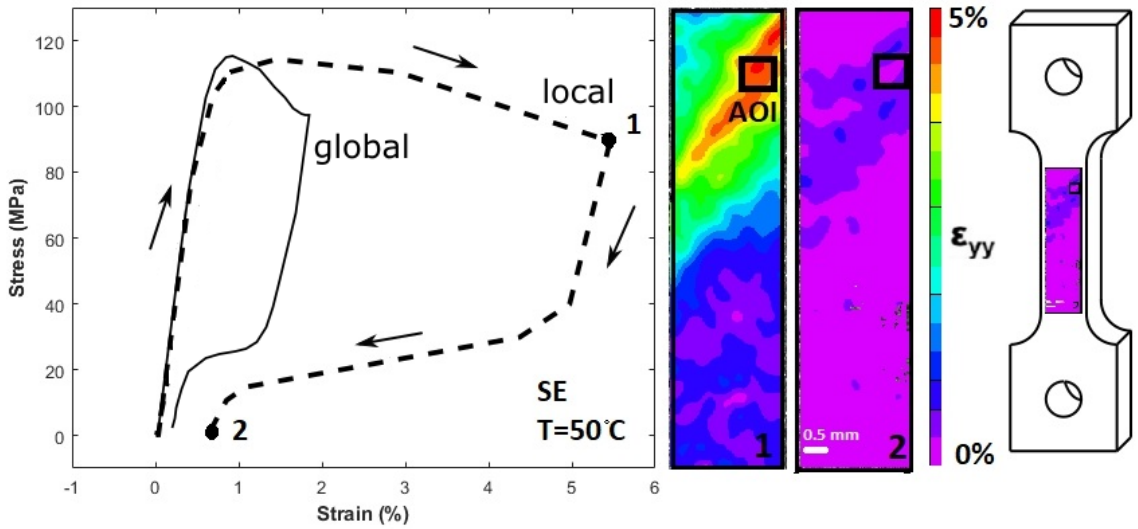

Figure 3.3. Stress–Strain behavior of the superelastic specimen (SE), T= 50 ^oC in tension. The strain is calculated from the mean of ϵ_{yy} extracted from the black framed region.

The second experiment is conducted at room temperature (T = 20 ^oC), and the specimen is loaded under position control to 0.2 mm elongation. The stress-strain curve is plotted in Figure 3.4. The material is in the martensitic phase and undergoes reorientation with loading as a result of the shape memory behavior.

The martensitic reorientation starts around a stress of 60 MPa. When the load is removed, the strain recovery is lower than 25% of the maximum strain ($1 \rightarrow 2$), which is then reduced to almost zero with heating to 100 C° ($2 \rightarrow 3$). Strains are calculated from DIC images taken with 2 second intervals, and the local strains belong to the region shown with the black frame, where a strain localization occurs. As shown in Figure 3.4, while the local strain is around 4%, the global strain is just about 1%.

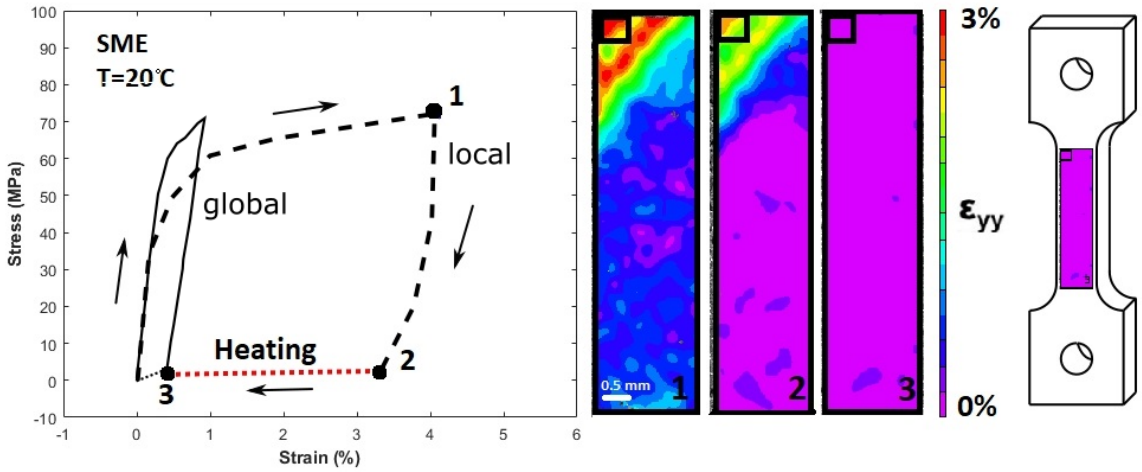

Figure 3.4. Stress – Strain behavior of the shape memory specimen (SM), T= 20 ^oC. The strain is calculated from the mean of the strains, ϵ_{yy}, extracted from the black framed region.

3.3. Crack Initiation Angle Evaluation

In crack growth experiments, 8-mm long edge-notched dog-bone specimens with an edge notch cut at the mid-section are used. The first superelastic (SE1) specimen has a gauge section width of 2.88 mm, a thickness of 1.32 mm; the second superelastic (SE2) specimen has a gauge section width of 2.93 mm, a thickness of 1.32 mm; the third sample, SE3, has a gauge section width=2.93 mm, thickness=1.28 mm, notch length=0.5 mm, notch width $\approxeq$ 0.3048 mm. The shape memory (SM) specimen has a width of 2.93 mm, and a thickness of 1.35 mm. Each edge notch is 0.5 mm long and is cut using EDM with a 0.1778 mm diameter wire [98].

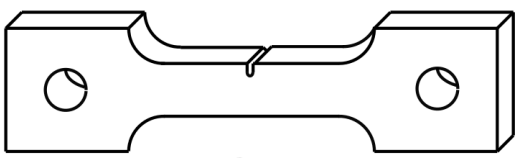

Figure 3.5. Edge-notched dog-bone specimen. A 0.5 mm notch is cut at the mid-section.

Stress controlled experiments are conducted at 50 ^oC at 3 Hz frequency, under a constant stress amplitude of 80.75 MPa with a R = 0.05 for the first two superelastic cases, and at room temperature (25 ^oC), under 57 MPa for the shape memory one. Crack initiation and subsequent growth are monitored during each cycle using a CCD camera focused on the area around the notch/crack tip. The displacement field that is extracted from the images is used to locate the sharp crack tip. After the initiation of a crack, the loading frequency is reduced to 0.2 Hz, and images around the crack tip are taken with the same CCD camera, and DIC data are collected.

In the first superelastic specimen, the crack initiated at the notch making an angle of $\approx 43^\circ$ with the x-coordinate as shown in Figure 3.6 after around 18000 loading cycles.

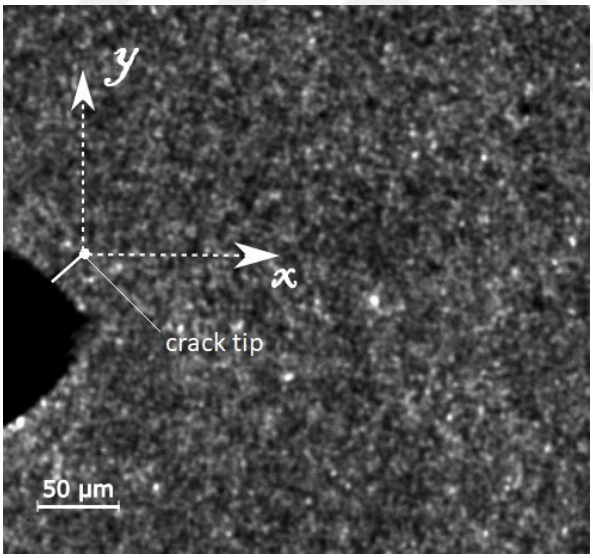

Figure 3.6. Crack initiation in the first superelastic specimen (SE1): Crack length = 0.027 mm.

A new experiment is conducted following similar conditions to the first one using the second superelastic specimen (SE2). This time the crack initiates at the notch at an angle of $\approx -42^\circ$ after 3000 cycles as shown in Figure 3.7, keeping approximately the same magnitude of crack initiation angle seen in the first specimen (SE1). A third superelastic experiment is conducted under cyclic loading at 3 Hz and a stress

amplitude of 66.5 MPa. A crack initiates at the notch at an angle of $\approx 44^{\circ}$ after 25000 cycles as shown in Figure 3.8.

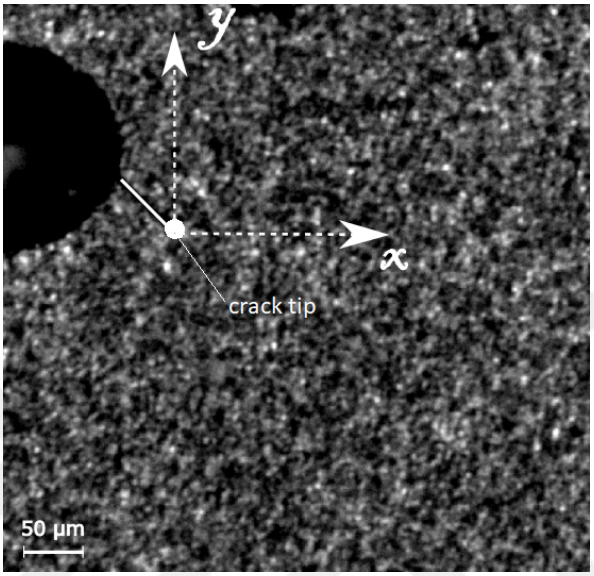

Figure 3.7. Crack initiation in the second superelastic specimen (SE2): Crack length = 0.0246 mm.

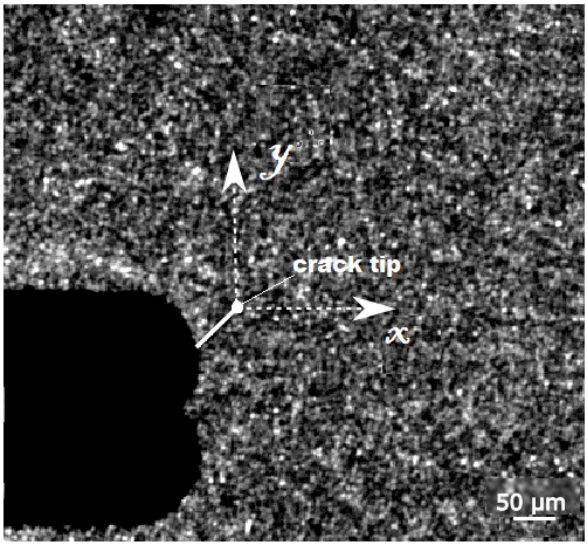

Figure 3.8. Crack initiation in the third superelastic specimen (SE3): Crack length = 0.073 mm.

The DIC images show the presence of a straight crack emanating from the notch (initial crack) in the shape memory specimen. A second straight crack (effective crack) as shown in Figure 3.9 shows up at around 80000 loading cycles. The initial crack at the bottom stops after the initiation of the effective crack at the notch.

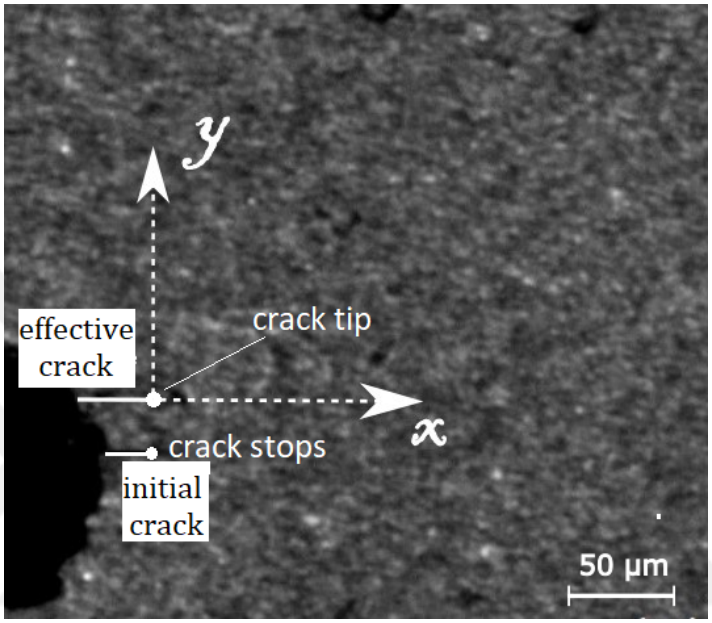

Figure 3.9. The initial and effective cracks in the shape memory specimen (SM): The effective crack length=0.0358 mm.

Since the crack initiation angle is 0° for the shape memory specimen, crack initiation angle calculations are only done for the superelastic specimens. To see the crack initiation from the notches of the superelastic specimens together, in Figure 3.10, DIC images of the initial cracks are presented. Image in Figure 3.10 (a) belongs to the first superelastic specimen; Figure 3.10 (b) presents initial crack in the third specimen. Figures 3.10 (c) & (d) present the crack initiations from the notch in the second specimen, where first a crack shown in Figure 3.10 (c) starts from the notch with an angle of $\theta_{SE3,1} \cong -42°$; later, a second crack initiates. The tests carried out on CoNiAl specimens show that the martensite localization bands have approximately the same angle as the notched specimen crack initiation angles.

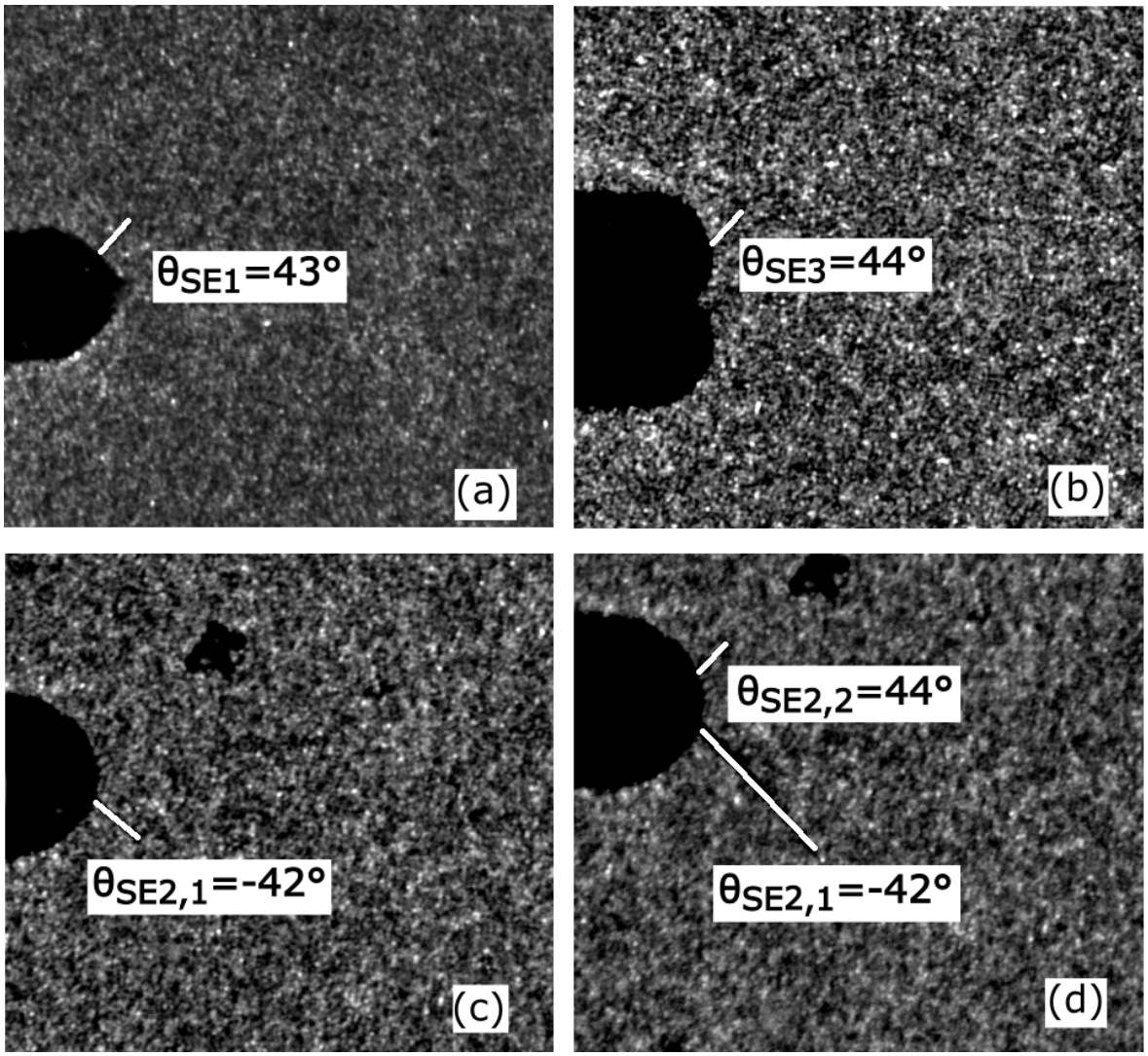

Figure 3.10. (a) Crack initiation in the first specimen, $\theta_{SE1} \approxeq 43°$; (b) the third specimen, $\theta_{SE3} \approxeq 44°$. (c) Initiation of the first crack in the second specimen, $\theta_{SE2,1} \approxeq -42°$; (d) second crack from the notch in the second specimen, $\theta_{SE2,2} \approxeq 44°$

3.4. Crack Initiation Angle Calculations

Apparently, the crack initiates and/or grows in the direction of the martensite band–austenite boundary which is also reported by other researchers [81, 92, 94–96]. The growing crack angle is strongly influenced by the orientation dependent properties of the single crystal SMA, which also affects the martensitic transformation band angles [92, 94].

A CoNiAl specimen is tested under uniaxial tension (y-direction), and ϵ_{yy} field is obtained using Digital Image Correlation (DIC). The strain distribution is plotted in Figure 3.11 (a) to show the martensite band angle $\boldsymbol{\phi}$. The angle of the martensite variant that activated in the CoNiAl tension specimen as a localization band (see Figure 3.11 (a)) is measured to be $\approxeq 41°$. The single crystal SMAs' mechanical behavior is affected as a result of the material anisotropy caused by the martensite transformation. To account for the anisotropy the martensite band angle found is used as the material orientation angle ($\phi \approxeq 41°$) throughout the calculations.

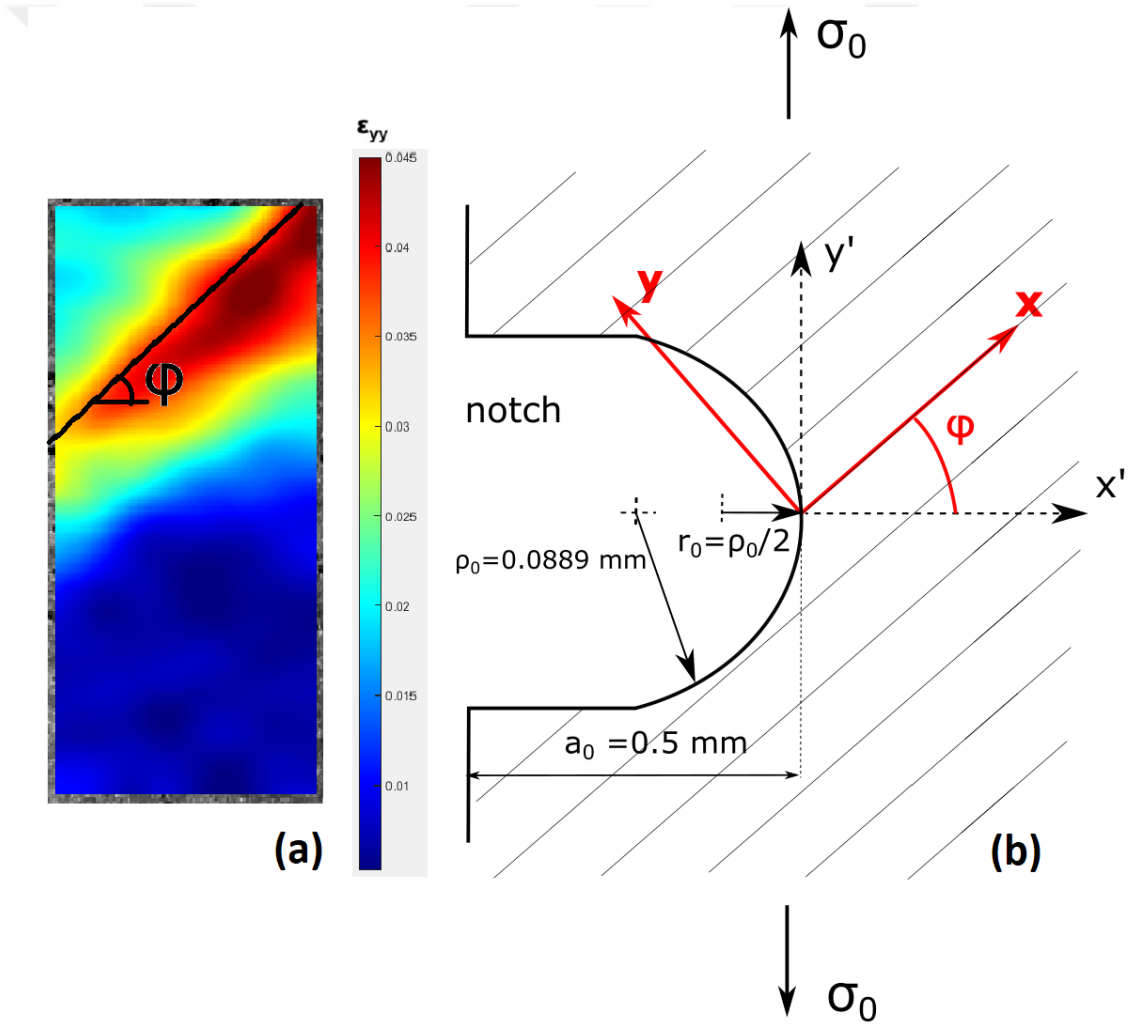

Figure 3.11. (a) Martensite localization band at $\approxeq 41°$. (b) Sketch of the notch. Material orientation angle $\phi = 41°$, and $\sigma_0 = 85$ MPa. x & y are material coordinates; x' & y' notch configuration coordinates (x' is along the notch).

In this section, an attempt to calculate the initiation angle of the crack that emanate from the notch into the anisotropic medium will be made. The tangential stress, the maximum energy release rate, and the strain energy density around the notch using equations of anisotropic elasticity will be calculated. In Figure 3.11, the geometry of the notch is presented.

Material properties are obtained from tensile tests, and the missing anisotropic compliance matrix components of the material are calculated using the anisotropic elasticity relations of cubic crystals as explained in detail in [94].

Table 3.1. Compliance matrix components in material coordinates.

a_{11} (MPa^{-1})	a_{22} (MPa^{-1})	a_{12} (MPa^{-1})	a_{16} (MPa^{-1})	a_{26} (MPa^{-1})	a_{66} (MPa^{-1})
$2.1395 \cdot 10^{-5}$	$2.1395 \cdot 10^{-5}$	$6.9596 \cdot 10^{-6}$	$8.0199 \cdot 10^{-6}$	$-8.0199 \cdot 10^{-6}$	$1.4104 \cdot 10^{-4}$

3.4.1. Stress Field in Anisotropic Media Around a Crack

The stress field for anisotropic materials around a crack in Cartesian coordinates are given as follows [102]:

$$\sigma_x = \frac{K_I}{\sqrt{2\pi r}} Re\left[\frac{s_1 s_2}{s_1 - s_2}\left(\frac{s_2}{\sqrt{cos\theta + s_2 sin\theta}} - \frac{s_1}{\sqrt{cos\theta + s_1 sin\theta}}\right)\right] + \frac{K_{II}}{\sqrt{2\pi r}} Re\left[\frac{1}{s_1 - s_2}\left(\frac{s_2^2}{\sqrt{cos\theta + s_2 sin\theta}} - \frac{s_1^2}{\sqrt{cos\theta + s_1 sin\theta}}\right)\right] \tag{3.1}$$

$$\sigma_y = \frac{K_I}{\sqrt{2\pi r}} Re\left[\frac{s_1 s_2}{s_1 - s_2}\left(\frac{1}{\sqrt{cos\theta + s_1 sin\theta}} - \frac{1}{\sqrt{cos\theta + s_2 sin\theta}}\right)\right] + \frac{K_{II}}{\sqrt{2\pi r}} Re\left[\frac{1}{s_1 - s_2}\left(\frac{s_1}{\sqrt{cos\theta + s_1 sin\theta}} - \frac{s_2}{\sqrt{cos\theta + s_2 sin\theta}}\right)\right] \tag{3.2}$$

$$\sigma_{xy} = \frac{K_I}{\sqrt{2\pi r}} Re\left[\frac{1}{s_1 - s_2}\left(\frac{s_1}{\sqrt{cos\theta + s_2 sin\theta}} - \frac{s_2}{\sqrt{cos\theta + s_1 sin\theta}}\right)\right] + \frac{K_{II}}{\sqrt{2\pi r}} Re\left[\frac{1}{s_1 - s_2}\left(\frac{1}{\sqrt{cos\theta + s_2 sin\theta}} - \frac{1}{\sqrt{cos\theta + s_1 sin\theta}}\right)\right] \tag{3.3}$$

and the stress field is transformed into polar coordinates as:

$$\sigma_r = \sigma_x cos^2\theta + \sigma_y sin^2\theta + \sigma_{xy} sin2\theta \tag{3.4}$$

$$\sigma_\theta = \sigma_x sin^2\theta + \sigma_y cos^2\theta - \sigma_{xy} sin2\theta \tag{3.5}$$

$$\sigma_{r\theta} = sin\theta cos\theta(\sigma_y - \sigma_x) + \sigma_{xy} cos2\theta. \tag{3.6}$$

Here, s_i are material properties in material coordinates (shown with "x, y" in Figure 3.11), and transformed into notch coordinates ("x', y'") as follows:

$$s_i = \frac{\mu_i cos\phi + sin\phi}{cos\phi - \mu_i sin\phi}, \quad (i = 1, 2), \tag{3.7}$$

where, μ_i are the roots of the following equation, which are always complex numbers and in the form of $\mu_i = \pm\xi + j\zeta$:

$$a_{11}\mu^4 - 2a_{16}\mu^3 + (2a_{12} + a_{66})\mu^2 - 2a_{26}\mu + a_{22} = 0. \tag{3.8}$$

Here a_{ij} are the compliance coefficients in Voigt notation [102], and are material parameters obtained from the tensile test results given in Section 3.2 in Figure 3.3. The missing anisotropic compliance matrix components of the material are calculated using the anisotropic elasticity relations as explained in detail in [94]. Material parameters used in this study are given in Table 3.1.

3.4.2. U-notches

Since the equations available are for sharp cracks, to determine the stress field around a notch tip, the notch stress intensity factors (NSIFs) are used for K_I and K_{II} in the calculations. Fracture behavior of u-notches are strongly dependent on the

geometrical parameters q and r_0 which are defined as [103]

$$q = 2(\pi - \gamma)/\pi, \tag{3.9}$$

$$\rho_0 = qr_0/(q-1). \tag{3.10}$$

Here ρ_0 is the radius of the notch tip, and 2γ is the notch opening angle which is $\gamma = 0$, and q=2 according to Equation (3.9) for u-shape notches. In Figure 3.12 a representation of these parameters is given around a u-notch tip. The area Ω encapsulates the region at the notch with the highest value of stress.

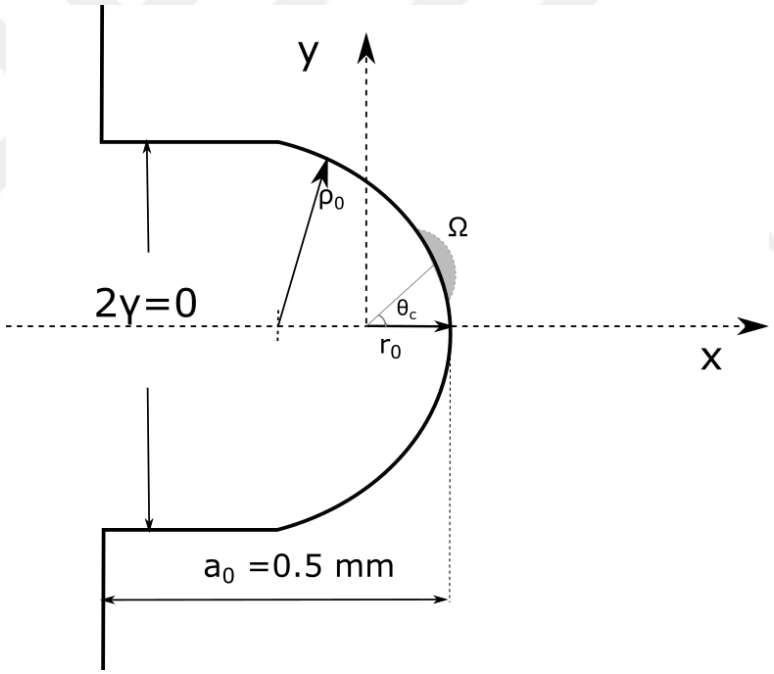

Figure 3.12. Representation of the control volume for critical region ahead of the notch. θ_c is the fracture angle from the notch tip.

The NSIFs are calculated as follows:

$$K_I = \sqrt{2\pi}\lim_{r\to 0}(\sigma_\theta)_{\theta=0} r^{1-\Lambda_1} = \Lambda_1\sqrt{2\pi}[(1+\Lambda_1) + \chi_{b_1}(1-\Lambda_1)]a_1 \tag{3.11}$$

$$K_{II} = \sqrt{2\pi}\lim_{r\to 0}(\sigma_{r\theta})_{\theta=0} r^{1-\Lambda_2} = -\Lambda_2\sqrt{2\pi}[(1-\Lambda_2) + \chi_{b_2}(1-\Lambda_2)]a_2. \tag{3.12}$$

For u-notches, $\Lambda_1 = \Lambda_2 = 0.5$, and $\chi_{b_1} = \chi_{b_2} = 1$. a_1 & a_2 are constants, and are dependent on the applied stress [103]. For the loading condition in the present work, the notch intensity factors are calculated as: $K_{II} = 0$, and $K_I = 110\ MPa\sqrt{mm}$.

3.4.3. Analytical Crack Initiation Angle Calculations

3.4.3.1. Generalized Maximum Tangential Stress (GMTS) Criterion. To calculate the crack initiation angle using the Generalized Maximum Tangential Stress criterion, the stress distribution around the crack tip for anisotropic materials for the case of plane stress initially obtained by Sih *et al.* [100] is utilized [104]:

$$\sigma_{rr} = \frac{K_{eff}}{\sqrt{\pi r}}\left[Re\left[\frac{1}{(s_1 - s_2)}\left(\frac{(\lambda + s_1\sqrt{1-\lambda^2})(sin\theta - s_2 cos\theta)^2}{\sqrt{cos\theta + s_2 sin\theta}} - \frac{(\lambda + s_2\sqrt{1-\lambda^2})(sin\theta - s_1 cos\theta)^2}{\sqrt{cos\theta + s_1 sin\theta}}\right)\right]\right], \tag{3.13}$$

$$\sigma_{\theta\theta} = \frac{K_{eff}}{\sqrt{\pi r}}\left[Re\left[\frac{1}{(s_1 - s_2)}\left((\lambda + s_1\sqrt{1-\lambda^2})(cos\theta + s_2 sin\theta)^{3/2} - (\lambda + s_2\sqrt{1-\lambda^2})(cos\theta + s_1 sin\theta)^{3/2}\right)\right]\right]. \tag{3.14}$$

Then, the critical tangential stress distribution is obtained as:

$$\sigma^c_{\theta\theta} = \sigma_{\theta\theta} + T sin^2\theta, \tag{3.15}$$

where "T" is the T-stress, and is calculated as:

$$T = \sigma_{rr} - \sigma_{\theta\theta}. \tag{3.16}$$

Here K_{eff} is the effective stress intensity factor, r and θ are the polar coordinates, λ is the mode-mixity parameter, and s_i are obtained from Equation (3.7). Effective stress intensity factors are obtained as follows:

$$K_{eff} = \sqrt{(K_I)^2 + (K_{II})^2}, \tag{3.17}$$

and the mode mixity parameter "λ" is obtained as:

$$\lambda = \frac{K_{II}}{K_{eff}}. \tag{3.18}$$

Crack grows in the direction of the angle θ_c at a constant radius along which the tangential stress is maximum:

$$\frac{\partial \sigma^c_{\theta\theta}}{\partial \theta} = 0, \qquad \frac{\partial^2 \sigma^c_{\theta\theta}}{\partial \theta^2} < 0 \qquad \rightarrow \theta = \theta_c \tag{3.19}$$

The tangential stress stress distribution is plotted as a function of the angle θ in Figure 3.13. The tangential stress function gives two local maxima. The crack grows in the direction of the larger one, which is $\theta_c \approxeq 42.3°$.

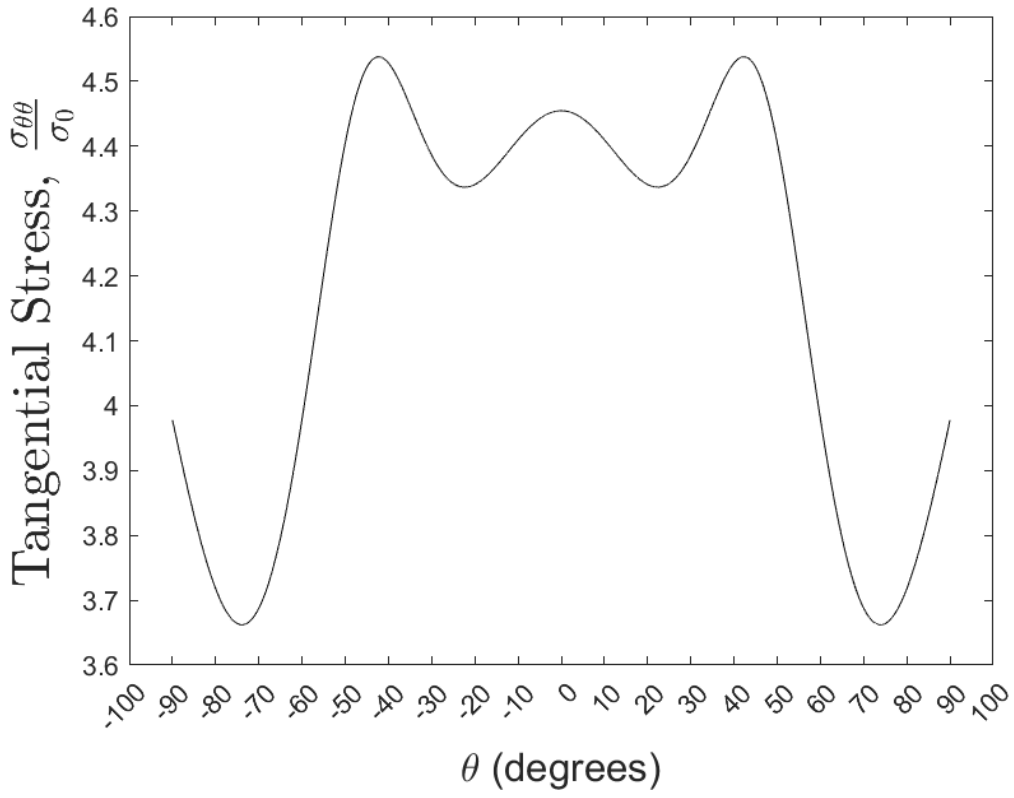

Figure 3.13. Distribution of tangential stress around the crack tip for anisotropic superelastic material, maximum $\sigma_{\theta\theta}$ occurs at $\theta_c \approxeq 42.3^o$.

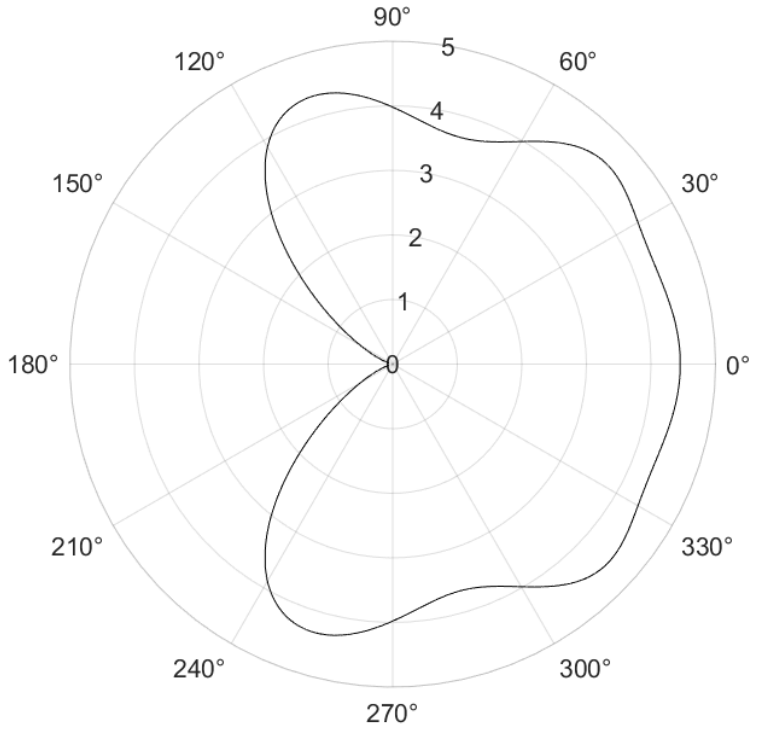

Figure 3.14. Distribution of tangential stress around the crack tip for anisotropic superelastic material $\theta_c \approxeq 42.3^o$; polar plot.

3.4.3.2. Maximum Energy Release Rate (MERR) Criterion. As a second attempt, the energy release rate for linearly elastic anisotropic materials is calculated using the equation initially given by Yang and Yuan [105] which is cited by Sakha *et al.* [104]:

$$\mathcal{G}(\theta) = \frac{1}{2}\mathbf{k}^{(k)^T}\mathbf{L}\mathbf{k}^{(k)} \tag{3.20}$$

The energy release rate $\mathcal{G}$ was put into this form after comprehensive derivations by substituting the corresponding anisotropic stress and displacement expressions into the equation given by Azhdari and Nemat-Nasser [106]:

$$\mathcal{G} = \lim_{\delta \to 0} \frac{1}{\delta} \int_0^{\delta} \Big[\sigma_{yy}(r,0) \cdot u_y(\delta - r, \pi) + \sigma_{xy}(r,0) \cdot u_x(\delta - r, \pi)\Big] dr. \tag{3.21}$$

In Equation (3.20), $\mathbf{k}^{(k)}$ is a vector containing the mode I & II stress intensity factors, where the exponent "(k)" means the stress intensity vector $\mathbf{k}$ is for the kink, $\mathbf{L}$ is a tensor that is related to the elastic material properties given in Equation (3.22), and "T" stands for the transpose of the vector $\mathbf{k}$. Calculations of each parameter are given by Sakha *et al.* [104] as follows:

$$\begin{aligned}
\mathbf{L} &= \frac{a_{11}}{E}\begin{bmatrix} cos\theta & sin\theta \\ -sin\theta & cos\theta \end{bmatrix}\begin{bmatrix} Im(s_1+s_2) & Im(s_1s_2) \\ Im(s_1s_2) & Im(s_1s_2(\bar{s_1}+\bar{s_2})) \end{bmatrix}\begin{bmatrix} cos\theta & -sin\theta \\ sin\theta & cos\theta \end{bmatrix} \\
&= \begin{bmatrix} L_{11} & L_{12} \\ L_{21} & L_{22} \end{bmatrix}, \qquad (3.22)
\end{aligned}$$

$$\mathbf{k}^{(k)} = \begin{bmatrix} K_{II}^k \\ K_I^k \end{bmatrix} = K_{eff}\left(\begin{bmatrix} C_{22} & C_{21} \\ C_{12} & C_{11} \end{bmatrix}\begin{bmatrix} \lambda \\ \pm\sqrt{1-\lambda^2} \end{bmatrix} + \frac{T\sqrt{r}}{K_{eff}}\begin{bmatrix} b_2 \\ b_1 \end{bmatrix}\right), \qquad (3.23)$$

$$C_{11} = Re\left[\frac{1}{(s_1-s_2)}\left(s_1(cos\theta+s_2sin\theta)^{3/2} - s_2(cos\theta+s_1sin\theta)^{3/2})\right)\right], \qquad (3.24)$$

$$C_{12} = Re\left[\frac{1}{(s_1-s_2)}\left((cos\theta+s_2sin\theta)^{3/2} - (cos\theta+s_1sin\theta)^{3/2})\right)\right], \qquad (3.25)$$

$$\begin{aligned}
C_{21} &= Re\left[\frac{1}{(s_1-s_2)}\left(s_1(sin\theta - s_2cos\theta)(cos\theta+s_2sin\theta)^{1/2}\right.\right. \\
&- \left.\left. s_2(sin\theta - s_1cos\theta))(cos\theta+s_1sin\theta)^{1/2}\right)\right], \qquad (3.26)
\end{aligned}$$

$$\begin{aligned}
C_{22} &= Re\left[\frac{1}{(s_1-s_2)}\left((sin\theta - s_2cos\theta)(cos\theta+s_2sin\theta)^{1/2}\right.\right. \\
&- \left.\left. (sin\theta - s_1cos\theta))(cos\theta+s_1sin\theta)^{1/2}\right)\right], \qquad (3.27)
\end{aligned}$$

$$b_1 = \sqrt{\frac{8}{\pi}}sin^2\theta, \qquad (3.28)$$

$$b_2 = -\sqrt{\frac{8}{\pi}}sin\theta cos\theta. \qquad (3.29)$$

The crack initiates in the direction of maximum energy release rate.

$$\frac{\partial \mathcal{G}(\theta)}{\partial\theta} = 0, \qquad \frac{\partial^2\mathcal{G}(\theta)}{\partial\theta^2} < 0 \qquad \rightarrow \theta = \theta_c \qquad (3.30)$$

In Figure 3.15 the energy release rate, $\mathcal{G}(\theta)$, is plotted as a function of the polar angle θ.

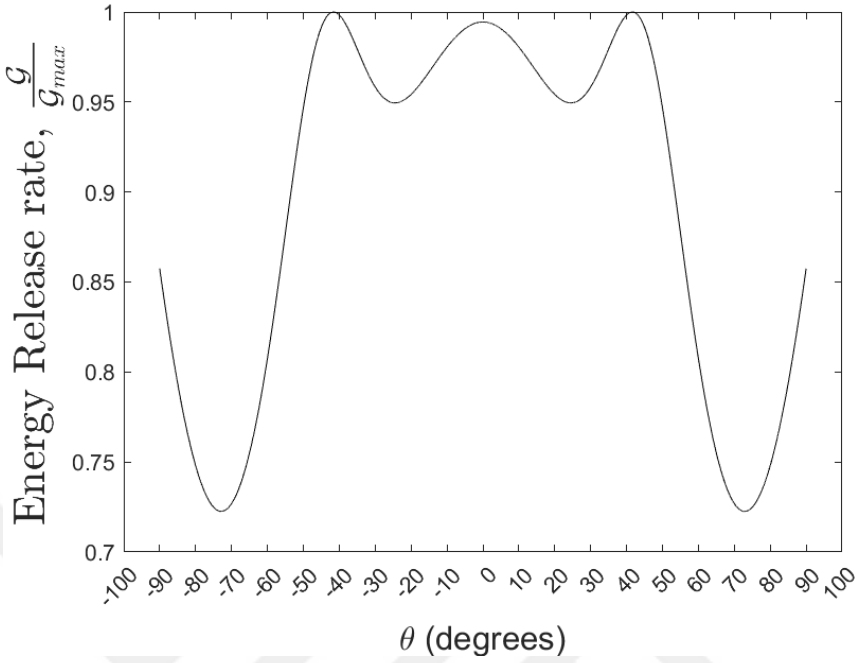

Figure 3.15. Distribution of energy release rates around the crack tip as a function of θ, the maximum occurs at $\theta_c \approxeq 41.6°$.

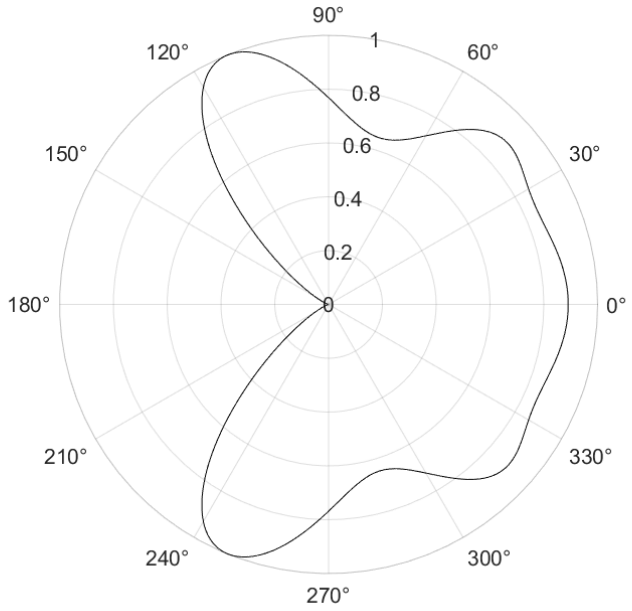

Figure 3.16. Distribution of energy release rates around the crack tip as a function of θ, the maximum occurs at $\theta_c \approxeq 41.6°$; polar plot.

The energy release rate has two local maxima, the crack advances in the direction of the larger one, which is $\approxeq 41.6°$.

3.4.3.3. Strain Energy Density (SED) Criterion. The distribution of strain energy density around the notch is calculated using the following strain energy density function [102]:

$$\frac{dU}{dV} = \frac{S}{r}. \tag{3.31}$$

The strain energy density factor "S" for anisotropic materials for the case of generalized plane stress is obtained in the following form using the anisotropic stress field equations and the derivations given by Gdoutos *et al.* [102]:

$$S(\theta) = \frac{1}{\pi}(A_{11}k_1^2 + 2A_{12}k_1k_2 + A_{22}k_2^2), \tag{3.32}$$

Here, k_1 and k_2 are calculated from

$$k_1 = \frac{K_I}{\sqrt{\pi}}, \qquad k_2 = \frac{K_{II}}{\sqrt{\pi}}; \tag{3.33}$$

and, A_{ij} are defined as follows:

$$A_{11} = \frac{1}{4}\Big[\quad a'_{11}A^2 + a'_{22}C^2 + a'_{66}E^2 + 2a'_{12}AC + 2a'_{16}AE + 2a'_{26}CE\Big], \tag{3.34}$$

$$A_{12} = \frac{1}{4}\Big[\quad a'_{11}AB + a'_{22}CD + a'_{66}EF + a'_{12}(AD + BC) + a'_{16}(AF + BE) + a'_{26}(CF + DE)\Big], \tag{3.35}$$

$$A_{22} = \frac{1}{4}\Big[\quad a'_{11}B^2 + a'_{22}D^2 + a'_{66}F^2 + 2a'_{12}BD + 2a'_{16}BF + 2a'_{26}DF\Big]. \tag{3.36}$$

In the Equation (3.33), K_I and K_{II} are the notch stress intensity factors that are calculated using Equations (3.11) and (3.12) by [103], and correspond to mode I and

mode II loading, respectively. Additionally,

$$A = Re\left[\frac{s_1 s_2}{s_1 - s_2}\left(\frac{s_2}{z_2} - \frac{s_1}{z_1}\right)\right], \tag{3.37}$$

$$B = Re\left[\frac{1}{s_1 - s_2}\left(\frac{s_2^2}{z_2} - \frac{s_1^2}{z_1}\right)\right], \tag{3.38}$$

$$C = Re\left[\frac{1}{s_1 - s_2}\left(\frac{s_1}{z_2} - \frac{s_2}{z_1}\right)\right], \tag{3.39}$$

$$D = Re\left[\frac{1}{s_1 - s_2}\left(\frac{1}{z_2} - \frac{1}{z_1}\right)\right], \tag{3.40}$$

$$E = Re\left[\frac{s_1 s_2}{s_1 - s_2}\left(\frac{1}{z_1} - \frac{1}{z_2}\right)\right], \tag{3.41}$$

$$F = Re\left[\frac{1}{s_1 - s_2}\left(\frac{s_1}{z_1} - \frac{s_2}{z_2}\right)\right]; \tag{3.42}$$

where s_i are obtained from Equation (3.7), and z_i are defined as:

$$z_i = \sqrt{cos\theta + s_i sin\theta}, \quad (i = 1, 2). \tag{3.43}$$

Compliance matrix components a_{ij} are transformed into crack coordinates using the following equations:

$$\begin{aligned}
a'_{11} &= a_{11}cos^4\phi + (2a_{12} + a_{66})sin^2\phi\, cos^2\phi \\
&+ a_{22}sin^4\phi + (a_{16}cos^2\phi + a_{26}sin^2\phi)sin2\phi, \\
a'_{22} &= a_{11}sin^4\phi + (2a_{12} + a_{66})sin^2\phi\, cos^2\phi \\
&+ a_{22}cos^4\phi - (a_{16}sin^2\phi + a_{26}cos^2\phi)sin2\phi, \\
a'_{12} &= a_{12} + (a_{11} + a_{22} - 2a_{12} - a_{66})sin^2\phi\, cos^2\phi \\
&+ \frac{1}{2}(a_{26} - a_{16})sin2\phi\, cos2\phi, \\
a'_{66} &= a_{66} + 4(a_{11} + a_{22} - 2a_{12} - a_{66})sin^2\phi\, cos^2\phi \\
&+ 2(a_{26} - a_{16})sin2\phi\, cos2\phi, \\
a'_{16} &= \left[a_{22}sin^2\phi - a_{11}cos^2\phi + \frac{1}{2}(2a_{12} + a_{66})cos2\phi\right]sin2\phi \\
&+ a_{16}cos^2\phi(cos^2\phi - 3sin^2\phi) + a_{26}sin^2\phi(3cos^2\phi - sin^2\phi), \\
a'_{26} &= \left[a_{22}cos^2\phi - a_{11}sin^2\phi - \frac{1}{2}(2a_{12} + a_{66})cos2\phi\right]sin2\phi
\end{aligned}$$

$$+ \quad a_{16}sin^2\phi(3cos^2\phi - sin^2\phi) + a_{26}cos^2\phi(cos^2\phi - 3sin^2\phi); \tag{3.44}$$

where "ϕ" is the material orientation angle as shown in Figure 3.11 (b).

For anisotropic materials, crack grows in the direction of the angle θ_c along which the strain energy density has a local maximum [104,107–109] that is calculated following the conditions which are given as:

$$\frac{\partial S(\theta)}{\partial \theta} = 0, \qquad \frac{\partial^2 S(\theta)}{\partial \theta^2} < 0 \qquad \rightarrow \theta = \theta_c. \tag{3.45}$$

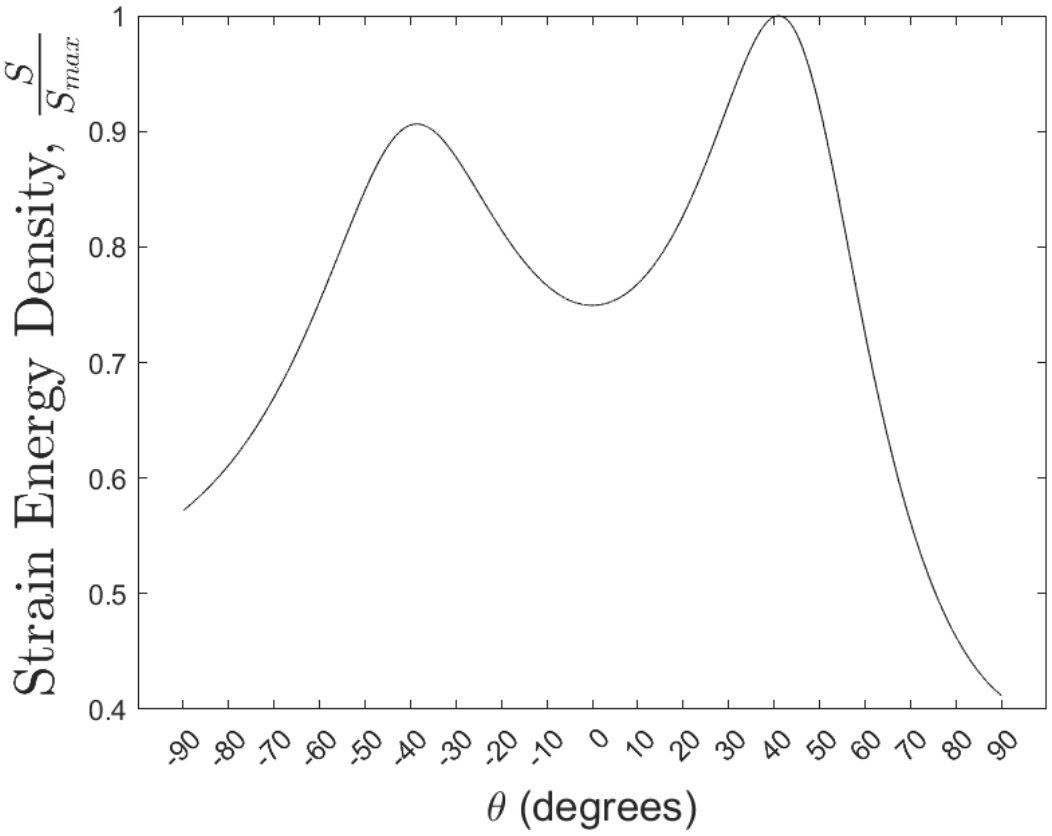

Figure 3.17. Distribution of strain energy density around the crack tip for anisotropic superelastic material, maximum occurs at $\theta_c \approxeq 40.9^o$.

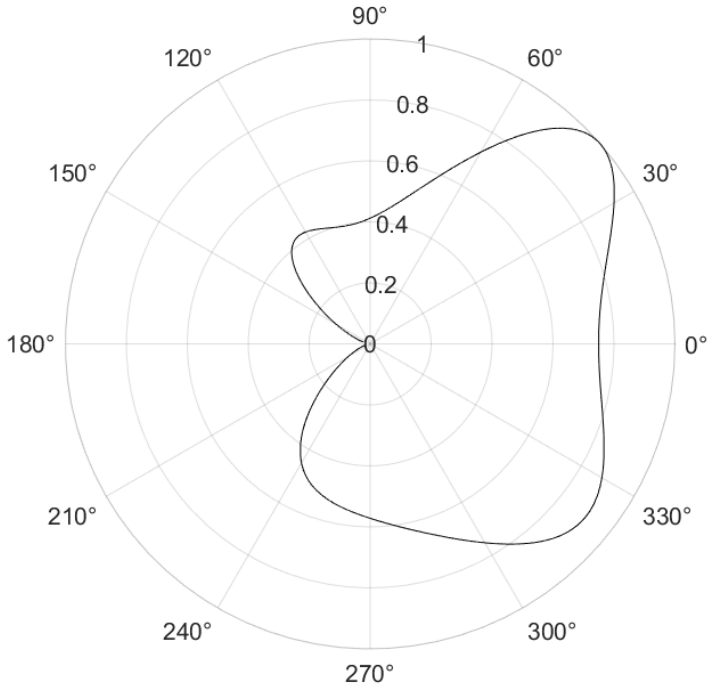

Figure 3.18. Distribution of strain energy density around the crack tip for anisotropic superelastic material; polar plot.

Strain energy density factor, S given in Equation (3.32) is plotted as a function of the angle θ in Figure 3.17. Where two local maxima are observed, with the larger one occurring at an angle of $\theta_c \approxeq 40.9°$. In all three calculations in Section 3.4, the results are found to be in accordance with the experimental observations outlined in Section 3.2.

3.4.4. Prediction of the Crack Initiation Angle Using Finite Elements

3.4.4.1. Finite Elements Model. A finite element model is constructed using ABAQUS utilizing four-node bilinear plane stress quadrilateral (CPS4) elements. The material is defined using the built-in material subroutine for SMAs [86] with the material properties obtained from tension experiments of the anisotropic superelastic CoNiAl, and a material orientation angle of $\phi = 41°$ is assigned. The SMA material properties are tabulated in Table 3.2.

Table 3.2. Finite element model material properties of the CoNiAl SMA.

E_A (MPa)	ν_A	E_M (MPa)	ν_M	ϵ^L (%)	σ^S_{tL} (MPa)	σ^E_{tL} (MPa)	σ^S_{tU} (MPa)
20000	0.43	18000	0.43	6.3	115	138	35
σ^E_{tU} (MPa)	σ^S_{cL} (MPa)	T_0 (°C)	$(\frac{\delta\sigma}{\delta T})_L$ (MPa/°C)	$(\frac{\delta\sigma}{\delta T})_U$ (MPa/°C)	σ^P_1 (MPa)	ϵ_1 (%)	
15	200	50	1.3	4.2	400	9.7	

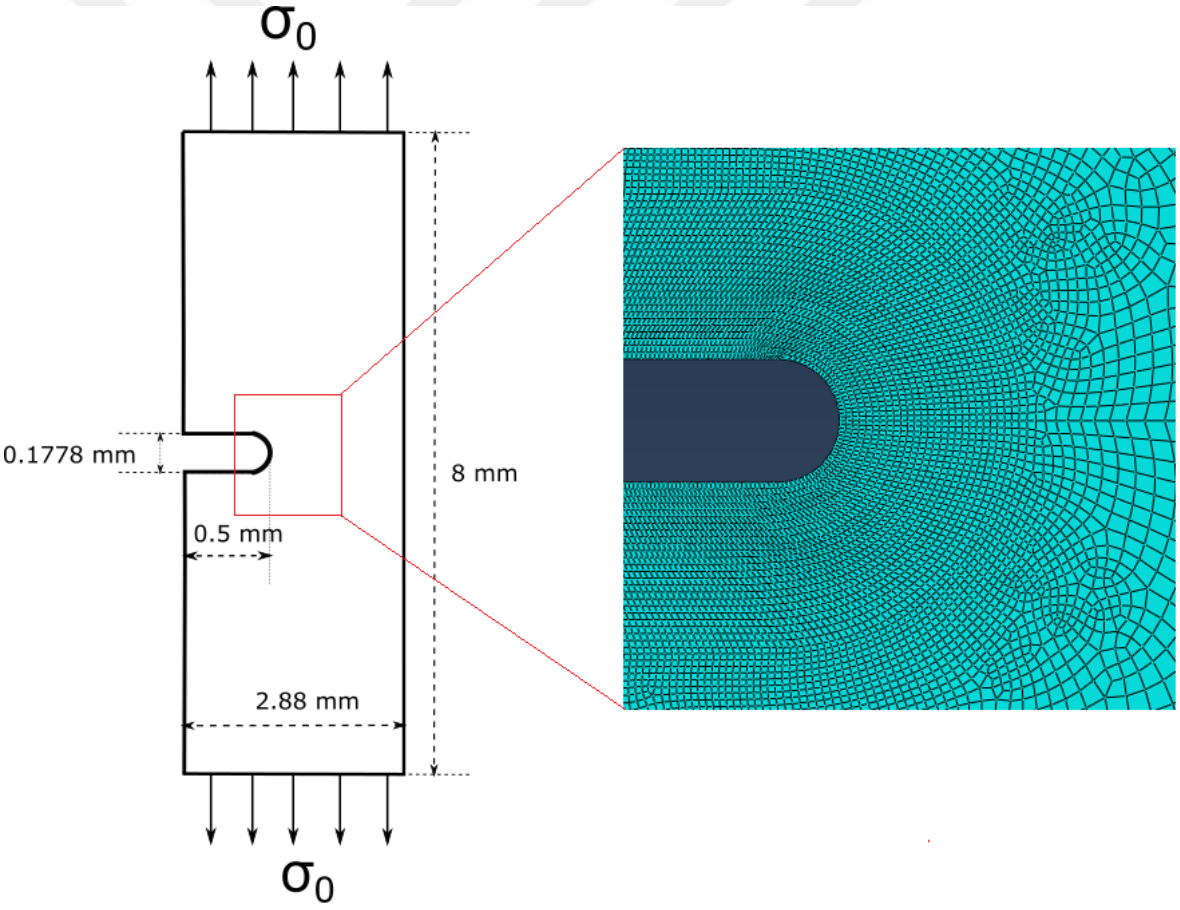

Figure 3.19. Geometry, mesh, and loading of the finite element model. Plane stress assumption. Global and material coordinates presented in Figure 3.11 are used.

The problem geometry and the mesh used in ABAQUS are shown in Figure 3.19. A finer mesh is used around the notch tip with an approximate element size of 0.01 mm.

The plate is loaded with uniform traction of up to 85 MPa: the maximum stress of one loading cycle. As a result, the stresses around the notch do not exceed the yield stress of martensite (σ_1^P), and no plastic deformation occurs. Full stress and strain fields and the strain energy density are calculated to study further the mechanical response of the notched single-crystal transforming material.

3.4.4.2. Tangential Stress Field Around the Notch & Crack. Two analyses were performed, first with a notch and then with a 0.015 mm long sharp crack coming out of the notch. The maximum tangential stress contours around the notch are plotted in Figure 3.20, and 3.21. In the u-notch specimens, the crack follows θ_c, which is the angle between r_0 and the region at the notch with the highest value of stress.

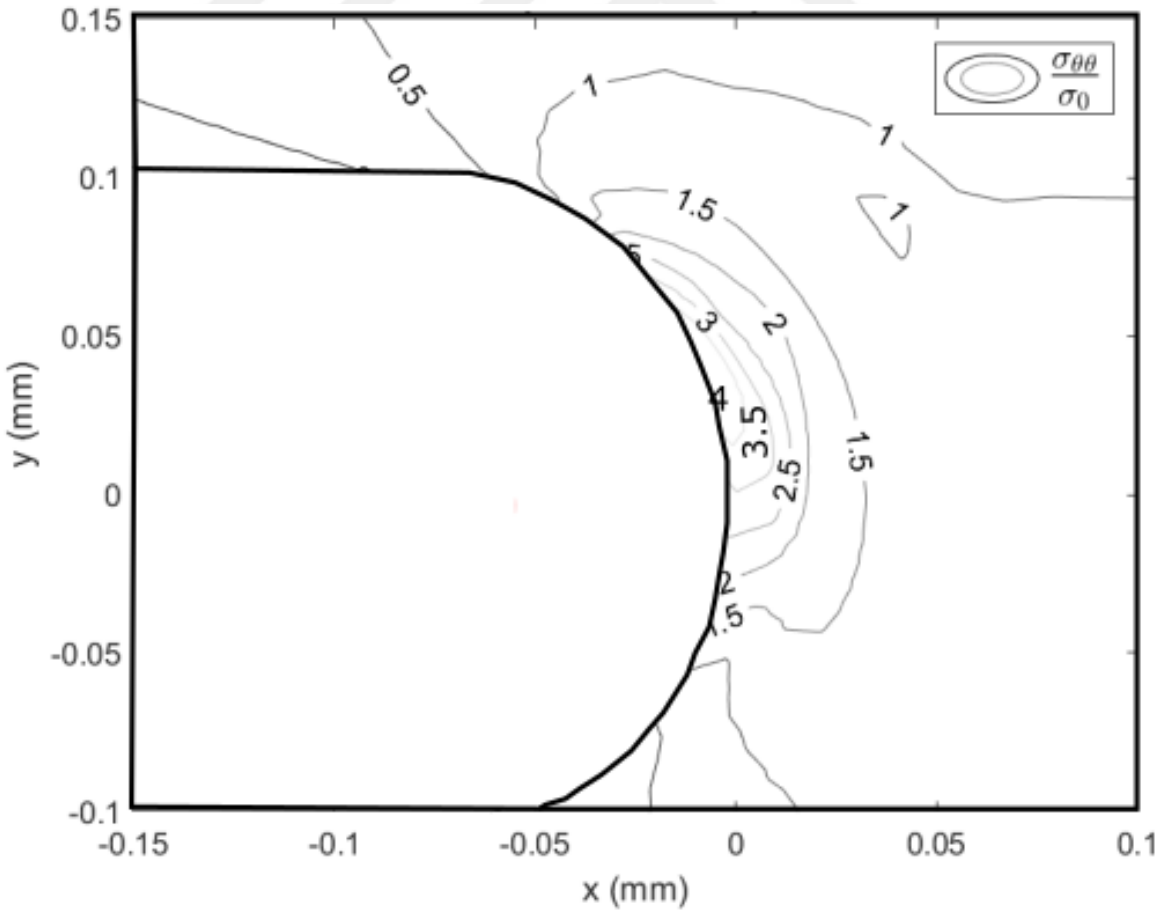

Figure 3.20. Tangential stress contours around the notched specimen model. Anisotropic superelastic material, maximum occurs at $\theta_c \cong 41.3°$.

As seen in Figure 3.20, the tangential stress distribution around the notch is not symmetric. Since the maximum of $\sigma_{\theta\theta}$ occurs at an angle of 41.3°, the stress contours also shift from the notch tip with the same angle. A small crack of length 0.015 mm emanating from the notch at the angle where the maximum tangential stress is found in Figure 3.20, is introduced to the same model. It is clear in Figure 3.21 the maximum tangential stress occurs at the crack tip as expected, and the stress distribution in this case forms asymmetrically as well, at an angle of 41° from the global x-coordinate.



Figure 3.21. Tangential stress contours. Crack propagation from the pre-crack (a=0.015 mm). Anisotropic superelastic material model, $\theta_c \approxeq 41°$ measured from the crack tip to the maximum point on the stress contour with respect to the global x-direction.

To see the difference in tangential stress distributions between anisotropic and isotropic material models, an isotropic superelastic CoNiAl is modeled and the tangen-

tial stress contours around the notch are plotted in Figure 3.22, in which the maximum tangential stress occurred at $\theta = 0°$. Unsurprisingly, in the isotropic superelastic Co-NiAl model the tangential stress contours form symmetrically with respect to the notch tip, and the crack is expected to initiate from the notch tip, then grow in a straight line.

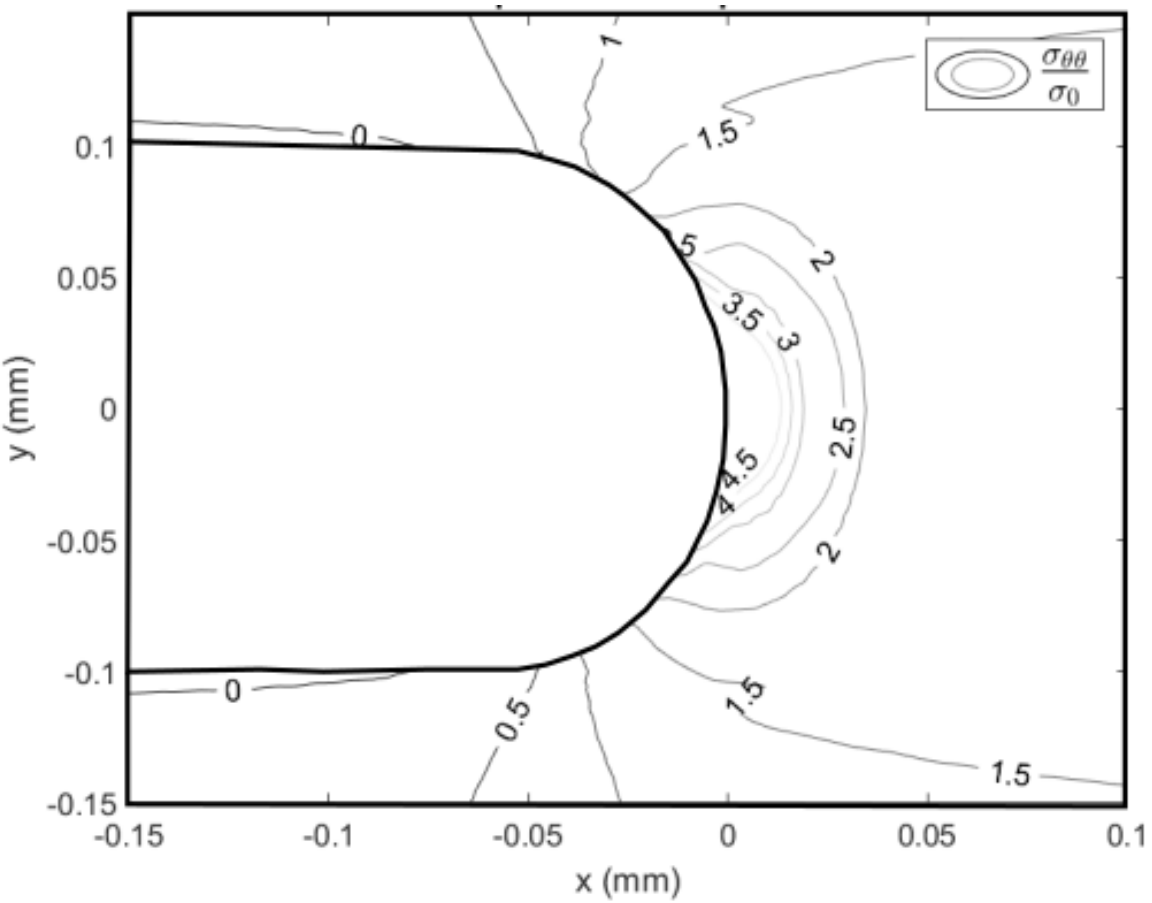

Figure 3.22. Tangential stress contours around the notch. Isotropic superelastic material model, $\theta_c = 0°$.

3.4.4.3. Strain Energy Density Distribution. In Figure 3.23 the strain energy density distribution around the notch is plotted. θ_c gives the angle where the strain energy density is maximum. In the model, while the maximum tangential stress occurs at $\approxeq 41.3°$, the maximum strain energy density is found at an angle of $\approxeq 38°$.

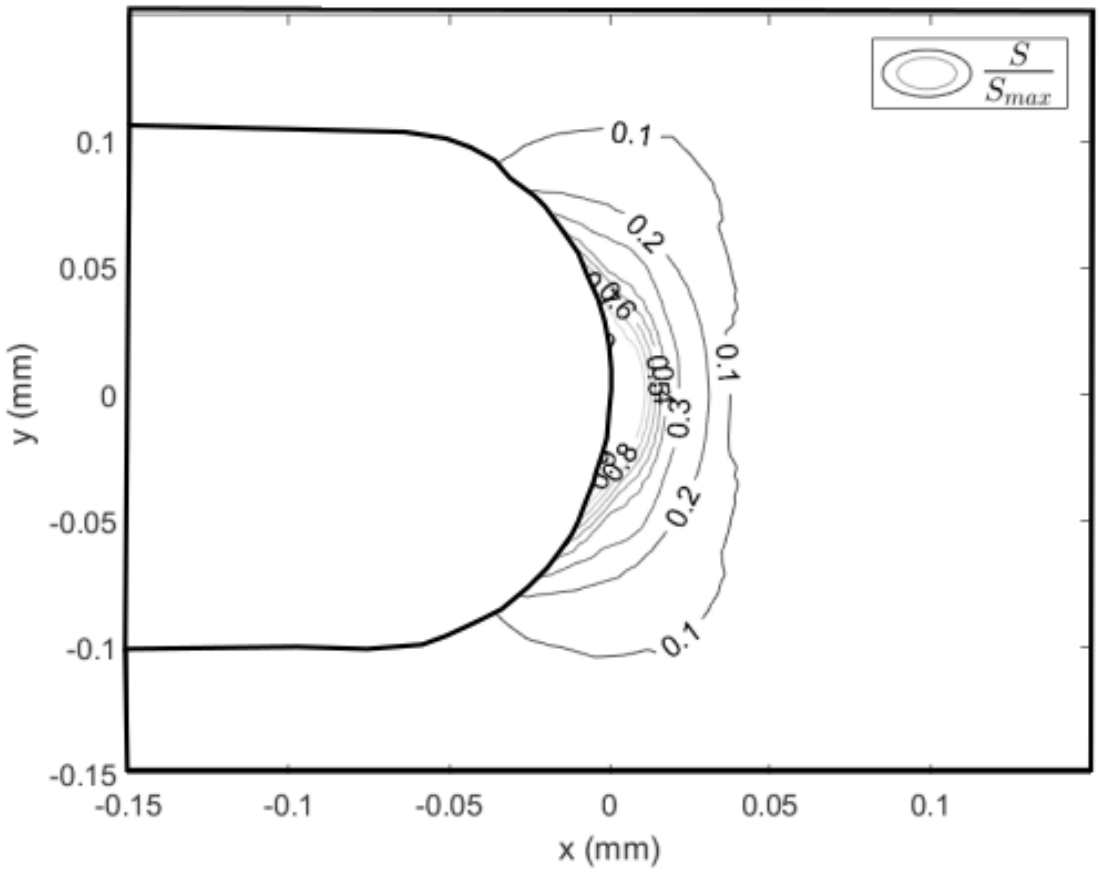

Figure 3.23. Strain energy density (SENER) around the notch. Anisotropic superelastic material model, $\theta_c \approxeq 38°$.

3.4.4.4. Determination of Martensitic Transformation Region. Equivalent strains are calculated from the strain field obtained from ABAQUS utilizing the equation:

$$\epsilon_{eqv} = \sqrt{\frac{2}{3}(\epsilon_{xx}^2 + \epsilon_{yy}^2 + 2\epsilon_{xy}^2)}. \tag{3.46}$$

Equivalent strain contours around the notch & crack tips of the superelastic anisotropic CoNiAl plates are plotted in Figures 3.24 and 3.25. Here, the regions inside the 0.01 strain contours correspond to the transformation zone where the austenite and martensite phases exist together, and the areas inside the 0.062 strain contours correspond to the full martensitic zones. The strain value of 0.01 is the martensitic transformation start strain which is obtained from the stress-strain curve presented in

Figure 3.3, and the strain value of 0.062 is the martensitic transformation finish strain reported by [5] for CoNiAl SMAs with [100] crystallographic orientation under tensile loading. As seen in the corresponding figures, the transformation region around the crack tip is much smaller than the one around the notch due to the fast increase of stress to yield, that is caused by the singularity. Additionally, since the crack length is very small, stresses at the notch are still high, resulting in martensitic transformation.

In Figures 3.26 and 3.27, martensitic transformation regions as given by ABAQUS are shown. Upon comparing the equivalent strain contours presented in Figures 3.24 and 3.25, it is apparent that utilizing equivalent strain for the purpose of approximating the martensitic transformation regions surrounding notches and cracks yields good results. Based on this observation, it appears that the assumption mentioned earlier could be useful when determining the transformation region.

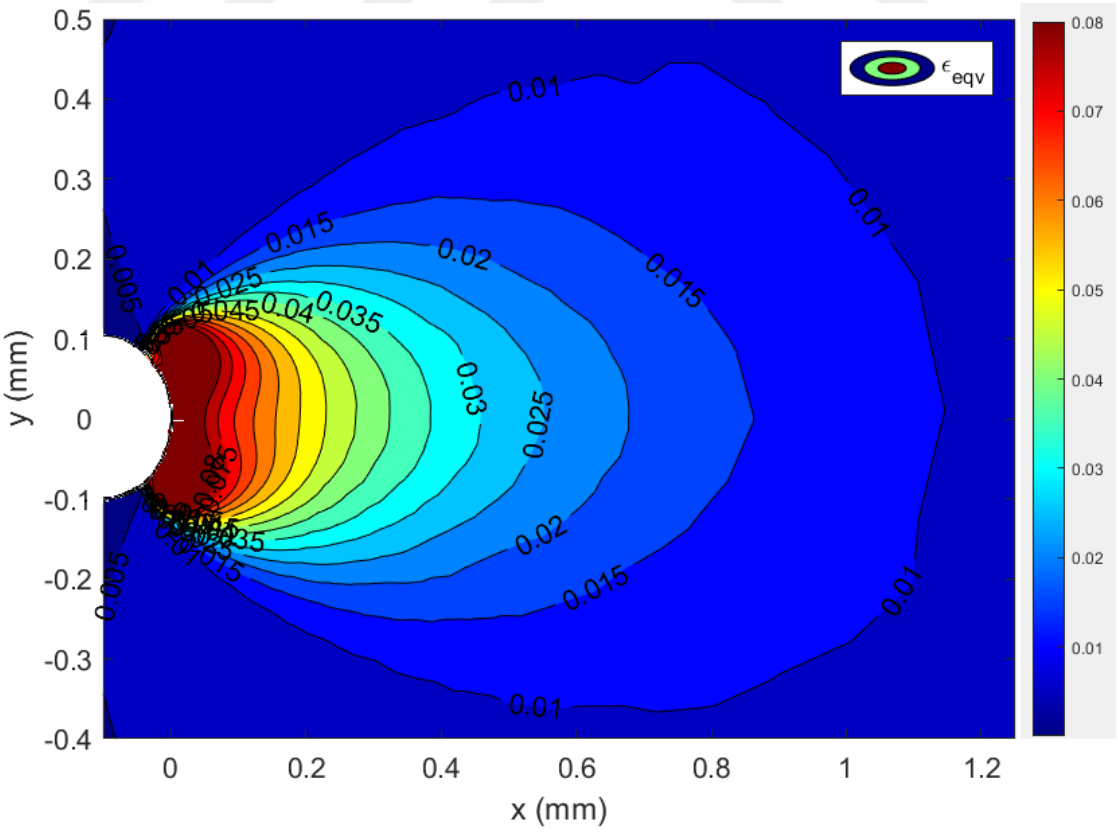

Figure 3.24. Equivalent strain contours around the notch. Anisotropic superelastic material model.

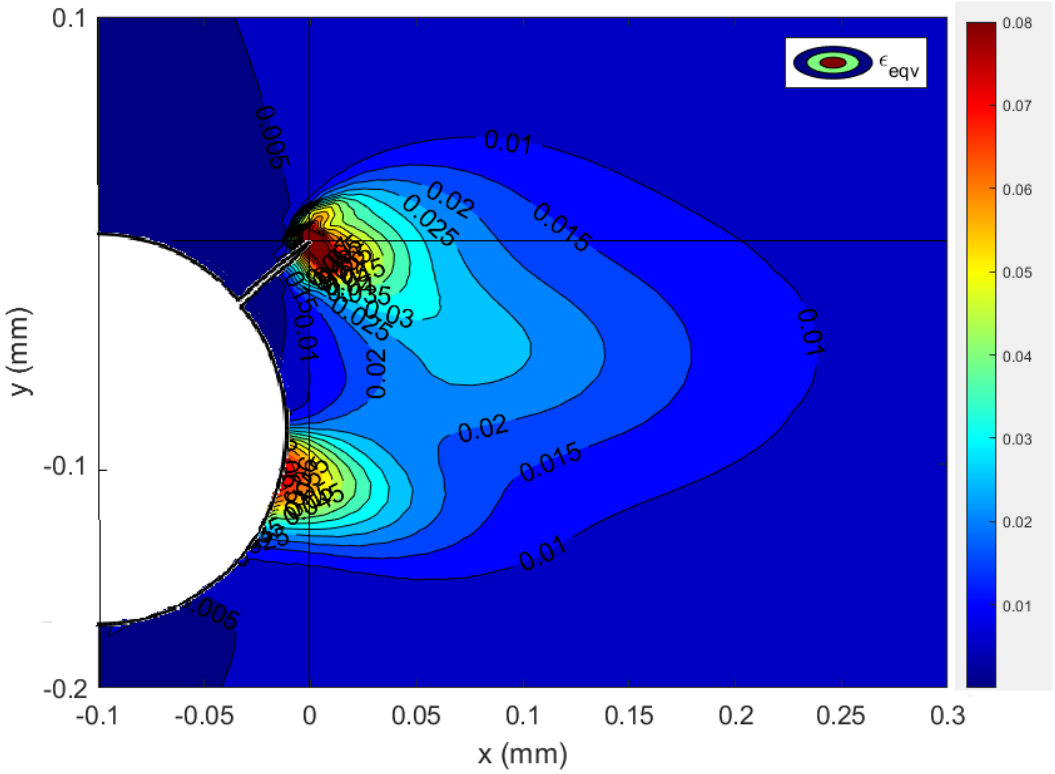

Figure 3.25. Equivalent strain contours around the pre-crack and the notch. Anisotropic superelastic material model.

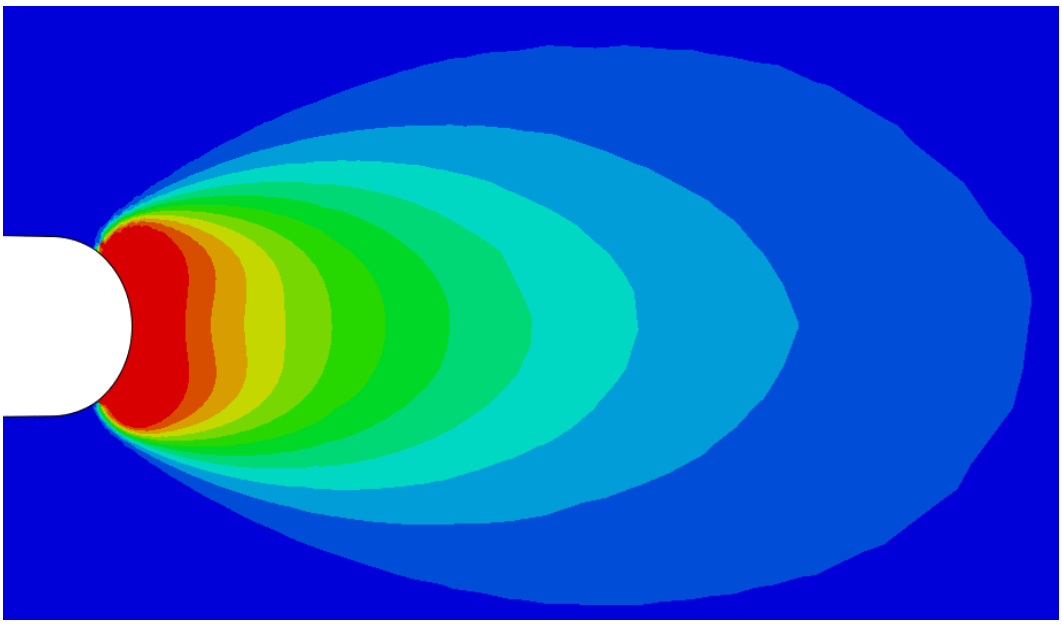

Figure 3.26. Martensite transformation contours (MVF) around the notch. Anisotropic superelastic material model.

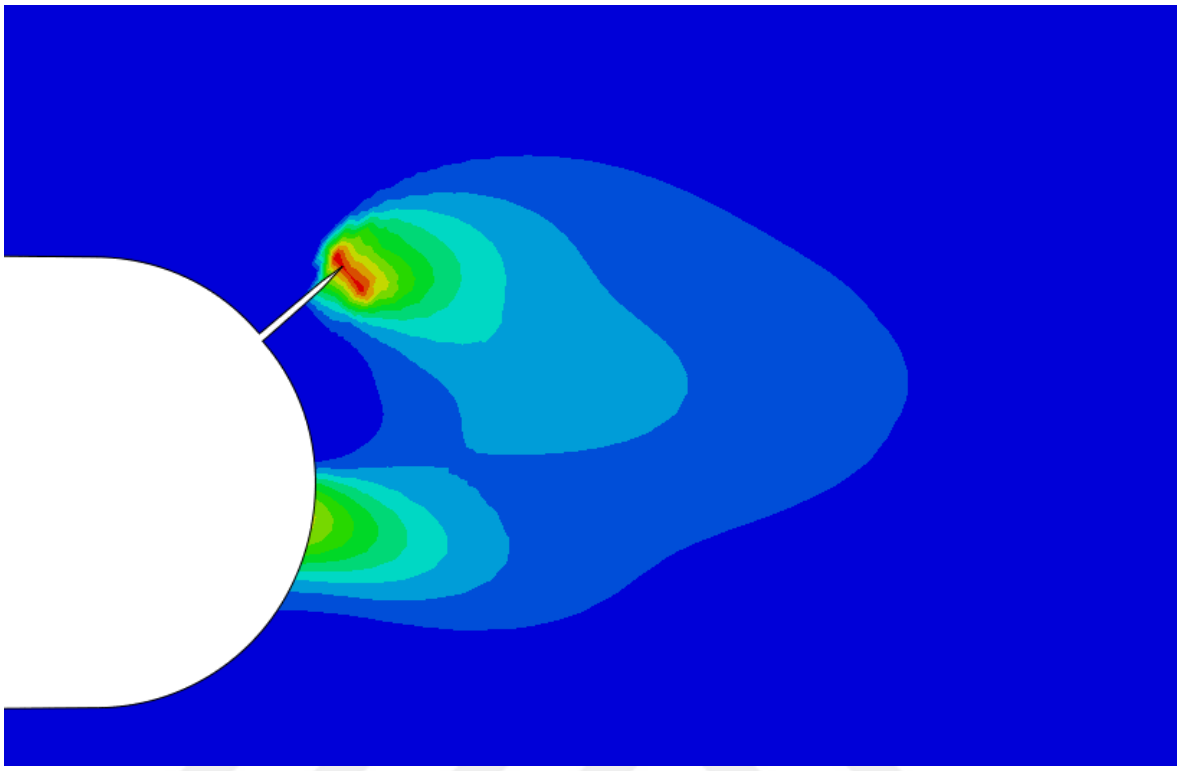

Figure 3.27. Martensite transformation contours (MVF) contours around the pre-crack and the notch. Anisotropic superelastic material model.

3.4.4.5. Calculation of Energy Release Rate as a Function of Crack Initiation Angle. A series of analyses are then performed to calculate the potential energy which consists of the strain energy, the transformation energy, and the external work [87]. The potential energy release rate, the change of potential energy with respect to the change in the crack surface area $\frac{\Delta \Pi}{\Delta A}$ is calculated using small cracks around the notch (shown as an inset in Figure 3.28), and using a node release technique. A fourth-order polynomial is fitted to the $\frac{\Delta \Pi}{\Delta A}$ data to plot the potential energy release rate distribution around the notch.

Figure 3.28 shows the energy release rate as a function of θ . The curve is plotted focusing on the area where the maxima occurred. The maximum of the energy release rate is found at $\theta_c \approxeq 41.2°$.

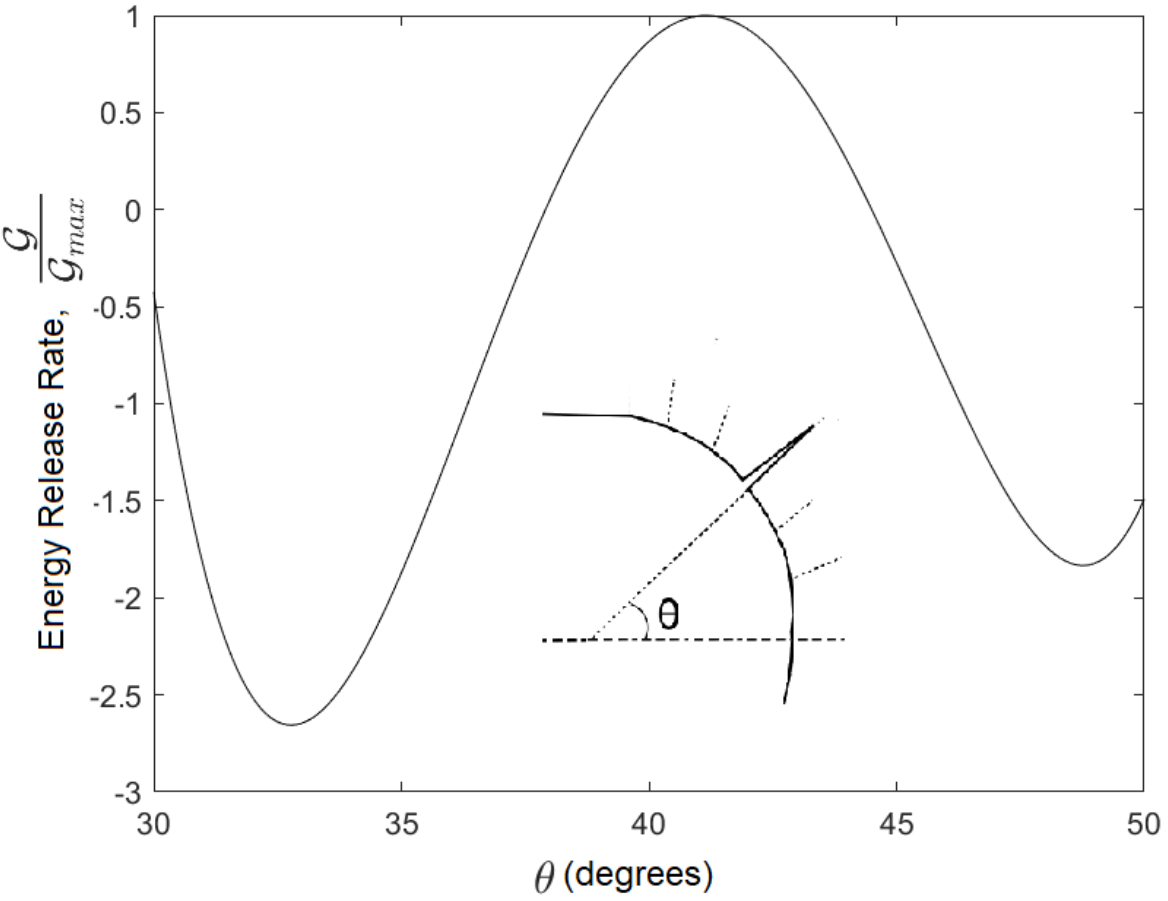

Figure 3.28. Distribution of energy release rate around the crack tip for anisotropic superelastic material obtained from finite elements analyses. Maximum of $\mathcal{G}$ is found at angle $\theta_c \cong 41.2°$.

The crack initiation angles obtained from finite element analyzes were found to be in good agreement to the analytical calculation results. However, with finite elements, in addition to the tangential stress, energy release rate, and strain energy densities, martensitic transformation areas can also be calculated. Although the tangential stresses were found to be of the same order, it was seen that the strain energy density and energy release rate values were considerably higher than the analytical calculation results due to included effect of martensitic transformation. This result supports that the martensitic transformation improves the fracture behavior of CoNiAl shape memory alloys.

3.5. Summary and Conclusions

Tree notched single crystal CoNiAl specimens are tested under similar conditions, and crack initiation angles with a magnitude of 43 $\pm 1^{\circ}$ are obtained. The martensite localization band that forms in the tension specimen has approximately the same angle with the crack initiation angle in the notched specimen as shown in Figure 3.29.

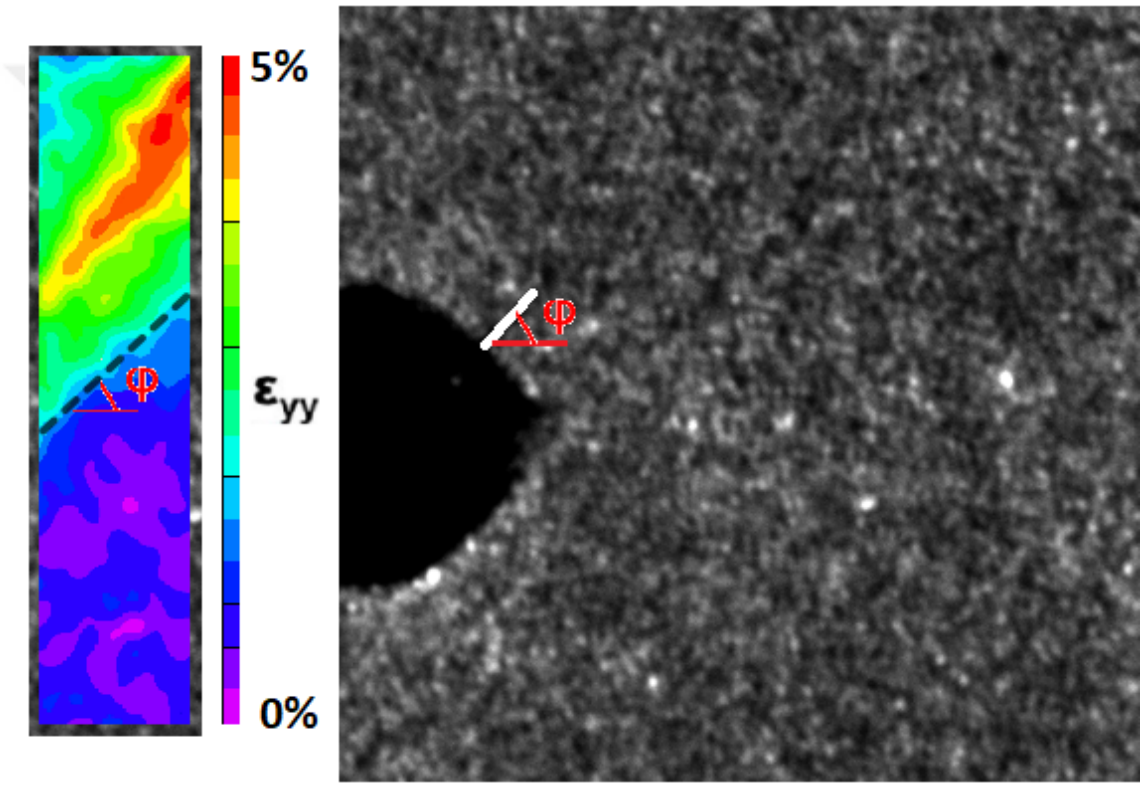

Figure 3.29. Martensite band angle in the tension specimen and a crack emanating from the notch, which have approximately the same angle, ϕ.

The tangential stresses and strain energy densities are then calculated analytically around the notch and using Generalized Maximum Tangential Stress (GMTS), Maximum Energy Release Rate (MERR), and the Strain Energy Density (SED) Criteria, and crack initiation angles are determined. The comparison of critical crack initiation/growth angle measurements, analytical calculations and finite element results are summarized in Table 3.3.

Table 3.3. Comparison of critical crack initiation/growth angles from experiments and finite element analyses ($\approxeq \theta_c^\circ$).

Experiments		**Analytical**		**FEM MTS**		**FEM MERR**	
1st specimen	43°	GMTS	42.3°	Anisotropic (notch)	41.3°	Anisotropic (crack)	41.2°
2nd specimen	44°	MERR	41.6°	Isotropic (notch)	0°	**FEM SED**	
3rd specimen	−42°(44°)	MSED	40.9°	Anisotropic (crack)	41°	Anisotropic (notch)	38°

Comparisons show that, as a first attempt, the criteria that are originally developed for linear elastic anisotropic materials give reasonable results. The anisotropic transformation behavior of a single crystal shape memory alloy has a significant effect on crack initiation/propagation directions. The direction of the martensitic transformation band is dependent on the SMA material composition that also affects the cracking angle.

For simplicity only one variant of martensite that dominates has been used in the calculations here. For other single crystal SMAs, it might be necessary to determine all the martensite variants and to calculate the tangential stress, the energy release rate, and the strain energy density corresponding to each martensite variant.

4. CRACK GROWTH IN SINGLE CRYSTAL SHAPE MEMORY ALLOYS

4.1. Introduction

In this chapter the crack growth in a single crystal shape memory alloy is studied with specific emphasis on the effect of a secondary phase. There are studies on propagating crack–γ phase interaction in NiMnCoGa, NiMnSnFe, and NiMnGaFe shape memory alloys [110–112] that report an improvement in ductility and fracture toughness. Ma *et al.* [110] and Wu *et al.* [111] discuss the increase in fracture toughness, but do not calculate any corresponding fracture parameters. Euh *et al.* [112], in addition, calculate the stress intensity factors but only when the crack tip is located inside the γ-phase under quasi-static loading; they do not evaluate the crack growth under cyclic loading and do not look into details of crack growth.

CoNiAl single crystal shape memory alloy specimens are used in the study. CoNiAl is brittle in nature and prone to brittle cracking like the materials used in the examples cited above. This behavior is reduced through heat treatment which also modifies the transformation temperatures A_s, M_s, A_f, and M_f and the shape memory and superelastic behavior [6–10]. The heat treatment results in a secondary phase (γ-phase), the volume fraction of which depends on the annealing temperature, its duration and the rate of cooling. The presence of γ-phase increases transformation strains [3, 6–9, 18, 20, 21] and affects the tensile strength, ductility, superelastic properties and shape memory strain recovery capabilities of the alloy [6, 22, 113, 114]. The secondary phase does not undergo forward martensitic transformation [4] and also modifies the fracture behavior of CoNiAl.

In the literature there is a lack of studies on mechanical (structural) fatigue fracture mechanics of CoNiAl shape memory alloys while there are a number of works on functional fatigue [3, 115–117]. Previous studies on this alloy are limited to the investigation of its superelastic & isobaric shape memory behavior through tension

and/or compression tests, phase transitions, two-way shape memory effect (TWSME), crystal structures, effect of annealing, precipitation behavior, quenching temperature and cooling rate on the structural & magnetic properties, production, and ductility enhancements, also the effects of different compositions of the constituents [3–5, 8–10, 13, 15, 16, 19, 21–23, 113, 115–157].

In this study, the crack growth under cyclic loading and the effect of the secondary phase that acts as a microstructural barrier in CoNiAl single crystal shape memory alloy are investigated for the first time. The material used has a shape-memory behavior at room temperature, and a superelastic behavior at $50^o\,C$ under tensile loading. Using edge notched specimens, cyclic loading tests are conducted in superelastic and shape memory regimes to determine the fatigue crack growth in specimens with two distinct crystalline phases: the austenitic phase that transforms to martensitic phase and the martensitic phase that undergoes re-orientation (Details on the experimental procedure and the material behavior are explained in detail in Chapter 3). Full field displacement data obtained with DIC are fitted to the analytical solution for anisotropic displacement field around crack tip and the fracture parameters are calculated at each step for a growing crack. Test specimens are examined post failure with optical microscopy to determine the transient crack growth behavior.

4.2. Digital Image Correlation

The stress intensity factors, ΔK_I and ΔK_{II} are extracted by fitting the measured horizontal and vertical displacement data obtained from DIC to the following crack tip displacement equations given by Sih *et al.* [100] for linear elastic anisotropic bodies. This methodology is described in detail in [158, 159].

$$\begin{aligned}\Delta u &= \Delta K_I\sqrt{\frac{2r}{\pi}}Re\left[\frac{1}{\mu_1-\mu_2}\left(\mu_1 p_2\sqrt{cos\theta+\mu_2 sin\theta}-\mu_2 p_1\sqrt{cos\theta+\mu_2 sin\theta}\right)\right]\\ &+ \Delta K_{II}\sqrt{\frac{2r}{\pi}}Re\left[\frac{1}{\mu_1-\mu_2}\left(p_2\sqrt{cos\theta+\mu_2 sin\theta}-p_1\sqrt{cos\theta+\mu_2 sin\theta}\right)\right]\\ &+ a_{11}Trcos\theta - A_1 rsin\theta + B_u, \end{aligned} \tag{4.1}$$

$$\begin{aligned}\Delta v &= \Delta K_I\sqrt{\frac{2r}{\pi}}Re\left[\frac{1}{\mu_1-\mu_2}\left(\mu_1 q_2\sqrt{cos\theta+\mu_2 sin\theta}-\mu_2 q_1\sqrt{cos\theta+\mu_2 sin\theta}\right)\right]\\ &+ \Delta K_{II}\sqrt{\frac{2r}{\pi}}Re\left[\frac{1}{\mu_1-\mu_2}\left(q_2\sqrt{cos\theta+\mu_2 sin\theta}-q_1\sqrt{cos\theta+\mu_2 sin\theta}\right)\right]\\ &+ a_{12}Trsin\theta+A_1 rcos\theta+B_v, \qquad (4.2)\end{aligned}$$

where

$$p_i = a_{11}\mu_i^2+a_{12}-a_{16}\mu_i, \qquad (4.3)$$

$$q_j = a_{12}\mu_j+\frac{a_{22}}{\mu_j}-a_{26}, \qquad (4.4)$$

and

$$a_{11}\mu^4-2a_{16}\mu^3+(2a_{12}+a_{66})\mu^2-2a_{26}\mu+a_{22}=0. \qquad (4.5)$$

In the Equations (4.1) and (4.2), Re represents the real part of a complex number, T is the T-stress [87]. The inclusion of the T-stress is necessary for better accuracy in the calculation of fracture parameters [82]. A_1 is the rigid body rotation, B_u and B_v are the rigid body translations in u and v directions, respectively. a_{11}, a_{12}, a_{16}, a_{22}, a_{26}, and a_{66} are the reduced compliance components for plane stress problems, and μ_1 and μ_2 are the roots of Equation (4.5). r and θ are the crack tip coordinates in polar coordinate system as shown in Figure 4.1.

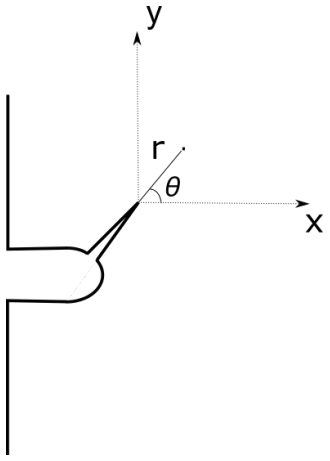

Figure 4.1. Crack tip configuration presented in polar coordinates.

The stress intensity factors, ΔK_I and ΔK_{II}, as well as the T-stress and rigid body motion terms are extracted from Equations (4.1) and (4.2). The effective stress intensity factor ΔK_{eff} for mixed mode is calculated as follows:

$$\Delta K_{eff} = \sqrt{K_I^2 + \alpha K_{II}^2}, \tag{4.6}$$

where

$$\alpha = \frac{\Delta J_2}{\Delta J_1}, \tag{4.7}$$

and

$$\Delta J_1 = -\frac{\pi \Delta K_I}{2} a_{22} Im \left[\frac{\Delta K_I(\mu_1 + \mu_2) + \Delta K_{II}}{\mu_1 \mu_2} \right], \tag{4.8}$$

$$\Delta J_2 = \frac{\pi \Delta K_{II}}{2} a_{11} Im \left[\Delta K_{II}(\mu_1 + \mu_2) + \Delta K_I \mu_1 \mu_2 \right]. \tag{4.9}$$

and μ_k are the roots of the characteristic Equation (4.5). ΔJ_i in Equations (4.8) and (4.9) are the energy release rates that are used to calculate the effective stress intensity factor, ΔK_{eff}, for mixed mode [100].

The references mentioned earlier [158, 159], use a_{ij}'s that belong to the bulk parent material. The referenced works all use homogeneous materials, where there are no different local phases with different properties and no localization. In CoNiAl, as discussed in detail earlier, there is a region of transformation around the crack tip. The a_{ij}'s are therefore "effective" properties that consist of the properties of the transforming and the non-transforming (γ) phases. Using the a_{ij} which belongs to the individual phase only, would not give the proper behavior, because in stress intensity factor calculations the data used in least squares fitting come from the area around the crack tip. Calculating effective a_{ij} using least squares fitting to DIC is more reliable, since the properties found are calculated from the region around the crack tip.

In the calculations the compliance matrix components, $a_{11}, a_{16}, a_{12}, a_{66}, a_{26}$ and a_{22} (a_{ij}) that are not known are determined together with the fracture parameters using the least squares curve fitting of the DIC data to Equations (4.1) and (4.2). Equations (4.3), (4.4) and (4.5) are used as constraints.

4.3. Results and Discussion of Crack Growth

For the crack growth experiments, five edge-notched dog-bone specimens with edge-notches cut at the mid-sections are used. Three superelastic and two shape memory cyclic loading tests are conducted, and similar cracking behaviors are observed in superelastic and shape-memory regimes with the only differences being on γ-phase locations. As a result, two different test results of superelastic specimens, and one test result of shape memory specimen are reported in the present work.

4.3.1. Superelastic Case 1

After initiation, the crack grows in the "1" direction with increasing stress intensity factor (see Figure 4.2).

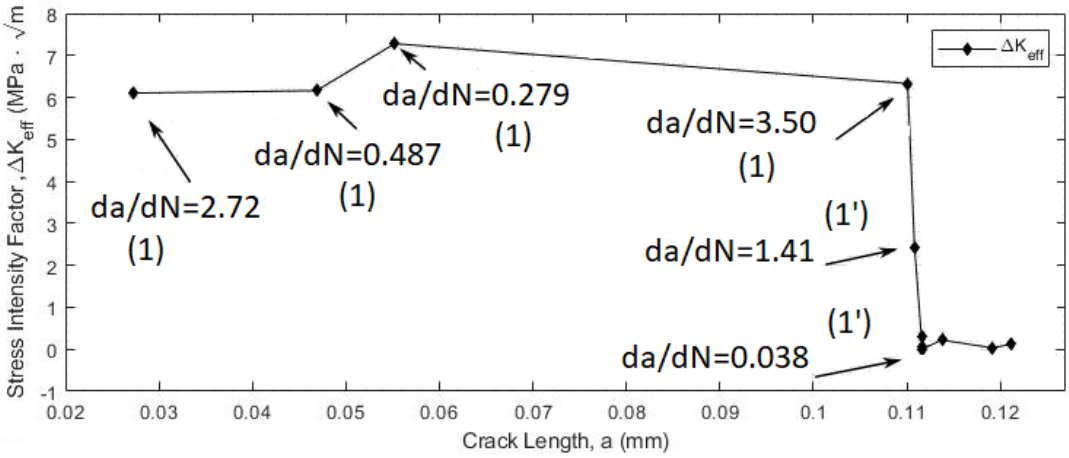

Figure 4.2. Effective stress intensity factor vs. crack length after crack initiation (SE1). Corresponding crack growth rates (da/dN) are given in 10^{-8} m/cycle. Numbers in parentheses correspond to the effective crack in the crack growth sequence in Figure 4.3.

During propagation, the crack growth rate drops to $0.487\text{x}10^{-8} m/cycle$ then to $0.279\text{x}10^{-8} m/cycle$, which occurs upon hitting a small $\gamma-$phase region. The propagation slows down, the crack passes through the $\gamma-$phase region without kinking (Figure 4.3 & 4.4). Then, when a crack length of 0.11 mm is reached, a sharp drop in the stress intensity factor is found, and the main crack is observed to kink from direction "1" to "1′" as shown in Figure 4.3 & 4.4. Then, the crack advanced slowly to "1″" with decreasing da/dN and comparatively lower stress intensity factors (Figure 4.2).

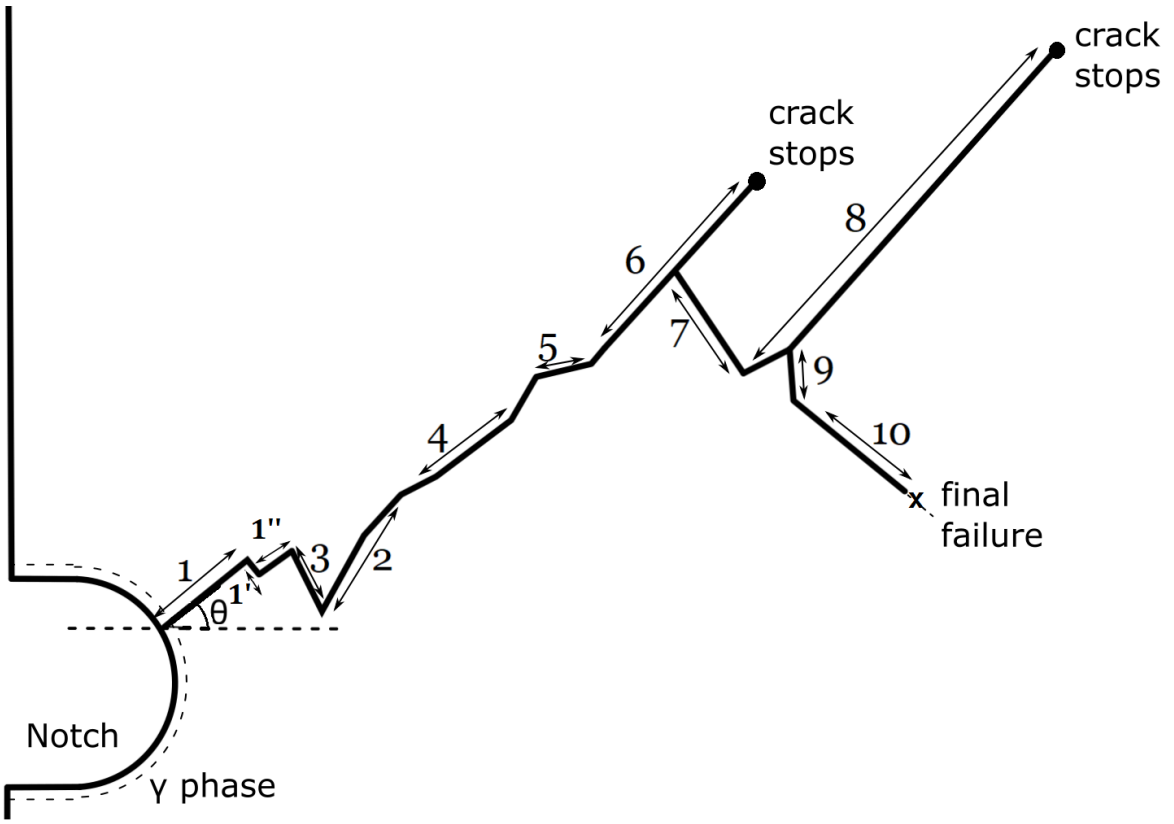

Figure 4.3. Sketch of crack growth path from the notch (SE1). Numbers indicate sequences of crack growth. The γ-phase region around the notch is shown by the dashed line. The specimen fails at $\approx$ 36000 cycles.

In Figure 4.4 (a, b and c), the snapshots from the DIC camera show the growth of the crack. The first image in Figure 4.4 (a), is taken when the crack is 0.1479 mm long. Subsequent images are taken with intervals of 1000 cycles. When studied with Figure 4.2, it is observed that when the crack changes direction (Figure 4.4 (a), "1" to

“1′”), the stress intensity factor decreases. Later the crack continues to grow parallel to the initial crack following direction “1″” with an increasing stress intensity factor (Figure 4.5). The first datum point in Figure 4.5 corresponds to the last one in Figure 4.2.

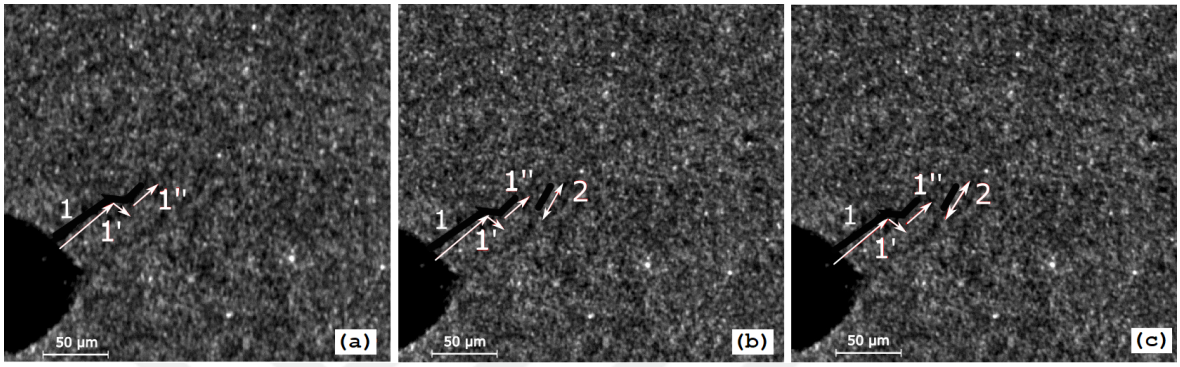

Figure 4.4. Crack initiation and following advancement in the first superelastic specimen (SE1). (a) DIC image showing kinking in the crack growth direction (“1” → “1′” → “1″”). (b) New crack forms (“2”). (c)“1″” and “2” advance.

Stress intensity factor for Figure 4.4 (a) is calculated as 17.4 $MPa\sqrt{m}$, after which the main crack length (“1”, “1′” and “1″” in Figure 4.4 (b)) increases to 0.1502 mm, but the effective stress intensity factor decreases. As shown in Figure4.4 (b), a new crack (“2”) is observed to form, which explains the decrease in the stress intensity factor of the main crack (shown with “1″” in Figure 4.5). During this period (“1″” to “3”), the main crack continues growing. Still, the crack growth rate (da/dN) decreases, which is a result of the simultaneous growth of the two cracks: The new crack “2” and the main crack from “1″”. In Figure 4.4 (c), the newly formed crack “2” slightly increases in size, extending from both ends: Upwards direction and downwards to the main crack “1″”. Eventually, it merges with the main crack at the “3” region as shown in Figure 4.3. The stress intensity factor calculated for this case, where cracks ”1″” and “2” both continue growing independently, is calculated to be 1.5 $MPa\sqrt{m}$, and the main crack length increases to 0.1519 mm (Figure 4.5).

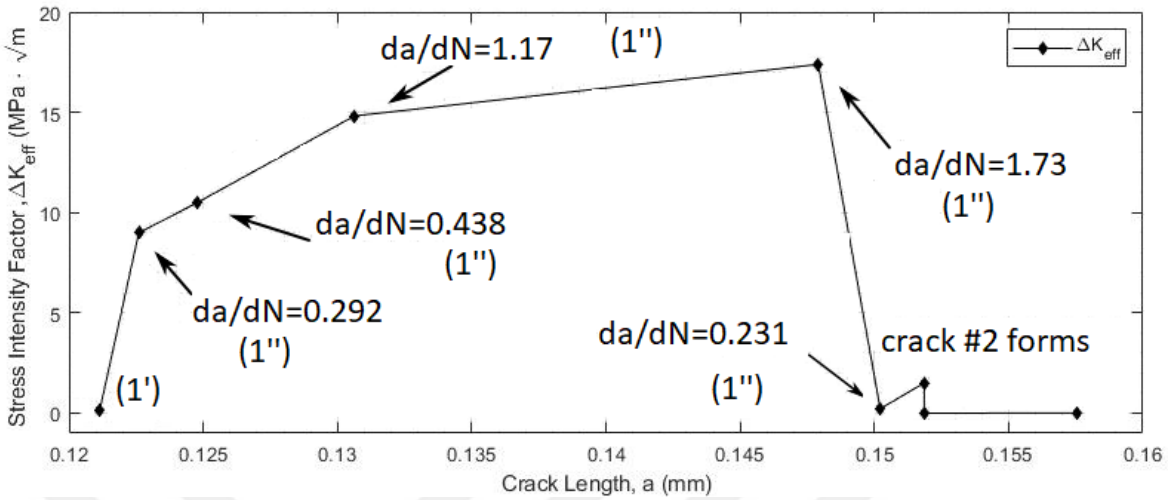

Figure 4.5. Effective stress intensity factor vs. crack length (SE1). Corresponding crack growth rates (da/dN) are given in 10^{-8} m/cycle. Numbers in parentheses correspond to the effective crack in the crack growth sequence in Figure 4.3.

For further analysis of this complicated and interesting crack behavior, the DIC paint on the surface of the specimen is cleaned and the specimen is examined under optical microscope after failure. Figure 4.6 shows the optical image of the ruptured specimen. It is observed that the stress intensity factor starts to decrease when the crack tip ("1") hits the boundary of the γ-phase.

The initial crack is shown with an arrow numbered "1" in Figure 4.4 which kinks and continues to grow parallel to the γ-phase boundary ("1′"). Following another kink, it advances into the γ-phase and becomes "1″". From "1′" to "1″" the stress intensity factor increases as shown in Figure 4.5. The arrow "2" in Figure 4.6 corresponds to the new crack formation in Figure 4.4 (b). It first propagates upwards, then starts growing backwards towards the main crack ("1″") after hitting the γ-phase region as shown in Figure 4.6. Following further loading, the main crack "1″" and the new crack "2" merge at "3" which happens to coincide with the boundary of the γ-phase. Effective stress intensity factors calculated during "1″" to "3" are very low, which increase after merging.

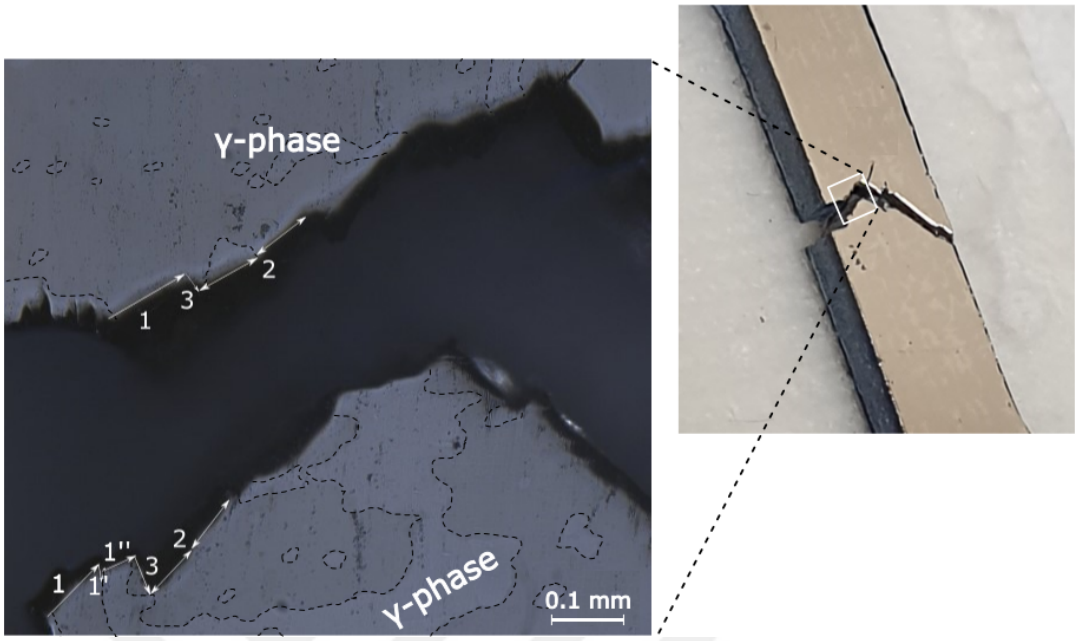

Figure 4.6. Optical microscopy image of the specimen SE1 taken after failure showing the cracks "1″" and "2" merging at "3". γ-phase borders are shown with black dashed lines. Inset shows the ruptured specimen and the area to which the microscopic image corresponds.

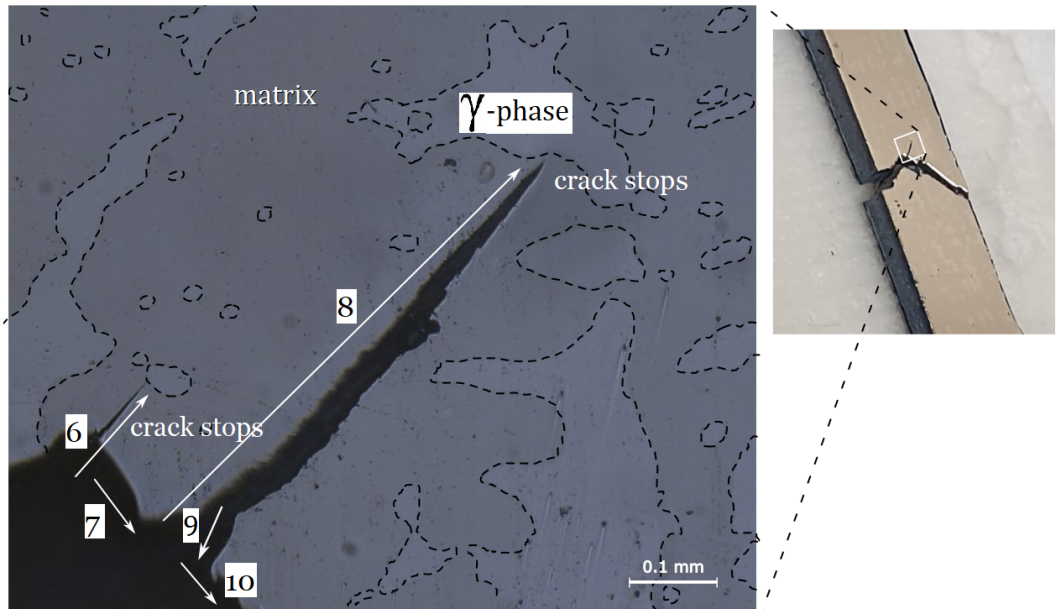

Figure 4.7. Cracks stop at γ-phase boundaries. Inset shows the ruptured specimen and the area to which the microscopic image corresponds (SE1). Numbers correspond to the effective crack in the crack growth sequence given in Figure 4.3.

In summary, what we see is, cracks stop, their directions deviate by the presence of γ-phase. In Figure 4.7, two of the stopping cracks at the γ-phase boundaries can be seen. Initially the main crack advances through direction "6" which stops upon hitting the γ-phase boundary. It then continues to grow in direction "7". "8" which also stops, later advances in direction "10". Additionally, microscopic inspections of the notch show that the notch edge itself is fully covered with the γ-phase that does not have a uniform thickness as shown in Figure 4.8. The crack initiates inside the γ-phase (arrow "i"), and only after tearing through the γ-phase that it advances into the martensitic phase (arrow "1").

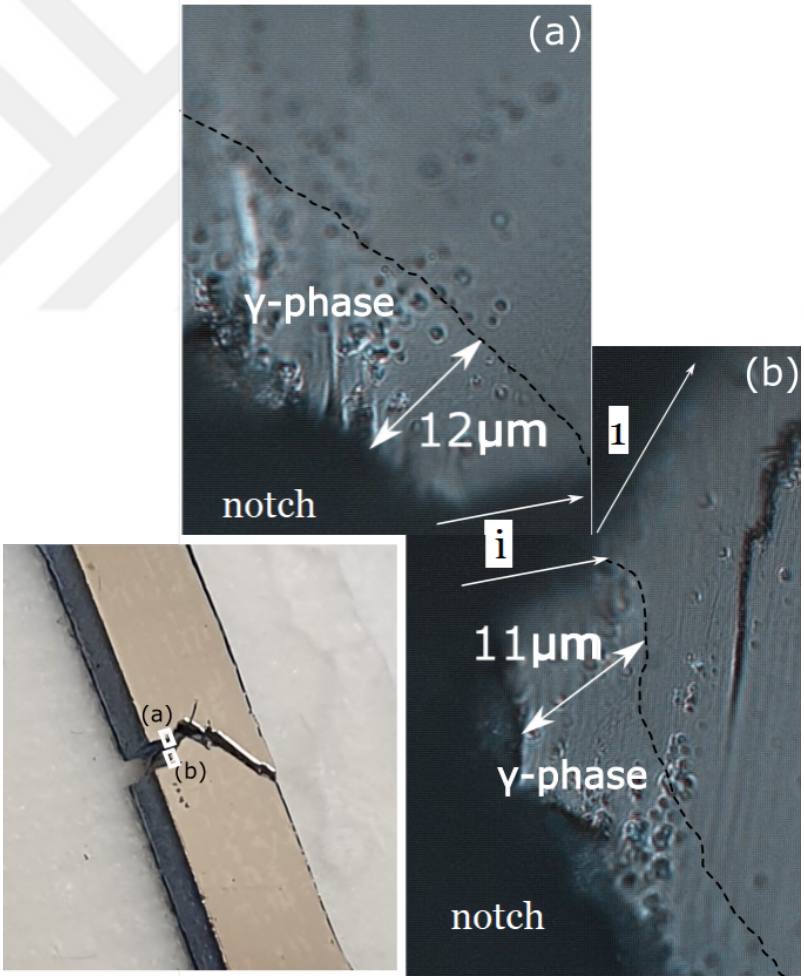

Figure 4.8. Microscopic images around the ruptured notch showing γ-phase (SE1). (a) The top with γ-phase thickness of $\approx 12\mu m$, (b) the bottom with $\approx 11\mu m$ thickness."i" indicates crack initiation inside γ-phase, and "1" corresponds to the first crack in Figure 4.3.

4.3.2. Superelastic Case 2

After initiation, the main crack is observed to advance faster than the growth observed in the first superelastic case until it stops at a length of 0.2012 mm after following a relatively straight path as presented with a sketch in Figure 4.9.

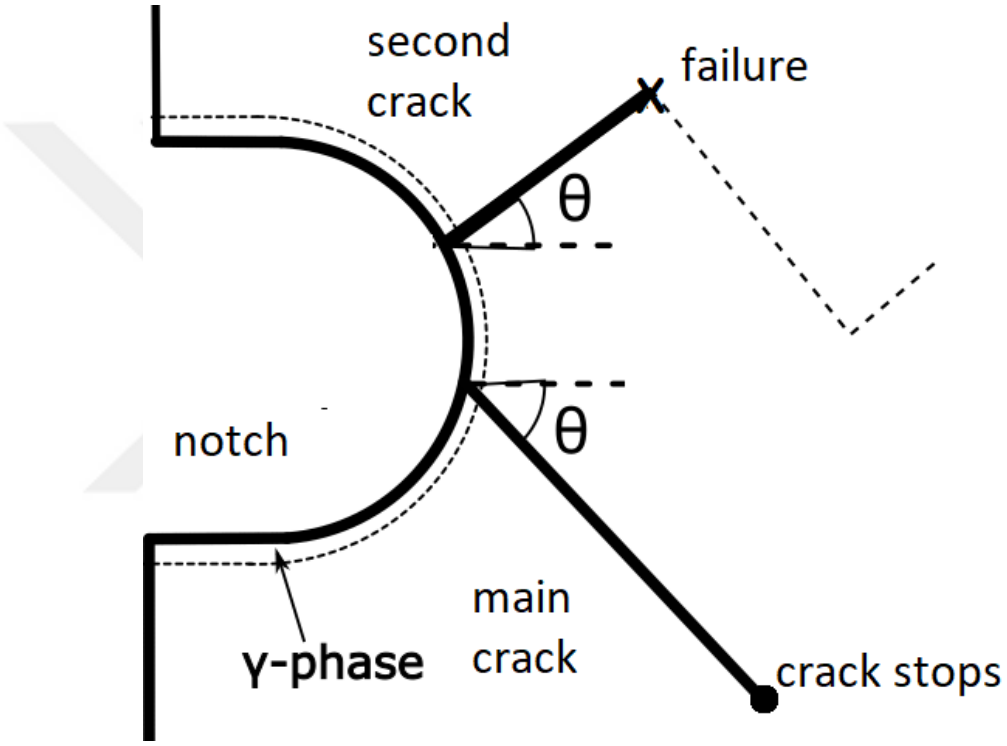

Figure 4.9. Sketch of the crack advancement (SE2): Cracks initiate and advance from the notch as shown. Dotted line around the notch shows the γ-phase region. The specimen fails from the "second crack" when the crack length is 0.095 mm, and 1664 cycles after crack the initiation.

Effective stress intensity factors increase to 10.8 $MPa\sqrt{m}$ during the advancement of the main crack. The effective stress intensity factors vs. crack length is plotted in Figure 4.10.

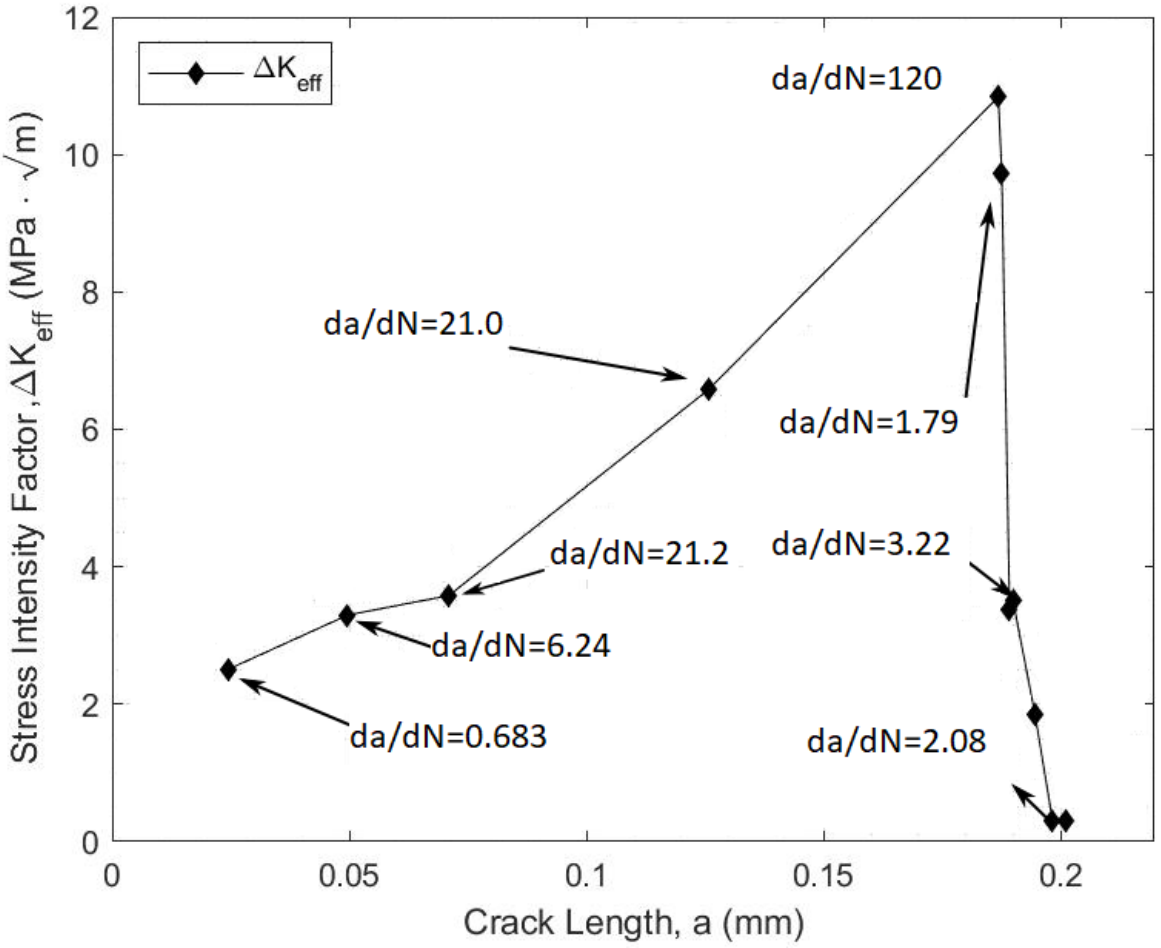

Figure 4.10. Effective stress intensity factor vs. crack length (SE2). Corresponding crack growth rates (da/dN) are given in 10^{-8} m/cycle. Results are for the main crack obtained from the area (AOI) that is shown in Figure 4.11.

When the DIC images are examined post failure, another crack is detected at the notch at $\approx 44°$ angle (see the inset in Figure 4.11) at the time when the main crack growth started to slow down. This new crack grows faster than the main crack and the specimen finally fails from it, the advancement of this crack is sketched in Figure 4.9 as "second crack" together with the main crack. In Figure 4.11, the main crack, the second crack, and the area of interest (AOI), from which the data are collected during testing are shown. An image of the region after failure is added to show how the failure occurs from the second crack. The time increment between these images is 0.2 seconds.

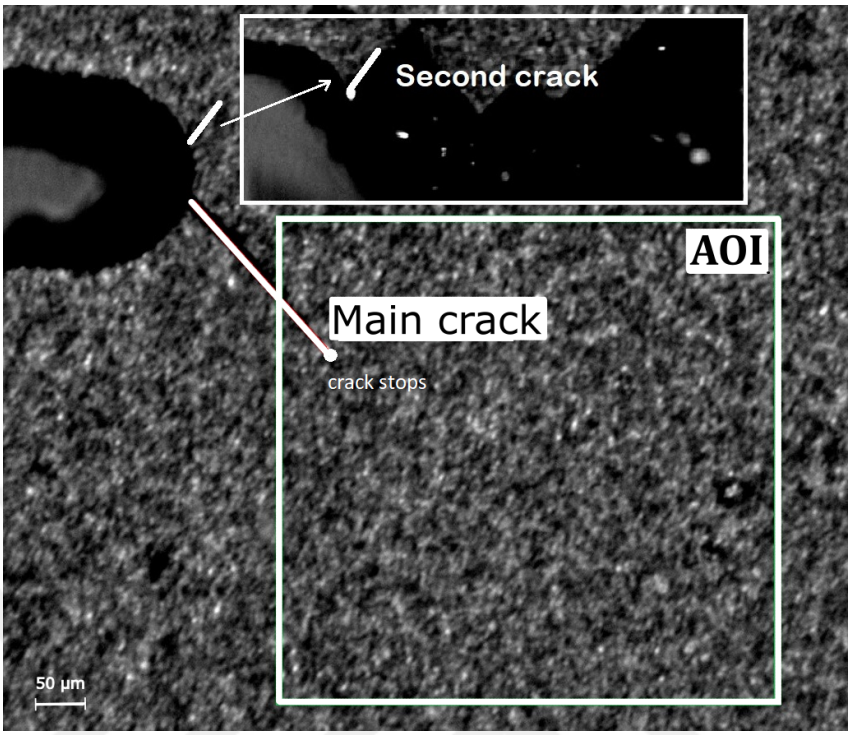

Figure 4.11. DIC image just before failure (SE2). Inset shows the DIC image of the second crack after failure.

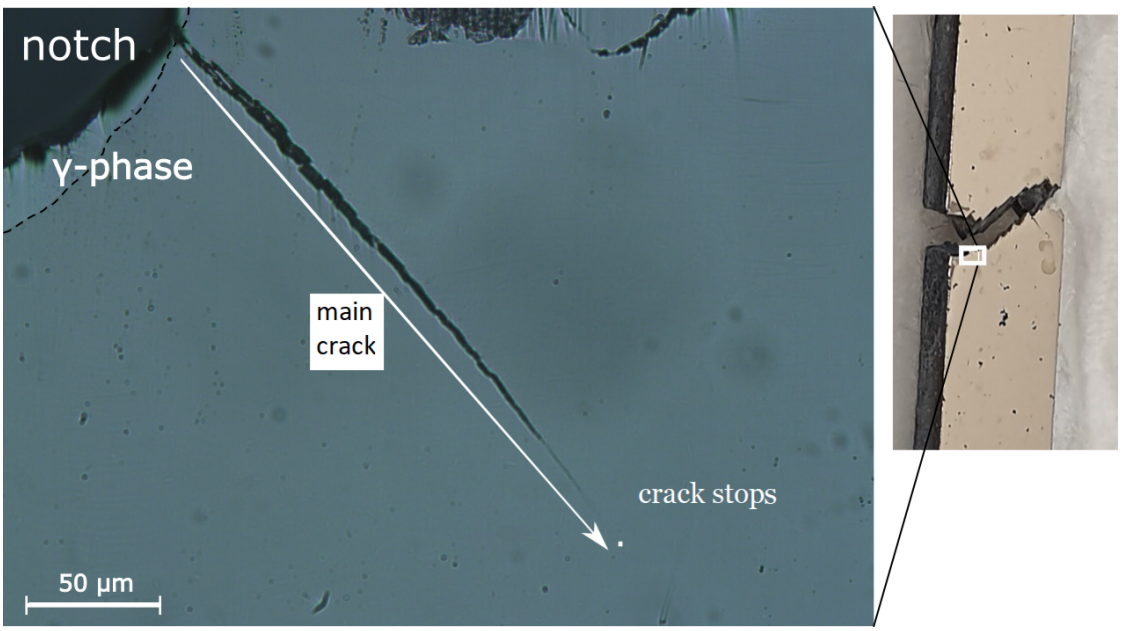

Figure 4.12. Optical microscopy of the main crack (SE2). γ-phase borders at the notch are shown with black dashed lines. Inset shows the ruptured specimen, and the area to which the microscopic image corresponds.

To determine the effect of microstructural barrier on crack growth, the DIC paint is cleaned from the surface of the specimen, and the ruptured piece is examined under optical microscope. No γ-phase is observed around the crack tip as shown in Figure 4.12 when the crack stops.

The formation of a new crack ("second crack") results in a decrease in the SIF calculated for the main crack, and the da/dN decreases from 120 to $1.79 \cdot 10^{-8}$ m/cycle (see Figure 4.10). Later, the da/dN of the "main crack" increases from 1.79 to $3.22 \cdot 10^{-8}$ m/cycle, which is found to be a result of a γ-phase encounter of the "second crack" that stops momentarily. During this period, the "main crack" continues to grow for 14.4 μm, then stops when the "second crack" kinks and continues growing.

When the growth stops, the equivalent strain $\left(\epsilon_{eq} = \sqrt{\frac{2}{3}(\epsilon_{xx}^2 + \epsilon_{yy}^2 + 2\epsilon_{xy}^2)}\right)$ calculated from the DIC strain data is examined. Figure 4.13 (a) shows that strains higher than 1% spread over a large area, indicating a martensitic transformation. After the crack stops, the region around the crack tip continues to transform. Figure 4.13 (b) shows the equivalent strain contours after $\approx$ 300 loading cycles following the arrest of the crack and the area inside 1% strain contour is considerably larger than the one shown in Figure 4.13 (a).

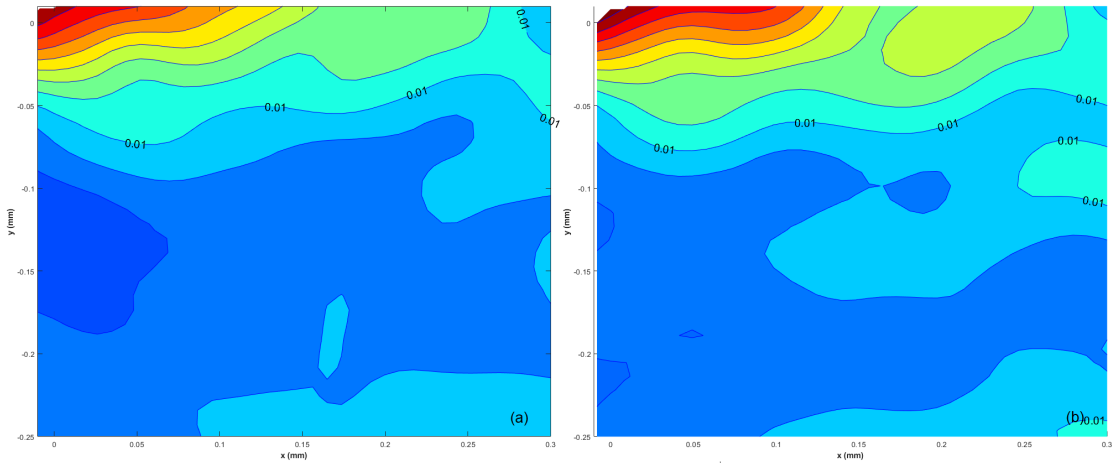

Figure 4.13. Equivalent strain (ϵ_{eq}) plots around the main crack tip after the crack stops (SE2). (a) Just after crack stops, (b) $\approx$ 300 cycles after crack stops. Results are obtained from the AOI in Figure 4.11.

Next, the region around the notch is inspected in the ruptured specimen. In Figure 4.14 the images from the optical microscope of the two cracks formed at the notch are presented (also see Figure 4.9).

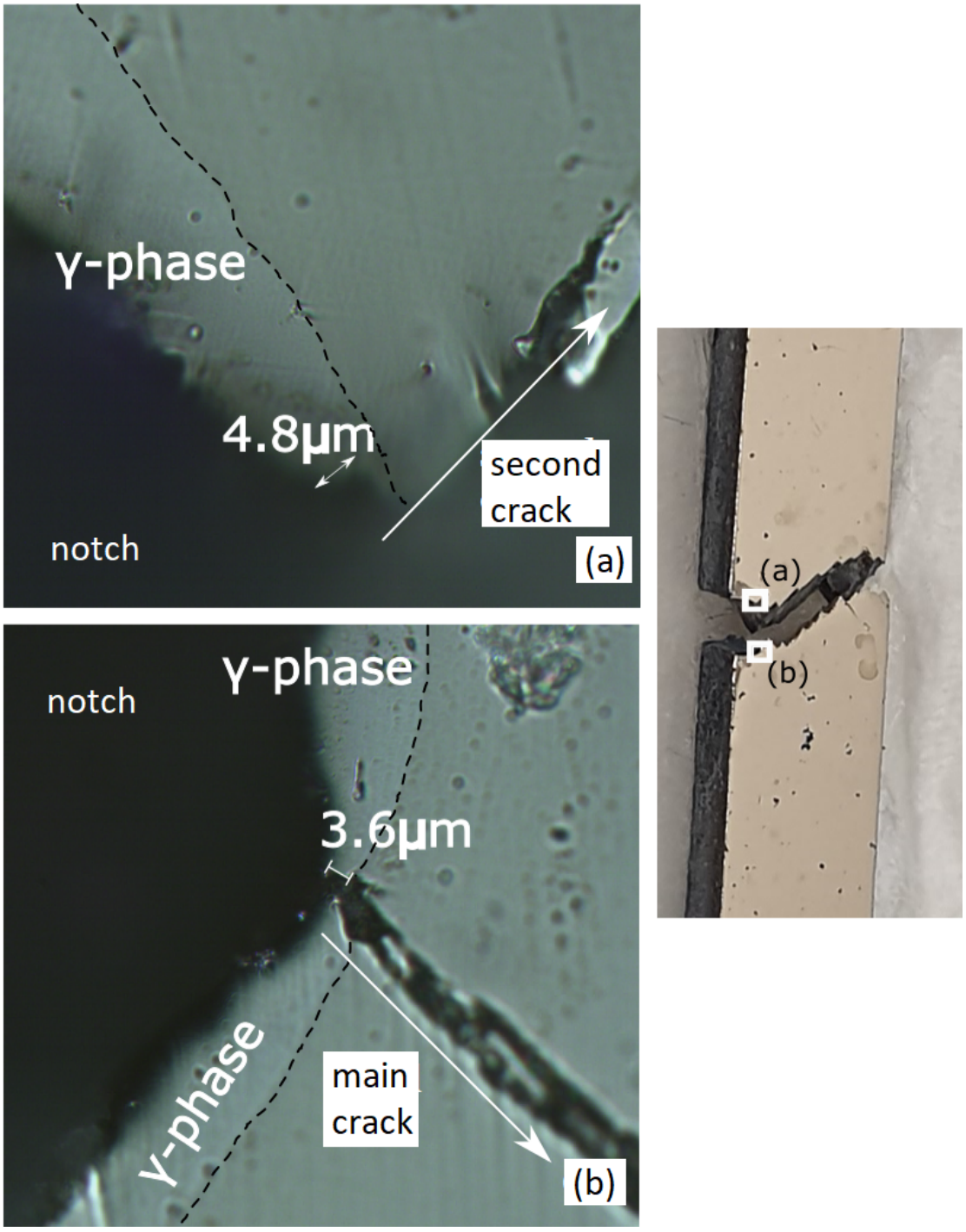

Figure 4.14. Crack initiation at the notch (SE2). (a) Second crack, (b) main crack. Inset shows the areas which correspond to the microscopic images are taken.

The initiation point of the main crack at the notch is given in Figure 4.14 (b), and Figure 4.14 (a) shows the second crack. The size of the γ-phase in Figure 4.14 (a) is larger around the initiation point of the second crack than the one shown in Figure 4.14 (b). The DIC images show that the "second crack" initiates first at the notch. But owing to the smaller area of γ-phase at the crack tip, the main crack forms in the martensitic phase and grows faster. Meanwhile, the second crack continues to grow at a much slower rate inside the γ-phase. When the second crack crosses the γ-phase boundary into martensitic region, the main crack slows down and eventually stops.

Table 4.1. Compliance components calculated using Equations (4.1)-(4.5). DIC data are obtained from the area (AOI) in Figure 4.11.

Cycle Number	**Crack Length (mm)**	S_{11} (MPa^{-1})	S_{12} (MPa^{-1})	S_{22} (MPa^{-1})	S_{16} (MPa^{-1})	S_{26} (MPa^{-1})	S_{66} (MPa^{-1})
1	0.0246	7.65E-05	-7.2E-05	12.4E-05	-1.1E-05	3.52E-05	4.93E-05
402	0.0496	5.74E-05	-4.2E-05	8.68E-05	6.85E-06	2.38E-05	5.31E-05
503	0.0710	4.96E-05	-4.3E-05	8.74E-05	-1.5E-06	2.6E-05	4.18E-05
805	0.1256	1.85E-05	-5.2E-06	4.12E-05	8.68E-06	1.07E-05	3.3E-05
856	0.1868	2.59E-06	-1.4E-06	9.59E-06	-5.3E-06	-9.2E-06	1.89E-05
897	0.1875	2.25E-06	-1.3E-06	4.03E-06	-1.3E-05	-4.5E-05	-1.04E-05
948	0.1892	2.44E-06	-1.2E-06	5.64E-06	-2.9E-05	-10.6E-05	-2.62E-05
1009	0.1899	2.5E-06	-1.5E-06	1.98E-06	-2.0E-05	-7.9E-05	-2.01E-05
1171	0.1946	2.21E-06	-1.4E-06	1.96E-05	-6.1E-05	-10.8E-05	18.5E-05
1272	0.1982	1.73E-06	-1.2E-06	-19.5E-05	-4.8E-05	-2.9E-05	-6.4E-05
1413	0.2012	2.43E-06	-1.8E-06	-11.8E-05	-2.3E-05	-2.2E-05	-1.99E-05
1564	0.2012	1.77E-06	-1.7E-06	3.65E-05	-32E-05	-2.2E-05	-120E-05

In Table 4.1, compliance components are given. Lines are drawn to separate the rows into three groups. The first group gives the results when the main crack advances with an increasing da/dN; the second group is for the slowing main crack, and the last group represents the results when it stops.

The results show that as the crack advances, absolute values of compliance components decrease, indicating an increase in stiffness and thus a decrease in fracture resistance. When the crack slows down and finally stops, S_{11} and S_{12} remain stable with other values fluctuating. Some of the a_{66} values in Table 4.1 are negative, indicating that the shear modulus is negative. A negative shear modulus is possible in the presence of martensitic phase transformation [160] and localization.

4.3.3. Shape Memory Case

Following the crack initiation, the effective crack grows from 0.0358 mm to 0.1065 mm (first a straight crack until "2" and then kinked to "3" as shown in Figure 4.15) with increasing da/dN and ΔK_{eff} for about 3500 loading cycles (Figure 4.16).

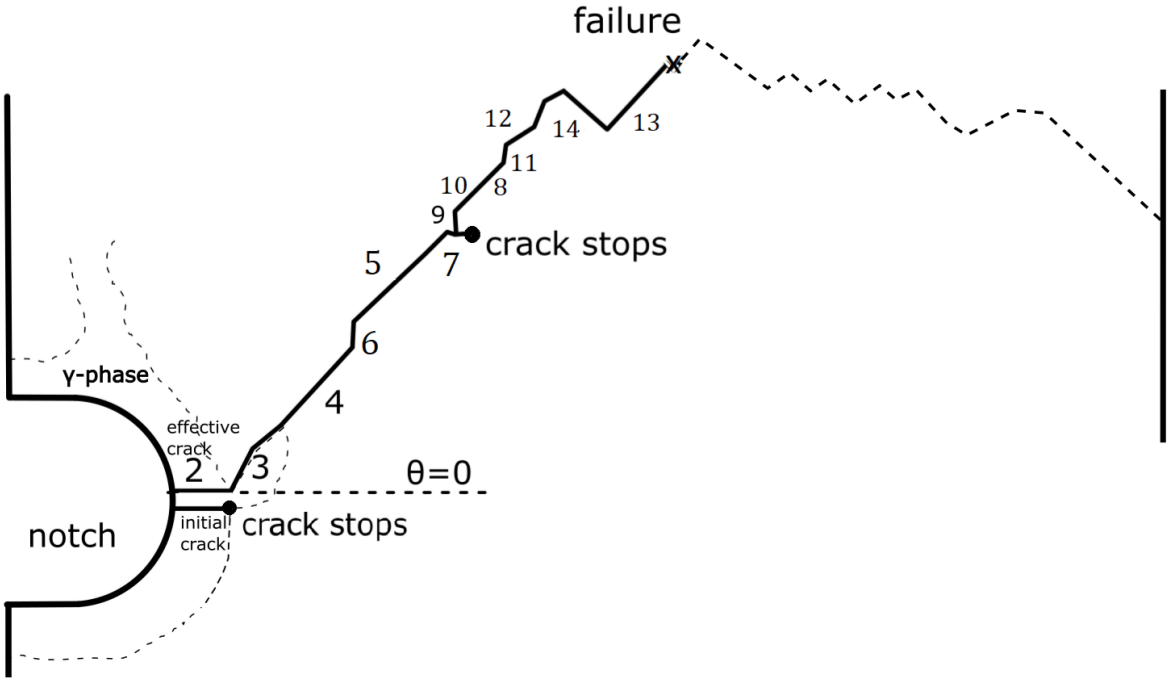

Figure 4.15. Sketch of the growth path of the effective crack (SM): Numbers indicate the sequences of crack advancement. Dotted line around the notch shows the γ-phase region. The specimen fails after $\approx$ 24000 cycles when the crack length increases to $\approx$ 0.8 mm.

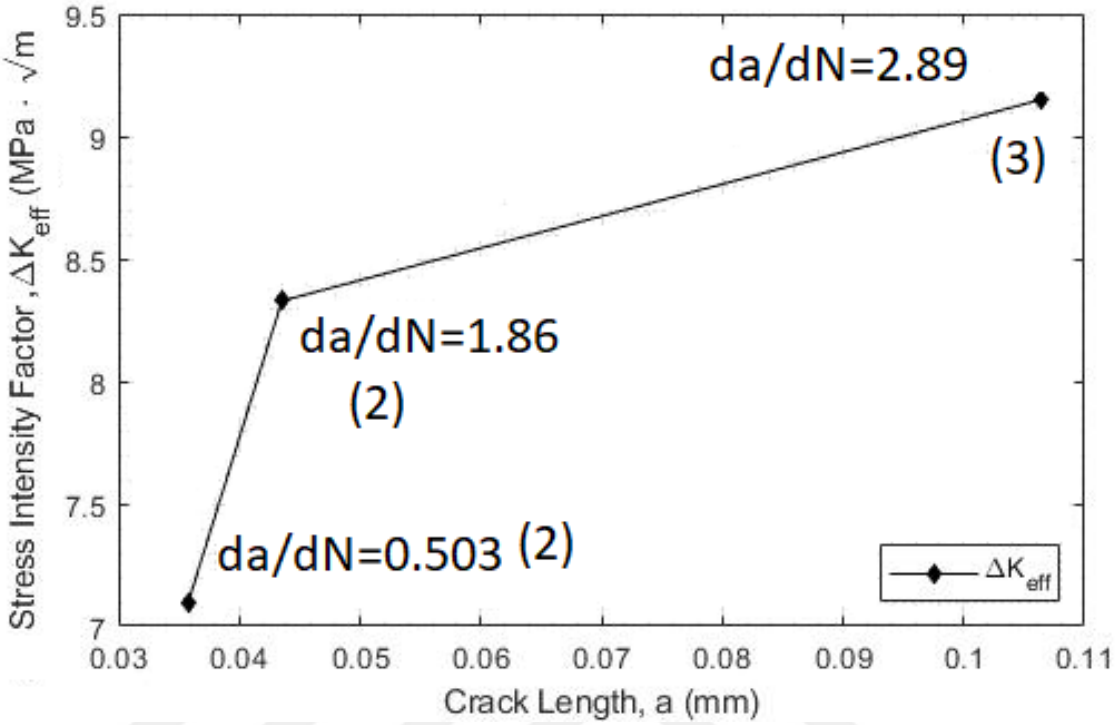

Figure 4.16. Effective stress intensity factor vs. crack length after crack initiation (SM). Corresponding crack growth rates (da/dN) are given in 10^{-8} m/cycle. Numbers in parentheses correspond to the crack growth sequences of the effective crack in Figure 4.15.

Optical microscopy images taken after failure show a large region of γ-phase around the notch (Figure 4.17) as a result of which both cracks initiate inside the γ-phase, and grow in Mode I at the early stages until they leave the γ-phase region.

As shown in Figure 4.17 (a) and (b) the crack deviates when its tip crosses the γ/martensite phase boundary, rather than continuing horizontally. Then the crack advances in mixed mode inside the martensitic phase, following the γ-martensite phase boundary.

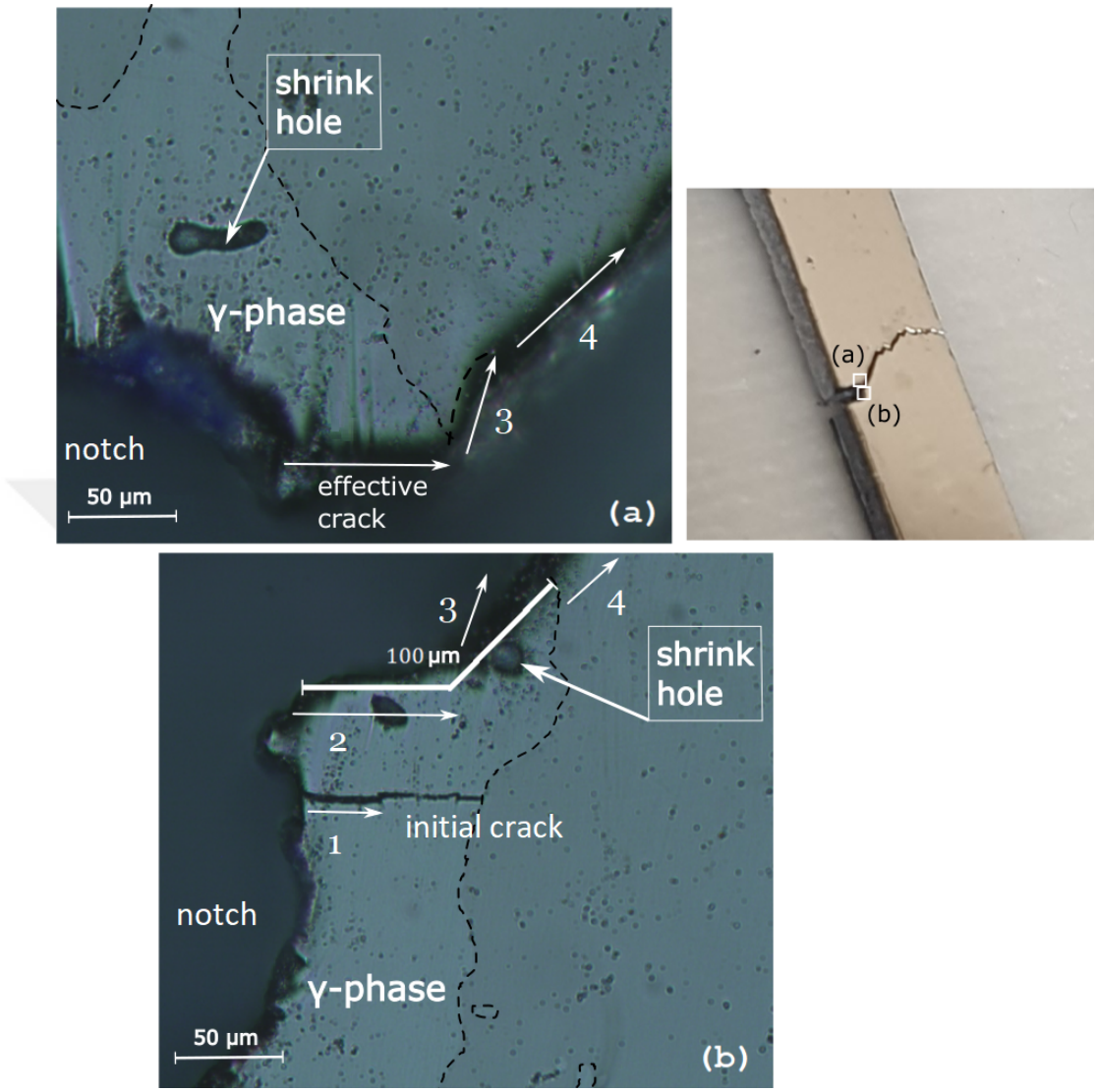

Figure 4.17. Optical microscopy images around the ruptured notch (a) the top, (b) the bottom (SM). Inset shows the ruptured specimen and the areas to which the microscopic images correspond.

New cracks that are not connected to the main crack are formed in several instances during testing as sketched in Figure 4.15 ("5", "8", "13"). In Figure 4.18 (a), one of the new cracks is shown on the DIC image. The new crack is marked "8" to show it's location (Figure 4.18 (b)). The length of the effective crack up to "7" in Figure 4.18 (a) is 0.5071 mm. Later, as seen in Figure 4.18 (b), the crack follows a path towards "9" and the effective crack and the new crack merge at "10".

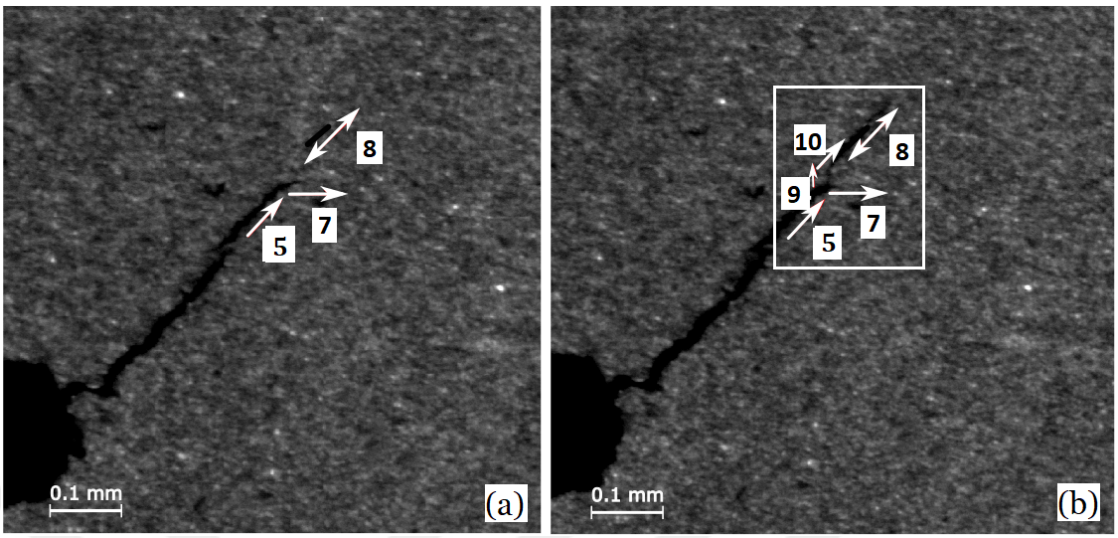

Figure 4.18. Crack growth in the shape memory specimen (SM). (a) DIC image showing a new crack formation ("8"). (b) The main crack and the new crack merge.

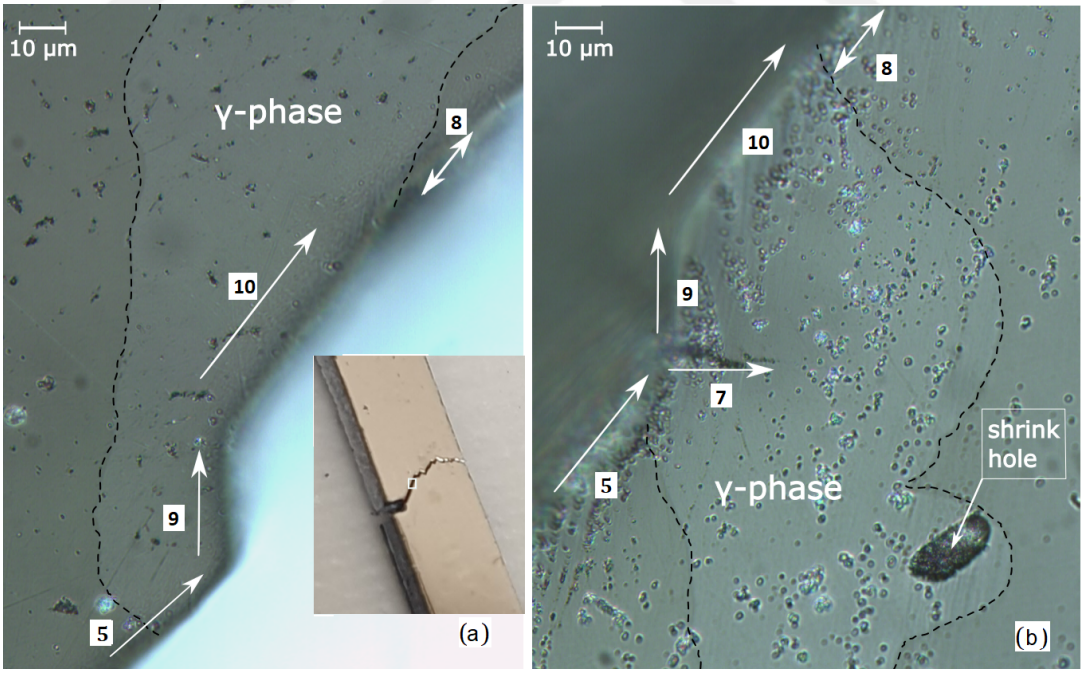

Figure 4.19. Crack growth in the shape memory specimen (SM). Optical microscopy image taken around the two cracks ("5" and "8") that merge at "9" and"10": (a) The top, (b) the bottom part of the ruptured specimen. γ-phase borders are shown with black dashed lines. Inset shows the ruptured specimen and the area to which the microscopic images corresponds.

In Figure 4.19 (a) and (b), optical microscopy shows the presence of the γ-phase where the crack growth slows down and stops. When the growing crack tip "5" hits the non-transforming γ-phase boundary, the crack stops and the effective stress intensity factor decreases. Afterwards the crack advances inside the γ-phase following direction "7" with a slower da/dN and increasing effective stress intensity factor (Figure 4.20). Then a new crack ("8") forms inside the martensitic region, and the effective stress intensity factor decreases. When the crack " 8" is closer to "5", the crack through "7" stops, the main crack changes path, follows "9" to "10" and merges with "8" resulting in an increase in the ΔK_{eff} and da/dN (See Figure 4.20).

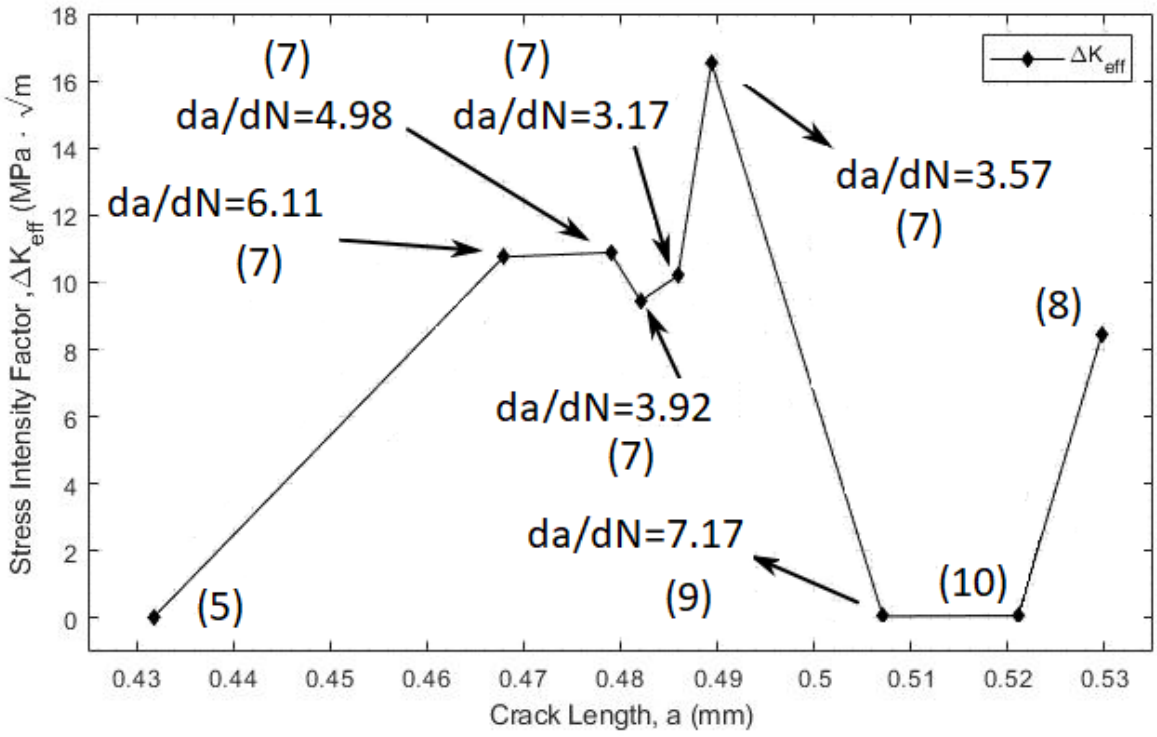

Figure 4.20. Effective stress intensity factor vs. crack length (SM). Corresponding crack growth rates (da/dN) are given in 10^{-8} m/cycle. Numbers in parentheses correspond to the crack growth sequences of the effective crack in Figure 4.15.

Vertical displacement and ϵ_{yy} strain contours corresponding to Figure 4.18 (a) and (b) are presented in Figure 4.21 and Figure 4.22, respectively. When a new crack

forms away from the main crack, vertical displacement and strains around the crack tip decrease, explaining the cause for low stress intensity factor in case Figure 4.18 (a).

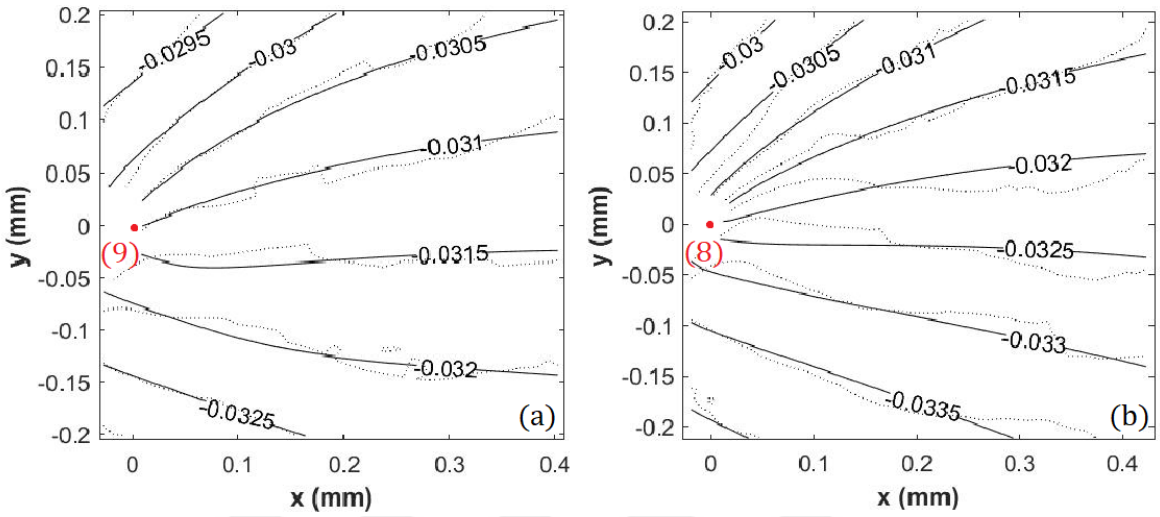

Figure 4.21. (a) Vertical displacement contours corresponding to Figure 4.18-(a), (b) to Figure 4.18-(b) (full lines: u_y from Equation. 4.2, dotted lines: DIC)(SM).

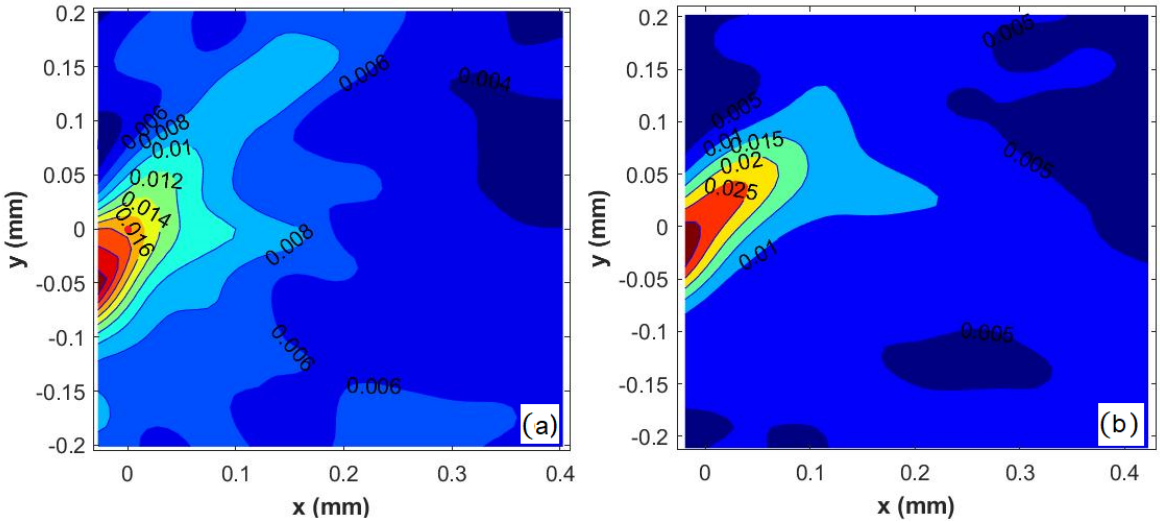

Figure 4.22. (a) ϵ_{yy} contours corresponding to Figure 4.18-(a), and (b) to Figure 4.18-(b), respectively (SM).

4.4. Summary and Conclusions

In Chapter 4, the crack growth under cyclic loading in CoNiAl shape memory specimens that have shape-memory behavior at room temperature, and superelastic behavior at 50 °C is studied in detail. Using edge-notched specimens, tests are carried out in superelastic and shape memory regimes, and the effects of the transformation and the secondary phase on crack growth are reported.

The optical microscopy images show the presence of a γ-phase around the notch, the dimensions of which have an effect on crack initiation. Crack initiates after 18000 loading cycles in the first (SE1), 3000 loading cycles in the second (SE2) superelastic specimen, and after 80000 loading cycles in the shape memory (SM) specimen, where the thicknesses of the γ-phase regions around the notch are different.

Test specimens that are examined post-failure with optical microscopy show the presence of γ-phase where and when the propagating cracks slow down, deviate, and/or stop. When the crack tip hits the non-transforming ductile γ-phase, first the crack stops, then it continues through the γ-phase with a slower crack growth rate (da/dN). In the meantime, the austenite region outside the γ-phase ahead of the crack tip starts to transform into martensite. During unloading, the reverse transformation is constrained by the γ-phase, a large area of residual martensite remains, in which a new crack forms and starts growing independent from the previous crack. Finally, the ductile γ-phase also cracks and the two cracks merge.

γ-phase formations positioned close to the main propagating crack tip increase the time to failure by blocking crack advancement. The first superelastic specimen and the shape memory specimen have comparable γ-phase volume fractions ahead of the growing crack tip but the shape memory specimen reaches failure after $\approx$ 24000 loading cycles and the first superelastic specimen fails after $\approx$ 36000 cycles which can be explained as a result of the higher number of γ-phase encounters during crack advancement in SE1. γ-phase regions in the first superelastic specimen are smaller in size, but greater in number than the ones in shape memory specimen (See Figures 4.6

& 4.7 and 4.19). In the second superelastic specimen due to the lack of γ-phase regions close to the main propagating crack tip (Figure 4.12), the main crack grows faster; and reaches failure in a shorter time at only 1664 cycles.

The insets in Figures 4.6, 4.12 and 4.19 show zigzag cracking pathways that are the consequence of γ-phase encounters, that deflect or stop cracks. All these occur because of the presence of the so called "barriers". Cracks stop growing or deflect when they reach γ-phase boundaries, so the γ-phase regions act as "barriers" to crack growth. (See Figure 1.8). However, a barrier does not always mean a non-penetrable region. Since the γ-phase is ductile and can deform plastically, it can absorb energy and inhibit fracture propagation, which causes the cracks to stop at the γ-phase boundaries. The γ-phase acts as a microstructural barrier in front of a crack tip compared to a homogeneous medium into which the crack grows. When the γ-phase size is small relative to the crack length, the crack either cuts through or bends around the γ-phase region depending on the stress distribution around the crack tip. If the γ-phase is large, however, it fatigues, and eventually breaks after cyclic loading.

Results of the present study show that the heat-treated CoNiAl has increased resistance to crack growth as a result of crack–γ phase interaction. In the absence of γ-phase the material is more brittle with less fracture resistance. The classical approach of LEFM captures the increase in fracture resistance, but it misses the considerable effect of microstructural behavior (crack interaction with transformed & re-oriented regions, and γ-phase) that is discussed in detail in this paper. One should be cautious with the toughness results reported in the literature.

5. SUMMARY AND CONCLUSIONS

In this thesis, the crack initiation and growth behavior of single crystal and polycrystalline shape memory alloys are investigated. The focus of the study was mostly on single crystal SMAs and on the effects of non-transforming microstructural phases, and martensitic phase transformation that forms at the crack tip and have important effects on their fracture behavior. In the following paragraphs, main results of the study are listed.

In Chapter 2, the fracture behavior of polycrystalline NiTi is discussed through extensive J-integral calculations. Initially, test specimens are loaded under cyclic loading at 1 Hz for 5000 cycles to obtain fatigue pre-cracks as per the ASTM E1820 standard. Following cyclic loading, crack lengths within the range of 0.45 to 0.55 times the width of the specimen are obtained. In all the specimens, cracks initiated from the notch making a 0° angle with the x-coordinate. Later, experiments are conducted at two different loading rates (0.1 and 0.5 mm/min) on polycrystalline NiTi compact tension specimens, and the load-displacement curves are obtained. J-Integrals are calculated from the areas under load-displacement curves, following the equations from ASTM E1820 standard [85].

Next, a series of finite elements analyses are conducted for the two loading rates. The energy release rate is calculated accounting for the elastic strain energy, transformation & heat dissipation energy of the whole model, via increasing the crack lengths for a length of "da" which are the crack growth lengths of the experiments. Later, the calculated energy release rate values are compared with the J-integrals given by ABAQUS, and the ones measured with experiments. Results showed that the energy release rate, as a result the energy required for crack initiation, increases with martensitic transformation and latent heat dissipation. At low loading rates the heat dissipation is low, so the energy required for crack initiation is determined mainly by the dissipation due martensitic transformation because a larger transformation region forms at the crack tip than at the crack tip of the higher loading rate case. However,

the inclusion of the heat dissipation energy showed the strongest effect on the energy release rate that is calculated from the results of the plate loaded at the higher loading rate. Since latent heat dissipation is higher at the higher loading rate case, the increase in the energy release rate is more pronounced with the inclusion of the heat dissipation energy.

Chapters 3 and 4 follow the findings of the fatigue crack initiation/growth experiments that were conducted on single edge notched single-crystal $Co_{36}Ni_{35}Al_{29}$ $(at.\%)$ shape memory alloy specimens with [100] crystallographic orientation. Prior to the experiments, all the specimens are heat treated at 1275 °C for 24 hours in a vacuum furnace, which are then left to cool in air at room temperature. Tensile tests are conducted on dog bone specimens to determine the material & mechanical behavior; shape memory behavior at room temperature (20 to 25 °C), and superelastic behavior at 50 °C is observed. For the fatigue crack initiation/growth tests, edge-notched dog-bone specimens are used. The edge notch is 0.5 mm long which is cut using EDM with a 0.1778 mm diameter wire. All specimens are polished to a mirror finish, and a fine speckle pattern is obtained by air blasting 1000 grit SiC powder on the surface. For the superelastic regime experiments, the specimens are heated to 50 °C using heating tapes; stress controlled tests are performed at 3 Hz frequency under a constant stress amplitude of 80.75 MPa with R=0.05. The shape memory regime experiments are conducted at room temperature (25 °C) under stress control with an amplitude of 57 MPa, and R=0.05. During the experiments, images of the area around the notch/crack tip are taken using a CCD camera which are then used to extract the full field displacement data via DIC.

In all the experiments that are conducted in the superelastic regimes, cracks initiated from the notch with a magnitude of 43 $\pm 1^{\circ}$ angle, later grew along a similar angle to the initial crack from the notch despite some deviations due to micro-structural barriers [98]. In the experiments, the crack initiation and subsequent growth directions are found to be following a similar angle to the martensitic localization band angle that forms in the tension specimens. Defining the martensite band angle as a material anisotropy direction, crack initiation angles in edge notched single crystal CoNiAl shape

memory alloys are calculated analytically using the Maximum Tangential Stress (MTS), the Maximum Energy Release Rate (MERR), Strain Energy Density (SED) Criteria, and computationally using finite elements (ABAQUS).

Since the available equations for MTS, MERR, and SED criteria are for sharp cracks, for the crack initiation angle calculations from the notch, stress intensity factors for u-notches that depend on the geometrical parameters of the notch are used. The 2D stress field around the notch for the plane stress case is calculated using the equations of Sih *et al.* [100]. T-stress is added to the tangential stress calculations, and tangential stress distribution around the notch is plotted as function of the angle θ. Two local maxima are found, the maximum of which occurs at $\theta = 42.3°$. Later, energy release rates are calculated following the equations given by Yang and Yuan [105] and Sakha *et al.* [104] that were proposed for anisotropic non-transforming materials. Energy release rate distribution plots around the notch revealed the maximum occurs at an angle of $\theta = 41.6°$. According to the strain energy density distribution around the notch that was plotted as a function of the polar angle θ using the equations given by Gdoutos *et al.* [102], the maximum strain energy density occurs at an angle of $\theta = 40.9°$.

Finite elements analyses are performed using the anisotropic material properties of the single crystal CoNiAl that were defined with a material orientation angle. Tangential stress and strain energy density field around the notch are plotted; and the energy release rates are calculated from the strain and transformation energy results of the whole model for small cracks around the notch. Maximum tangential stress and the maximum energy release rate values are found at an angle of $\approx 41°$, while the maximum strain energy density is found at $\theta = 38°$. Overall, the crack initiation angles calculated analytically and computationally are found to be in good agreement with the results of the experiments. The work presented in Chapter 3 is submitted as a journal article, and is currently published which can be found as an online first article [161].

In Chapter 4, the results of fatigue crack growth tests conducted at shape memory and superelastic regimes using edge notched single crystal $Co_{36}Ni_{35}Al_{29}\,(at.\%)$ shape

memory alloy specimens with [100] crystallographic orientation are presented. Crack tip displacement equations for linear elastic anisotropic bodies of Sih *et al.* [100] are used for least square fitting the displacement data obtained from DIC for extraction of mode I & II stress intensity factors, and the unknown material properties.

The material properties obtained from least squares fitting belong to the region around the crack tip where the transforming and the non-transforming phases coexist. In the literature, the material properties used usually belong to the bulk material which do not give proper results in the presence of different phases around the crack tip. Therefore, the material properties extracted from the crack tip region in the presence of transforming and non-transforming phases are found to be more reliable for the calculations of this study.

The crack growth behavior, fracture parameters and crack growth rates, which are found to fluctuate during propagation, are discussed in detail. To determine the cause of this unexpected behavior, postmortem samples are cleared of the DIC paint and examined under an optical microscope. Non-transforming secondary phase regions that act as barriers to crack growth has been found to occur in areas where the crack growth has slowed down/stopped. It is shown that the increasing/decreasing behavior in the crack growth rates and fracture parameters are a result of non-transforming secondary phases (γ-phases) that form due to heat treatment. When a propagating crack tip hits the boundary of the secondary phase, growth initially stops then continues significantly slower inside the secondary phase. In other cases, it was observed that the crack propagation direction deflects and follows a path outside of the non-transforming γ-phase. In each case, the crack-secondary phase interactions increase the time to failure by blocking/decelerating crack growth. The work presented in Chapter 4 is submitted as a journal article, and is recently accepted for publication [98].

To sum up, overall results of the study show that a macroscopic study of the fracture behavior of shape memory alloys falls short in explaining the behavior of the SMA. One should not forget to look at the region around the crack tip in detail and should not neglect the effect of microstructural behavior; crack interaction with transformed &

re-oriented regions, and non-transforming secondary phases. Additionally, martensitic transformation has a substantial effect on cracking behavior of shape memory alloys. In single crystal shape memory alloys, cracks follow the martensitic transformation bands, and in polycrystalline SMAs the amount of phase transformation becomes important due to the energy dissipation via martensitic transformation and latent heat generation.

REFERENCES

1. Yoneyama, T. and S. Miyazaki, *Shape Memory Alloys for Biomedical Applications*, Elsevier, UK, 2008.

2. Lagoudas, D. C., *Shape Memory Alloys: Modeling and Engineering Applications*, Springer, USA, 2008.

3. Efstathiou, C., H. Sehitoglu, A. W. Johnson, R. F. Hamilton, H. Maier and Y. Chumlyakov, "Large Reduction in Critical Stress in Co–Ni–Al Upon Repeated Transformation", *Scripta Materialia*, Vol. 51, No. 10, pp. 979–985, 2004.

4. Dilibal, S., H. Sehitoglu, R. F. Hamilton, H. Maier and Y. Chumlyakov, "On the Volume Change in Co–Ni–Al During Pseudoelasticity", *Materials Science and Engineering: A*, Vol. 528, No. 6, pp. 2875–2881, 2011.

5. Hamilton, R. F., H. Sehitoglu, C. Efstathiou, H. Maier and Y. Chumlyakov, "Pseudoelasticity in Co–Ni–Al Single and Polycrystals", *Acta Materialia*, Vol. 54, No. 3, pp. 587–599, 2006.

6. Tanaka, Y., T. Ohmori, K. Oikawa, R. Kainuma and K. Ishida, "Ferromagnetic Co-Ni-Al Shape Memory Alloys with Beta+Gamma Two-Phase Structure", *Materials Transactions*, Vol. 45, No. 2, pp. 427–430, 2004.

7. Oikawa, K., L. Wulff, T. Iijima, F. Gejima, T. Ohmori, a. Fujita, K. Fukamichi, R. Kainuma and K. Ishida, "Promising Ferromagnetic Ni–Co–Al Shape Memory Alloy System", *Applied Physics Letters*, Vol. 79, No. 20, pp. 3290–3292, 2001.

8. Oikawa, K., T. Omori, Y. Sutou, R. Kainumal and K. Ishidal, "Development of the Co-Ni-Al Ferromagnetic Shape Memory Alloys", *Journal De Physique Iv (Proceedings)*, Vol. 112, pp. 1017–1020, EDP Sciences, 2003.

9. Hamilton, R. F., H. Sehitoglu, C. Efstathiou, H. Maier, Y. Chumlyakov and X. Zhang, "Transformation of Co–Ni–Al Single Crystals in Tension", *Scripta Materialia*, Vol. 53, No. 1, pp. 131–136, 2005.

10. Kanth, B. R., N. Ramarao, A. Panda, R. Gopalan, A. Mitra and P. Mukhopadhyay, "Effect of Annealing on the Martensitic Transformation of a CoNiAl Ferromagnetic Shape Memory Alloy", *Journal of Alloys and Compounds*, Vol. 491, No. 1-2, pp. 22–25, 2010.

11. Irie, M., K. Otsuka and C. Wayman, *Shape Memory Materials*, Cambridge Univ. Press, Cambridge, UK, 1998.

12. Dar, R. D., H. Yan and Y. Chen, "Grain Boundary Engineering of Co–Ni–Al, Cu–Zn–Al, and Cu–Al–Ni Shape Memory Alloys by Intergranular Precipitation of a Ductile Solid Solution Phase", *Scripta Materialia*, Vol. 115, pp. 113–117, 2016.

13. Meyer, D., H. Maier, J. Dadda, I. Karaman and H. Karaca, "Thermally and Stress-Induced Martensitic Transformation in Co–Ni–Al Ferromagnetic Shape Memory Alloy Single Crystals", *Materials Science and Engineering: A*, Vol. 438, pp. 875–878, 2006.

14. Chumlyakov, Y., E. Panchenko, I. Kireeva, I. Karaman, H. Sehitoglu, H. Maier, A. Tverdokhlebova and A. Ovsyannikov, "Orientation Dependence and Tension/Compression Asymmetry of Shape Memory Effect and Superelasticity in Ferromagnetic Co40ni33al27, Co49ni21ga30 and Ni54fe19ga27 Single Crystals", *Materials Science and Engineering: A*, Vol. 481, pp. 95–100, 2008.

15. Chumlyakov, Y. I., I. Kireeva, E. Y. Panchenko, E. Timofeeva, Z. Pobedennaya, S. Chusov, I. Karaman, H. Maier, E. Cesari and V. Kirillov, "High-Temperature Superelasticity in CoNiGa, CoNiAl, Nifega, and TiNi Monocrystals", *Russian Physics Journal*, Vol. 51, No. 10, pp. 1016–1036, 2008.

16. Eftifeeva, A., E. Panchenko, Y. Chumlyakov, E. Yanushonite, G. Gerstein and H. J. Maier, "Compressive Response of High-Strength [001]-Oriented Single Crystals of a Co35ni35al30 Shape Memory Alloy", *Journal of Alloys and Compounds*, Vol. 787, pp. 963–971, 2019.

17. Bhattacharya, K., *Microstructure of Martensite: Why It Forms and How It Gives Rise to the Shape-Memory Effect*, Vol. 2, Oxford University Press, UK, 2003.

18. Liu, J., H. Zheng and J. Li, "Effect of Solidification Rate on Microstructure and Crystal Orientation of Ferromagnetic Shape Memory Alloys Co–Ni–Al", *Materials Science and Engineering: A*, Vol. 438, pp. 1061–1064, 2006.

19. Karaca, H., I. Karaman, Y. Chumlyakov, D. Lagoudas and X. Zhang, "Compressive Response of a Single Crystalline CoNiAl Shape Memory Alloy", *Scripta Materialia*, Vol. 51, No. 3, pp. 261–266, 2004.

20. Eftifeeva, A., E. Panchenko, Y. Chumlyakov and H. J. Maier, "Two-Way Shape Memory Effect in [001] B2-Oriented Co-Ni-Al Single Crystals", *Materials Today: Proceedings*, Vol. 4, No. 3, pp. 4789–4796, 2017.

21. Sutou, Y., R. Kainuma, K. Ishida and M. Taya, "Martensitic Transformation Behavior Under Magnetic Field in Co-Ni-Al Ferromagnetic Shape Memory Alloys", *Smart Structures and Materials 2003: Active Materials: Behavior and Mechanics*, Vol. 5053, pp. 159–168, International Society for Optics and Photonics, 2003.

22. Tanaka, Y., K. Oikawa, Y. Sutou, T. Omori, R. Kainuma and K. Ishida, "Martensitic Transition and Superelasticity of Co–Ni–Al Ferromagnetic Shape Memory Alloys with Beta+Gamma Two-Phase Structure", *Materials Science and Engineering: A*, Vol. 438, pp. 1054–1060, 2006.

23. Chumlyakov, Y. I., I. Kireeva, I. Karaman, E. Y. Panchenko, E. Zakharova, A. Tverskov, A. Ovsyannikov, K. Nazarov and V. Kirillov, "Orientational Dependence of Shape Memory Effects and Superelasticity in CoNiGa, Nimnga, CoNiAl,

Fenicoti, and TiNi Single Crystals", *Russian Physics Journal*, Vol. 47, No. 9, pp. 893–911, 2004.

24. Kumar, S. and W. A. Curtin, "Crack Interaction with Microstructure", *Materials Today*, Vol. 10, No. 9, pp. 34–44, 2007.

25. Frenzel, J., E. P. George, A. Dlouhy, C. Somsen, M.-X. Wagner and G. Eggeler, "Influence of Ni on Martensitic Phase Transformations in NiTi Shape Memory Alloys", *Acta Materialia*, Vol. 58, No. 9, pp. 3444–3458, 2010.

26. Chekotu, J. C., R. Groarke, K. O'toole and D. Brabazon, "Advances in Selective Laser Melting of NiTinol Shape Memory Alloy Part Production", *Materials*, Vol. 12, No. 5, p. 809, 2019.

27. Duerig, T. W., K. Melton and D. Stöckel, *Engineering Aspects of Shape Memory Alloys*, Butterworth-Heinemann, UK, 2013.

28. Miyazaki, S., "My Experience with Ti–Ni-Based and Ti-Based Shape Memory Alloys", *Shape Memory and Superelasticity*, Vol. 3, pp. 279–314, 2017.

29. Mckelvey, A. and R. Ritchie, "Fatigue-Crack Propagation in NiTinol, a Shape-Memory and Superelastic Endovascular Stent Material", *Journal of Biomedical Materials Research*, Vol. 47, No. 3, pp. 301–308, 1999.

30. Daly, S., a. Miller, G. Ravichandran and K. Bhattacharya, "An Experimental Investigation of Crack INiTiation in Thin Sheets of NiTinol", *Acta Materialia*, Vol. 55, No. 18, pp. 6322–6330, 2007.

31. Robertson, S., A. Mehta, A. Pelton and R. Ritchie, "Evolution of Crack-Tip Transformation Zones in Superelastic NiTinol Subjected to in-situ Fatigue: A Fracture Mechanics and Synchrotron X-Ray Microdiffraction Analysis", *Acta Materialia*, Vol. 55, No. 18, pp. 6198–6207, 2007.

32. Jiang, F. and K. S. Vecchio, "Fracture of NiTinol Under Quasistatic and Dynamic

Loading", *Metallurgical and Materials Transactions A*, Vol. 38, No. 12, pp. 2907–2915, 2007.

33. Wang, X., B. Xu, Z. Yue and X. Tong, "Fracture Behavior of the Compact Tension Specimens in NiTi Shape Memory Alloys", *Materials Science and Engineering: A*, Vol. 485, No. 1, pp. 14–19, 2008.

34. Gollerthan, S., D. Herberg, A. Baruj and G. Eggeler, "Compact Tension Testing of Martensitic/Pseudoplastic NiTi Shape Memory Alloys", *Materials Science and Engineering: A*, Vol. 481, pp. 156–159, 2008.

35. Committee, A. E., "Standard Test Method for Linear-Elastic Plane-Strain Fracture Toughness KIc of Metallic Materials", *Annual Book of ASTM Standards*, 2012.

36. Gloanec, A.-L., P. Cerracchio, B. Reynier, A. Van Herpen and P. Riberty, "Fatigue Crack INiTiation and Propagation of a TiNi Shape Memory Alloy", *Scripta Materialia*, Vol. 62, No. 10, p. 786, 2010.

37. Maletta, C., E. Sgambitterra and F. Niccoli, "Temperature Dependent Fracture Properties of Shape Memory Alloys: Novel Findings and a Comprehensive Model", *Scientific Reports*, Vol. 6, No. 1, p. 17, 2016.

38. Ungár, T., J. Frenzel, S. Gollerthan, G. Ribárik, L. Balogh and G. Eggeler, "On the Competition Between the Stress-Induced Formation of Martensite and Dislocation Plasticity During Crack Propagation in Pseudoelastic NiTi Shape Memory Alloys", *Journal of Materials Research*, Vol. 32, No. 23, pp. 4433–4442, 2017.

39. Katanchi, B., N. Choupani, J. Khalil-Allafi, R. Tavangar and M. Baghani, "Mixed-Mode Fracture of a Superelastic NiTi Alloy: Experimental and Numerical Investigations", *Engineering Fracture Mechanics*, Vol. 190, pp. 273–287, 2018.

40. Haghgouyan, B., C. Hayrettin, T. Baxevanis, I. Karaman and D. C. Lagoudas,

"Fracture Toughness of NiTi–Towards Establishing Standard Test Methods for Phase Transforming Materials", *Acta Materialia*, Vol. 162, pp. 226–238, 2019.

41. Young, B., B. Haghgouyan, D. Lagoudas and I. Karaman, "Effect of Temperature on the Fracture Toughness of a NiTiHf High Temperature Shape Memory Alloy", *Shape Memory and Superelasticity*, Vol. 5, pp. 362–373, 2019.

42. Mutlu, F., G. Anlaş and Z. Moumni, "Effect of Loading Rate on Fracture Mechanics of NiTi Sma", *International Journal of Fracture*, Vol. 224, No. 2, pp. 151–165, 2020.

43. Haghgouyan, B., B. Young, S. Picak, T. Baxevanis, I. Karaman and D. C. Lagoudas, "A Unified Description of Mechanical and Actuation Fatigue Crack Growth in Shape Memory Alloys", *Acta Materialia*, Vol. 217, p. 117155, 2021.

44. Makkar, J., B. Young, I. Karaman and T. Baxevanis, "Fracture Resistance of Shape Memory Alloys Under Thermomechanical Loading", *Engineering Fracture Mechanics*, Vol. 258, p. 108059, 2021.

45. Jape, S., B. Young, B. Haghgouyan, C. Hayrettin, T. Baxevanis, D. Lagoudas and I. Karaman, "Actuation-Induced Stable Crack Growth in Near-Equiatomic Nickel-Titanium Shape Memory Alloys: Experimental and Numerical Analysis", *International Journal of Solids and Structures*, Vol. 221, pp. 165–179, 2021.

46. Seyedzavvar, M., C. Boğa and N. Choupani, "Experimental Investigation and Numerical Analysis: Fracture Mechanics and Microstructural Development in Ni55.8Ti Superalloy Under Mixed-Mode Loading at Different Temperatures", *Meccanica*, Vol. 57, No. 8, pp. 2067–2084, 2022.

47. Usha, M., S. V. K. Tataverthi, S. R. Devisetty and V. Siddardha, "Experimental Investigation on Fracture Toughness of Cu-Based Shape Memory Alloys with Silver Addition", *Materials Today: Proceedings*, 2023.

48. Stam, G. and E. Van Der Giessen, "Effect of Reversible Phase Transformations on Crack Growth", *Mechanics of Materials*, Vol. 21, No. 1, pp. 51–71, 1995.

49. Sun, Q., K. C. Hwang and S. Yu, "A Micromechanics Constitutive Model of Transformation Plasticity with Shear and Dilatation Effect", *Journal of the Mechanics and Physics of Solids*, Vol. 39, No. 4, pp. 507–524, 1991.

50. Birman, V., "On Mode I Fracture of Shape Memory Alloy Plates", *Smart Materials and Structures*, Vol. 7, No. 4, p. 433, 1998.

51. Tanaka, K. and Y. Sato, "Analysis of Superplastic Deformation During Isothermal Martensitic Transformation", *Res Mech.*, Vol. 17, No. 3, pp. 241–252, 1986.

52. Yi, S. and S. Gao, "Fracture Toughening Mechanism of Shape Memory Alloys Due to Martensite Transformation", *International Journal of Solids and Structures*, Vol. 37, No. 38, pp. 5315–5327, 2000.

53. Eshelby, J. D., "The Determination of the Elastic Field of An Ellipsoidal Inclusion, and Related Problems", *Proceedings of the Royal Society of London A: Mathematical, Physical and Engineering Sciences*, Vol. 241, pp. 376–396, The Royal Society, 1957.

54. Sun, Q. P. and K. C. Hwang, "Micromechanics Modelling for the Constitutive Behavior of Polycrystalline Shape Memory Alloys—I. Derivation of General Relations", *Journal of the Mechanics and Physics of Solids*, Vol. 41, No. 1, pp. 1–17, 1993.

55. Yan, W., C. H. Wang, X. P. Zhang and Y.-W. Mai, "Effect of Transformation Volume Contraction on the Toughness of Superelastic Shape Memory Alloys", *Smart Materials and Structures*, Vol. 11, No. 6, p. 947, 2002.

56. Mcmeeking, R. and A. Evans, "Mechanics of Transformation-Toughening in Brittle Materials", *Journal of the American Ceramic Society*, Vol. 65, No. 5, pp.

242–246, 1982.

57. Hutchinson, J. W., "On Steady Quasi-Static Crack Growth", *Harvard University Report Deap S-8 (Afosr-Tr-74-1042)*, 1974.

58. Wang, G., "Effects of Notch Geometry on Stress–Strain Distribution, Martensite Transformation and Fracture Behavior in Shape Memory Alloy NiTi", *Materials Science and Engineering: A*, Vol. 434, No. 1, pp. 269–279, 2006.

59. Freed, Y. and L. Banks-Sills, "Crack Growth Resistance of Shape Memory Alloys by Means of a Cohesive Zone Model", *Journal of the Mechanics and Physics of Solids*, Vol. 55, No. 10, pp. 2157–2180, 2007.

60. Panoskaltsis, V., S. Bahuguna and D. Soldatos, "On the Thermomechanical Modeling of Shape Memory Alloys", *International Journal of Non-Linear Mechanics*, Vol. 39, No. 5, pp. 709–722, 2004.

61. Lexcellent, C. and F. Thiebaud, "Determination of the Phase Transformation Zone at a Crack Tip in a Shape Memory Alloy Exhibiting Asymmetry Between Tension and Compression", *Scripta Materialia*, Vol. 59, No. 3, pp. 321–323, 2008.

62. Raniecki, B. and C. Lexcellent, "Thermodynamics of Isotropic Pseudoelasticity in Shape Memory Alloys", *European Journal of Mechanics-A/Solids*, Vol. 17, No. 2, pp. 185–205, 1998.

63. Falvo, A., F. Furgiuele, A. Leonardi and C. Maletta, "Stress-Induced Martensitic Transformation in the Crack Tip Region of a NiTi Alloy", *Journal of Materials Engineering and Performance*, Vol. 18, No. 5-6, pp. 679–685, 2009.

64. Maletta, C. and M. Young, "Stress-Induced Martensite in Front of Crack Tips in NiTi Shape Memory Alloys: Modeling Versus Experiments", *Journal of Materials Engineering and Performance*, Vol. 20, No. 4-5, pp. 597–604, 2011.

65. Maletta, C. and F. Furgiuele, "Analytical Modeling of Stress-Induced Marten-

sitic Transformation in the Crack Tip Region of Nickel–Titanium Alloys", *Acta Materialia*, Vol. 58, No. 1, pp. 92–101, 2010.

66. Gollerthan, S., M. Young, A. Baruj, J. Frenzel, W. W. Schmahl and G. Eggeler, "Fracture Mechanics and Microstructure in NiTi Shape Memory Alloys", *Acta Materialia*, Vol. 57, No. 4, pp. 1015–1025, 2009.

67. Baxevanis, T. and D. Lagoudas, "A Mode I Fracture Analysis of a Center-Cracked Infinite Shape Memory Alloy Plate Under Plane Stress", *International Journal of Fracture*, Vol. 175, No. 2, pp. 151–166, 2012.

68. Dugdale, D. S., "Yielding of Steel Sheets Containing Slits", *Journal of the Mechanics and Physics of Solids*, Vol. 8, No. 2, pp. 100–104, 1960.

69. Ardakani, S. H., H. Ahmadian and S. Mohammadi, "Thermo-Mechanically Coupled Fracture Analysis of Shape Memory Alloys Using the Extended Finite Element Method", *Smart Materials and Structures*, Vol. 24, No. 4, p. 045031, 2015.

70. Ardakani, S. H., A. Afshar and S. Mohammadi, "Numerical Study of Thermo-Mechanical Coupling Effects on Crack Tip Fields of Mixed-Mode Fracture in Pseudoelastic Shape Memory Alloys", *International Journal of Solids and Structures*, Vol. 81, pp. 160–178, 2016.

71. Haghgouyan, B., S. Jape, T. Baxevanis, I. Karaman and D. C. Lagoudas, "Stable Crack Growth in NiTi Shape Memory Alloys: 3d Finite Element Modeling and Experimental Validation", *Smart Materials and Structures*, Vol. 28, No. 6, p. 064001, 2019.

72. Simoes, M. and E. Martínez-Pañeda, "Phase Field Modelling of Fracture and Fatigue in Shape Memory Alloys", *Computer Methods in Applied Mechanics and Engineering*, Vol. 373, p. 113504, 2021.

73. Xiong, J., B. Xu and G. Kang, "Phase Field Simulation on the Martensite Trans-

formation and Reorientation Toughening Behaviors of Single Crystal NiTi Shape Memory Alloy: Effects of Crystalline Orientation and Temperature", *Engineering Fracture Mechanics*, Vol. 270, p. 108585, 2022.

74. Hasan, M., M. Zhang and T. Baxevanis, "A Finite-Strain Phase-Field Description of Thermomechanically Induced Fracture in Shape Memory Alloys", *Shape Memory and Superelasticity*, pp. 1–17, 2022.

75. Zhang, Y., K. Guo and S. Jiang, "Influence of Amorphous Phase on Crack INiTiation and Propagation Behaviours in NiTi Shape Memory Alloy Based on Extended Finite Element Simulation", *Iop Conference Series: Materials Science and Engineering*, Vol. 1270, p. 012119, IOP, 2022.

76. Cui, Y., X. Zeng, V. B. Tan and Z. Zhang, "Experimental and Numerical Studies of NiTi Dynamic Fracture Behaviors Under the Impact Loading", *International Journal of Mechanical Sciences*, Vol. 235, p. 107724, 2022.

77. Voyiadjis, G. Z., H. Bahrami and S. Hoseini, "Fracture Analysis of Shape Memory Alloy Considering the Effect of Ti-Rich Areas", *Engineering Failure Analysis*, Vol. 143, p. 106879, 2023.

78. Sgambitterra, E., Y. M. Hashemi, M. Kadkhodaei, P. Magarò, F. Niccoli and C. Maletta, "A Novel Energetic Approach for Predicting Fatigue Crack Growth in Pseudoelastic NiTi Alloys", *Materials Letters*, p. 134755, 2023.

79. Xie, G., F. Wang, X. Lai, Z. Xu and X. Zeng, "Atomistic Study on Crystal Orientation-Dependent Crack Propagation and Resultant Microstructure Anisotropy in NiTi Alloys", *International Journal of Mechanical Sciences*, Vol. 250, p. 108320, 2023.

80. Yan, B., Y. Zhang, S. Jiang, J. Yu, D. Sun and M. Tang, "Mechanical Properties and Fracture Mechanisms of Martensitic NiTi Shape Memory Alloy Based on Various Thermomechanical-Processing Microstructures", *Journal of Alloys and*

Compounds, Vol. 883, p. 160797, 2021.

81. Amin-Ahmadi, B., R. D. Noebe and A. P. Stebner, "Crack Propagation Mechanisms of an Aged Nickel-Titanium-Hafnium Shape Memory Alloy", *Scripta Materialia*, Vol. 159, pp. 85–88, 2019.

82. Erdogan, F. and G. Sih, "On the Crack Extension in Plates Under Plane Loading and Transverse Shear", *Journal of Basic Engineering*, 1963.

83. Zhang, Y., Y. You, Z. Moumni, G. Anlas, J. Zhu and W. Zhang, "Stored-Energy-Based Fatigue Criterion for Shape Memory Alloys", *Smart Materials and Structures*, Vol. 28, No. 6, p. 065027, 2019.

84. Zhang, Y., Z. Moumni, Y. You, J. Zhu and W. Zhang, "Energy-Based Analysis of Temperature Oscillation at the Shakedown State in Shape Memory Alloys", *Continuum Mechanics and Thermodynamics*, pp. 1–13, 2019.

85. Committee, A. E.-., "Standard Test Method for Measurement of Fracture Toughness", *Annual Book of ASTM Standards*, Vol. 18a, 2019.

86. Auricchio, F., R. L. Taylor and J. Lubliner, "Shape-Memory Alloys: Macromodelling and Numerical Simulations of the Superelastic Behavior", *Computer Methods in Applied Mechanics and Engineering*, Vol. 146, No. 3-4, pp. 281–312, 1997.

87. Anderson, T. L., *Fracture Mechanics: Fundamentals and Applications*, Crc Press, USA, 1995.

88. *Abaqus/Simulia User Assistance*, Dassault Systèmes Simulia Corp, 2021.

89. Baxevanis, T., A. Parrinello and D. Lagoudas, "On the Fracture Toughness Enhancement Due to Stress-Induced Phase Transformation in Shape Memory Alloys", *International Journal of Plasticity*, Vol. 50, pp. 158–169, 2013.

90. Baxevanis, T., C. M. Landis and D. C. Lagoudas, "On the Effect of Latent Heat

on the Fracture Toughness of Pseudoelastic Shape Memory Alloys", *Journal of Applied Mechanics*, Vol. 81, No. 10, p. 101006, 2014.

91. Cissé, C. and M. A. Zaeem, "Transformation-Induced Fracture Toughening in Cualbe Shape Memory Alloys: A Phase-Field Study", *International Journal of Mechanical Sciences*, Vol. 192, p. 106144, 2021.

92. Loughran, G., T. Shield and P. Leo, "Fracture of Shape Memory Cualni Single Crystals", *International Journal of Solids and Structures*, Vol. 40, No. 2, pp. 271–294, 2003.

93. Paranjape, H. M., M. L. Bowers, M. J. Mills and P. M. Anderson, "Mechanisms for Phase Transformation Induced Slip in Shape Memory Alloy Micro-Crystals", *Acta Materialia*, Vol. 132, pp. 444–454, 2017.

94. Sidharth, R., Y. Wu, F. Brenne, W. Abuzaid and H. Sehitoglu, "Relationship Between Functional Fatigue and Structural Fatigue of Iron-Based Shape Memory Alloy Femnnial", *Shape Memory and Superelasticity*, 2020.

95. Xiong, F., Y. Liu and E. Pagounis, "Fracture Mechanism of a Ni–Mn–Ga Ferromagnetic Shape Memory Alloy Single Crystal", *Journal of Magnetism and Magnetic Materials*, Vol. 285, No. 3, pp. 410–416, 2005.

96. Creuziger, A., L. Bartol, K. Gall and W. Crone, "Fracture in Single Crystal NiTi", *Journal of the Mechanics and Physics of Solids*, Vol. 56, No. 9, pp. 2896–2905, 2008.

97. Mirsayar, M. and D. Hartl, "On the Validity of Strain Energy Density Criterion for Mixed Mode I/II Fracture Analysis of Notched Shape Memory Alloy Components", *Engineering Fracture Mechanics*, Vol. 214, pp. 270–288, 2019.

98. Mutlu, F., G. Anlaş and H. Şehitoğlu, "The Effect of Microstructural Barriers on Transient Crack Growth in Shape Memory Alloys", *Smart Materials and Struc-*

tures, Vol. 32, No. 9, p. 095006, 2023.

99. Sih, G. C., "Strain-Energy-Density Factor Applied to Mixed Mode Crack Problems", *International Journal of Fracture*, Vol. 10, No. 3, pp. 305–321, 1974.

100. Sih, G. C., P. Paris and G. Irwin, "On Cracks in Rectilinearly Anisotropic Bodies", *International Journal of Fracture Mechanics*, Vol. 1, No. 3, pp. 189–203, 1965.

101. Abuzaid, W. and H. Sehitoglu, "Superelasticity and Functional Fatigue of Single Crystalline Fenicoalti Iron-Based Shape Memory Alloy", *Materials & Design*, Vol. 160, pp. 642–651, 2018.

102. Gdoutos, E., D. Zacharopoulos and E. Meletis, "Mixed-Mode Crack Growth in Anisotropic Media", *Engineering Fracture Mechanics*, Vol. 34, No. 2, pp. 337–346, 1989.

103. Filippi, S., P. Lazzarin and R. Tovo, "Developments of Some Explicit Formulas Useful to Describe Elastic Stress Fields Ahead of Notches in Plates", *International Journal of Solids and Structures*, Vol. 39, No. 17, pp. 4543–4565, 2002.

104. Sakha, M., M. Nejati, A. Aminzadeh, S. Ghouli, M. O. Saar and T. Driesner, "On the Validation of Mixed-Mode I/Iı Crack Growth Theories for Anisotropic Rocks", *International Journal of Solids and Structures*, Vol. 241, p. 111484, 2022.

105. Yang, S. and F.-G. Yuan, "Kinked Crack in Anisotropic Bodies", *International Journal of Solids and Structures*, Vol. 37, No. 45, pp. 6635–6682, 2000.

106. Azhdari, A. and S. Nemat-Nasser, "Energy-Release Rate and Crack Kinking in Anisotropic Brittle Solids", *Journal of the Mechanics and Physics of Solids*, Vol. 44, No. 6, pp. 929–951, 1996.

107. Zhang, S., B. Jang, B. Valaire and J. Suhling, "A New Criterion for Composite Material Mixed Mode Fracture Analysis", *Engineering Fracture Mechanics*, Vol. 34, No. 3, pp. 749–769, 1989.

108. Zhiming, Y. and M. Ayari, "Prediction of Crack Propagation in Anisotropic Solids", *Engineering Fracture Mechanics*, Vol. 49, No. 6, pp. 797–808, 1994.

109. Nejati, M., A. Aminzadeh, F. Amann, M. O. Saar and T. Driesner, "Mode I Fracture Growth in Anisotropic Rocks: Theory and Experiment", *International Journal of Solids and Structures*, Vol. 195, pp. 74–90, 2020.

110. Ma, Y., S. Yang, Y. Liu and X. Liu, "The Ductility and Shape-Memory Properties of Ni–Mn–Co–Ga High-Temperature Shape-Memory Alloys", *Acta Materialia*, Vol. 57, No. 11, pp. 3232–3241, 2009.

111. Wu, Z., Z. Liang, Y. Zhang, Z. Liu, J. Zhang, F. Motazedian, S. Bakhtiari, B. S. Shariat, Y. Liu, Y. Ren and H. Yang, "A Eutectic Dual-Phase Design Towards Superior Mechanical Properties of Heusler-Type Ferromagnetic Shape Memory Alloys", *Acta Materialia*, Vol. 181, pp. 278–290, 2019.

112. Euh, K., J.-M. Lee, D.-H. Nam and S. Lee, "In-Situ Fracture Observation and Fracture Toughness Analysis of Ni-Mn-Ga-Fe Ferromagnetic Shape Memory Alloys", *Metallurgical and Materials Transactions A*, Vol. 42, No. 13, pp. 3961–3968, 2011.

113. Canadinc, D., J. Dadda, H. J. Maier, I. Karaman, H. E. Karaca and Y. I. Chumlyakov, "On the Role of the Cooling Rate and Crystallographic Orientation on the Shape Memory Properties of CoNiAl Single Crystals Under Compression", *Smart Materials and Structures*, Vol. 16, No. 4, p. 1006, 2007.

114. Dar, R. D. and Y. Chen, "Nanoindentation Studies of Small-Scale Martensitic Transformations and Ductile Precipitate Effects in Dual-Phase Polycrystalline Shape Memory Alloys", *Acta Materialia*, Vol. 91, pp. 112–127, 2015.

115. Eftifeeva, A. S., E. Y. Panchenko and Y. I. Chumlyakov, "The Effect of Thermal Cycling and Stress-Assistant Ageing Two Way Shape Memory Effect in [123] Oriented Co40ni33al27 Single Crystals", *Iop Conference Series: Materials Science*

and Engineering, Vol. 71, p. 012060, IOP, 2015.

116. Panchenko, E., A. Eftifeeva, Y. Chumlyakov, G. Gerstein and H. Maier, "Two-Way Shape Memory Effect and Thermal Cycling Stability in Co35ni35al30 Single Crystals by Low-Temperature Martensite Ageing", *Scripta Materialia*, Vol. 150, pp. 18–21, 2018.

117. Gerstein, G., G. Firstov, T. Kosorukova, Y. N. Koval and H. Maier, "Development of B2 Shape Memory Intermetallics Beyond Nial, CoNiAl and CoNiGa", *Shape Memory and Superelasticity*, Vol. 4, No. 3, pp. 360–368, 2018.

118. Ishida, K., R. Kainuma, N. Ueno and T. Nishizawa, "Ductility Enhancement in Nial (B2)-Base Alloys by Microstructural Control", *Metallurgical Transactions A*, Vol. 22, No. 2, pp. 441–446, 1991.

119. Oikawa, K., T. Ota, F. Gejima, T. Ohmori, R. Kainuma and K. Ishida, "Phase Equilibria and Phase Transformations in New B2-Type Ferromagnetic Shape Memory Alloys of Co-Ni-Ga and Co-Ni-Al Systems", *Materials Transactions*, Vol. 42, No. 11, pp. 2472–2475, 2001.

120. Wolf, B., K.-O. Bambauer and P. Paufler, "On the Temperature Dependence of the Hardness of Quasicrystals", *Materials Science and Engineering: A*, Vol. 298, No. 1-2, pp. 284–295, 2001.

121. Fujita, A., H. Morito, T. Kudo, K. Fukamichi, R. Kainuma, K. Ishida and K. Oikawa, "Magnetocrystalline Anisotropy in a Single-Variant Co-Ni-Al Ferromagnetic Shape Memory Alloy", *Materials Transactions*, Vol. 44, No. 10, pp. 2180–2183, 2003.

122. Karaca, H., I. Karaman, D. Lagoudas, H. Maier and Y. I. Chumlyakov, "Recoverable Stress-Induced Martensitic Transformation in a Ferromagnetic CoNiAl Alloy", *Scripta Materialia*, Vol. 49, No. 9, pp. 831–836, 2003.

123. Liu, Z., X. Dai, Z. Zhu, H. Hu, J. Chen, G. Liu and G. Wu, "Martensitic Transformation and Magnetic Properties of Co–Ni–Al Shape Memory Alloy Ribbons", *Journal of Physics D: Applied Physics*, Vol. 37, No. 19, p. 2643, 2004.

124. Brown, P., K. Ishida, R. Kainuma, T. Kanomata, K. Neumann, K. Oikawa, B. Ouladdiaf and K. Ziebeck, "Crystal Structures and Phase Transitions in Ferromagnetic Shape Memory Alloys Based on Co–Ni–Al and Co–Ni–Ga", *Journal of Physics: Condensed Matter*, Vol. 17, No. 8, p. 1301, 2005.

125. Wang, H., Z. Liu, Y. Wang, X. Duan and G. Wu, "Microstructure of Martensitic Phase in the Co39ni33al28 Shape Memory Alloys Revealed by Transmission Electron Microscopy", *Journal of Alloys and Compounds*, Vol. 400, No. 1-2, pp. 145–149, 2005.

126. Luo, F., J. Chen, Y. Tao, K. Oikawa and K. Ishida, "Influence of Quenching Temperature on Martensitic Transformation and Magnetism of Co40. 5ni34al25.5 Alloy", *Xiyou Jinshu Cailiao Yu Gongcheng/Rare Metal Materials and Engineering*, Vol. 35, No. 6, pp. 917–920, 2006.

127. Liu, J. and J. Li, "Magnetic Force Microscopy Observations of Co–Ni–Ga and Co–Ni–Al Alloys with o-Phase Structures", *Scripta Materialia*, Vol. 55, No. 9, pp. 755–758, 2006.

128. Valiullin, A., S. Kositsin, I. Kositsina, N. Kataeva and V. Zavalishin, "Study of Ferromagnetic Co–Ni–Al Alloys with Thermoelastic L10 Martensite", *Materials Science and Engineering: A*, Vol. 438, pp. 1041–1044, 2006.

129. Liu, J. and J. Li, "Microstructure, Shape Memory Effect and Mechanical Properties of Rapidly Solidified Co–Ni–Al Magnetic Shape Memory Alloys", *Materials Science and Engineering: A*, Vol. 454, pp. 423–432, 2007.

130. Pons, J., E. Cesari, C. Seguí, F. Masdeu and R. Santamarta, "Ferromagnetic Shape Memory Alloys: Alternatives to Ni–Mn–Ga", *Materials Science and Engi-*

neering: A, Vol. 481, pp. 57–65, 2008.

131. Maziarz, W., J. Dutkiewicz, R. Santamarta and E. Cesari, "Microstructure Changes in Two Phase Beta+Gamma Co-Ni-Al Ferromagnetic Shape Memory Alloys in Relation to Al/Co Ratio", *The European Physical Journal Special Topics*, Vol. 158, No. 1, pp. 137–142, 2008.

132. Liu, Z., S. Yu, H. Yang, G. Wu and Y. Liu, "Phase Separation and Magnetic Properties of Co–Ni–Al Ferromagnetic Shape Memory Alloys", *Intermetallics*, Vol. 16, No. 3, pp. 447–452, 2008.

133. Maziarz, W., "Structure Changes of Co–Ni–Al Ferromagnetic Shape Memory Alloys After Vacuum Annealing and Hot Rolling", *Journal of Alloys and Compounds*, Vol. 448, No. 1-2, pp. 223–226, 2008.

134. Chatterjee, S., M. Thakur, S. Giri, S. Majumdar, A. Deb and S. De, "Transport, Magnetic and Structural Investigations of Co–Ni–Al Shape Memory Alloy", *Journal of Alloys and Compounds*, Vol. 456, No. 1-2, pp. 96–100, 2008.

135. Maziarz, W., J. Dutkiewicz, Ł. Rogal, J. Grzonka and E. Cesari, "Microstructure of Ball Milled and Compacted Co–Ni–Al Alloys From the Beta Range", *Journal of Microscopy*, Vol. 236, No. 2, pp. 143–148, 2009.

136. Kopeček, J., S. Sedláková-Ignácová, K. Jurek, M. Jarošová, J. Drahokoupil, P. Šittner and V. Novák, "Structure Development in Co38ni33al29 Ferromagnetic Shape Memory Alloy", *European Symposium on Martensitic Transformations*, p. 02013, EDP Sciences, 2009.

137. Morito, H., K. Oikawa, a. Fujita, K. Fukamichi, R. Kainuma and K. Ishida, "Large Magnetic-Field-Induced Strain in Co–Ni–Al Single-Variant Ferromagnetic Shape Memory Alloy", *Scripta Materialia*, Vol. 63, No. 4, pp. 379–382, 2010.

138. Kopeček, J., K. Jurek, M. Jarošová, J. Drahokoupil, S. Sedláková-Ignácová,

P. Šittner and V. Novák, "The Preparation of Oriented Samples of Ferromagnetic Shape Memory Alloy CoNiAl", *Iop Conference Series: Materials Science and Engineering*, Vol. 7, p. 012013, IOP, 2010.

139. Maziarz, W., J. Dutkiewicz, L. Lityńska-Dobrzyńska, R. Santamarta and E. Cesari, "Structure Investigations of Ferromagnetic Co-Ni-Al Alloys Obtained by Powder Metallurgy", *Journal of Microscopy*, Vol. 237, No. 3, pp. 374–378, 2010.

140. Kositsyna, I. I. and V. Zavalishin, "Study of Co-Ni-Al Alloys with Magnetically Controlled Shape Memory Effect", *Materials Science Forum*, Vol. 635, pp. 75–80, Trans Tech Publ, 2010.

141. Titenko, A., "Martensitic Transformations in Ferromagnetic Co-Ni-Al Alloy with Shape Memory Caused by Uniaxial Stretching", *Metallofizika I Noveishie Tekhnologii*, Vol. 34, No. 6, pp. 843–854, 2012.

142. Lu, J., H. Shi, S. Sedlakova-Ignacova, R. Espinoza, J. Kopeček, P. Sittner, B. Bártová and D. Schryvers, "Microstructure and Precipitates in Annealed Co38ni33al29 Ferromagnetic Shape Memory Alloy", *Journal of Alloys and Compounds*, Vol. 572, pp. 5–10, 2013.

143. Seiner, H., J. Kopeček, P. Sedlák, L. Bodnárová, M. Landa, P. Sedmák and O. Heczko, "Microstructure, Martensitic Transformation and Anomalies in C' Softening in Co–Ni–Al Ferromagnetic Shape Memory Alloys", *Acta Materialia*, Vol. 61, No. 15, pp. 5869–5876, 2013.

144. Singh, S., R. Roy, B. Mahato, M. Ghosh, A. Mitra and A. Panda, "Effect of Al Incorporation for Co on the Gamma-Beta Phase Boundary of Rapidly Solidified CoNiAl Ferromagnetic Shape Memory Alloys", *Journal of Magnetism and Magnetic Materials*, Vol. 368, pp. 379–383, 2014.

145. Pataky, G. J., E. Ertekin and H. Sehitoglu, "Elastocaloric Cooling Potential of NiTi, Ni2fega, and CoNiAl", *Acta Materialia*, Vol. 96, pp. 420–427, 2015.

146. Faran, E. and D. Shilo, "Ferromagnetic Shape Memory Alloys—Challenges, Applications, and Experimental Characterization", *Experimental Techniques*, 2015.

147. Ju, J., F. Xue and L.-X. Sun, "Structure and Performance Changes of Ni-Co-Al Shape Memory Alloys in Relation to Co/Al Atomic Ratio", *Journal of Iron and Steel Research International*, Vol. 22, No. 7, pp. 652–656, 2015.

148. Dağdelen, F., T. Malkoç, M. Kök and E. Ercan, "Comparison of the Transformation Temperature, Microstructure and Magnetic Properties of Co-Ni-Al and Co-Ni-Al-Cr Shape Memory Alloys", *The European Physical Journal Plus*, Vol. 131, No. 6, pp. 1–6, 2016.

149. Long, J., K. Li, F. Chen, M. Yi, Y. Du, B. Lu, Z. Zhang, Y. Wang, K. Cheng and K. Zhang, "Microstructure Evolution of Wc Grains in Wc–Co–Ni–Al Alloys: Effect of Binder Phase Composition", *Journal of Alloys and Compounds*, Vol. 710, pp. 338–348, 2017.

150. Ju, J., L. Yang, S. Hao, Q. Mao, S. Lou and H. Liu, "Microstructure, Martensite Transition and Mechanical Properties Investigations of Polycrystalline Co-Ni-Al Alloys with Er Doping", *Journal of Materials Engineering and Performance*, Vol. 26, No. 3, pp. 1062–1068, 2017.

151. Ju, J., H. Liu, L. Shuai, Z. Liu, Y. Kang, C. Yan and H. Li, "Martensite Transformation and Mechanical Properties of Polycrystalline Co-Ni-Al Alloys with Gd Doping", *Metals*, Vol. 8, No. 10, p. 848, 2018.

152. Hossain, M. S., P. Gokul, B. Pal and P. Mukhopadhyay, "Correlation of Dynamic Elastic Properties of a Heat-Treated CoNiAl Alloy System with It's Microstructural Changes", *Shape Memory and Superelasticity*, Vol. 5, No. 4, pp. 468–475, 2019.

153. Hossain, M. S., T. Ghosh, B. R. Kanth and P. K. Mukhopadhyay, "Effect of Annealing on the Structural and Magnetic Properties of CoNiAl Fsma", *Crystal*

Research and Technology, Vol. 54, No. 4, p. 1800153, 2019.

154. Zhou, F., Y. Zhou, J. Wang, J. Liang, H. Gao and M. Kang, "Enlightening From Gamma, Gamma' and Beta Phase Transformations in Al-Co-Ni Alloy System: A Review", *Current Opinion in Solid State and Materials Science*, Vol. 23, No. 6, p. 100784, 2019.

155. Wang, C., F. Zhou, Y. Zhou, M. Wang, J. Liang, J. Wang and B. Gan, "Investigations of Strength and Ductility in Ni-XCo-10Al Alloys Via Discontinuous Precipitation", *Materials Characterization*, Vol. 163, p. 110318, 2020.

156. Bagchi, A., S. Sarkar, S. Bysakh, C. S. Tiwary, M. S. Hossain, S. Sarkar and P. Mukhopadhyay, "Microstructural Evolution and Its Outcome on the Photo Induced Micro Actuation Effect and Mechanical Properties of Copper Doped Co-Ni-Al FSMA", *Journal of Alloys and Compounds*, Vol. 846, p. 156432, 2020.

157. Arputhavalli, G. J., S. Agilan, M. Ray, D. Thangaraju, R. Marnadu, J. Chandrasekaran, K. V. Chandekar, M. Shkir, S. Jebasingh and M. Dinesh, "Post-Annealing Effects on Structural and Magnetic Properties of Pulsed Laser Deposition Grown Co–Ni–Al Ferromagnetic Shape Memory Alloys Thin Films", *Solid State Sciences*, Vol. 111, p. 106493, 2021.

158. Wu, Y., A. Ojha, L. Patriarca and H. Sehitoglu, "Fatigue Crack Growth Fundamentals in Shape Memory Alloys", *Shape Memory and Superelasticity*, Vol. 1, No. 1, pp. 18–40, 2015.

159. Sgambitterra, E., C. Maletta, F. Furgiuele and H. Sehitoglu, "Fatigue Crack Propagation in [0 1 2] NiTi Single Crystal Alloy", *International Journal of Fatigue*, Vol. 112, pp. 9–20, 2018.

160. Jaglinski, T., P. Frascone, B. Moore, D. Stone and R. Lakes, "Internal Friction Due to Negative Stiffness in the Indium–Thallium Martensitic Phase Transformation", *Philosophical Magazine*, Vol. 86, No. 27, pp. 4285–4303, 2006.

161. Mutlu, F., G. Anlaş and H. Şehitoglu, “Crack INiTiation Angle in Single Crystal Shape Memory Alloys”, *Shape Memory and Superelasticity*, Vol. 9, No. 4, pp. 1–10, 2023.

APPENDIX A: COPYRIGHTS



This is a License Agreement between Fatma MUTLU ("User") and Copyright Clearance Center, Inc. ("CCC") on behalf of the Rightsholder identified in the order details below. The license consists of the order details, the Marketplace Permissions General Terms and Conditions below, and any Rightsholder Terms and Conditions which are included below.

All payments must be made in full to CCC in accordance with the Marketplace Permissions General Terms and Conditions below.

Order Date	24-May-2023	Type of Use	Republish in a thesis/dissertation
Order License ID	1358125-1		
ISBN-13	978-1-4200-7966-1	Publisher	CRC Press; Woodhead Pub
		Portion	Chart/graph/table/figure

LICENSED CONTENT

Publication Title	Shape memory alloys for biomedical applications	Country	United Kingdom of Great Britain and Northern Ireland
Author/Editor	Yoneyama, Takayuki., Miyazaki, Shuichi.	Rightsholder	Elsevier Science & Technology Journals
Date	01/01/2009	Publication Type	Book
Language	English		

REQUEST DETAILS

Portion Type	Chart/graph/table/figure	Distribution	Worldwide
Number of Charts / Graphs / Tables / Figures Requested	1	Translation	Original language of publication
Format (select all that apply)	Print, Electronic	Copies for the Disabled?	No
Who Will Republish the Content?	Academic institution	Minor Editing Privileges?	Yes
		Incidental Promotional Use?	No
Duration of Use	Life of current edition	Currency	USD
Lifetime Unit Quantity	Up to 499		
Rights Requested	Main product, any product related to main product, and other compilations/derivative products		

NEW WORK DETAILS

Title	CRACK INITIATION AND GROWTH IN SHAPE MEMORY ALLOYS	Institution Name	BOGAZICI UNIVERSITY
		Expected Presentation Date	2023-07-31
Instructor Name	FATMA MUTLU		

ADDITIONAL DETAILS

Order Reference Number	N/A	The Requesting Person/Organization to Appear on the License	Fatma MUTLU

REQUESTED CONTENT DETAILS

Title, Description or Numeric Reference of the Portion(s)	Figure 2.1	Title of the Article/Chapter the Portion Is From	Mechanical properties of shape memory alloys
Editor of Portion(s)	H. Hosoda and T. Inamura	Author of Portion(s)	Yoneyama, Takayuki.; Miyazaki, Shuichi.
Volume / Edition	2009		
Page or Page Range of Portion	21	Issue, if Republishing an Article From a Serial	N/A
		Publication Date of Portion	2009-01-01

RIGHTSHOLDER TERMS AND CONDITIONS

Figure A.1. Proof of permission for reuse of Figure 1.1



This is a License Agreement between Fatma Mutlu ("User") and Copyright Clearance Center, Inc. ("CCC") on behalf of the Rightsholder identified in the order details below. The license consists of the order details, the Marketplace Permissions General Terms and Conditions below, and any Rightsholder Terms and Conditions which are included below.

All payments must be made in full to CCC in accordance with the Marketplace Permissions General Terms and Conditions below.

Order Date	23-May-2023	Type of Use	Republish in a thesis/dissertation
Order License ID	1357812-1		
ISBN-13	978-1-4200-7966-1	Publisher	CRC Press; Woodhead Pub
		Portion	Chart/graph/table/figure

LICENSED CONTENT

Publication Title	Shape memory alloys for biomedical applications	Country	United Kingdom of Great Britain and Northern Ireland
Author/Editor	Yoneyama, Takayuki., Miyazaki, Shuichi.	Rightsholder	Elsevier Science & Technology Journals
Date	01/01/2009	Publication Type	Book
Language	English		

REQUEST DETAILS

Portion Type	Chart/graph/table/figure	Distribution	Worldwide
Number of Charts / Graphs / Tables / Figures Requested	1	Translation	Original language of publication
Format (select all that apply)	Print, Electronic	Copies for the Disabled?	No
Who Will Republish the Content?	Academic institution	Minor Editing Privileges?	No
		Incidental Promotional Use?	No
Duration of Use	Life of current edition	Currency	USD
Lifetime Unit Quantity	Up to 499		
Rights Requested	Main product, any product related to main product, and other compilations/derivative products		

NEW WORK DETAILS

Title	CRACK INITIATION AND GROWTH IN SHAPE MEMORY ALLOYS	Institution Name	Bogazici University
		Expected Presentation Date	2023-07-31
Instructor Name	Fatma Mutlu		

ADDITIONAL DETAILS

Order Reference Number	N/A	The Requesting Person/Organization to Appear on the License	Fatma Mutlu

REQUESTED CONTENT DETAILS

Title, Description or Numeric Reference of the Portion(s)	Chapter 1, Figure 1.1	Title of the Article/Chapter the Portion Is From	Shape memory effect and superelasticity in Ti-Ni alloys
Editor of Portion(s)	Prof S. Miyazaki, Dr RL Sachdeva	Author of Portion(s)	Yoneyama, Takayuki.; Miyazaki, Shuichi.
Volume / Edition	2009	Issue, if Republishing an Article From a Serial	N/A
Page or Page Range of Portion	5	Publication Date of Portion	2009-01-01

RIGHTSHOLDER TERMS AND CONDITIONS

Figure A.2. Proof of permission for reuse of Figure 1.3

CCC Marketplace

This is a License Agreement between Fatma Mutlu ("User") and Copyright Clearance Center, Inc. ("CCC") on behalf of the Rightsholder identified in the order details below. The license consists of the order details, the Marketplace Permissions General Terms and Conditions below, and any Rightsholder Terms and Conditions which are included below.

All payments must be made in full to CCC in accordance with the Marketplace Permissions General Terms and Conditions below.

Order Date	25-May-2023	Type of Use	Republish in a thesis/dissertation
Order License ID	1358757-1		
ISBN-13	9781441942975	Publisher	Springer
		Portion	Chart/graph/table/figure

LICENSED CONTENT

Publication Title	Shape memory alloys : modeling and engineering applications	Country	United States of America
		Rightsholder	Springer
		Publication Type	Book
Author/Editor	Lagoudas, Dimitris C.	URL	http://rave.ohiolink.edu/ebooks/ebc/9780387476858
Date	01/01/2008		
Language	English		

REQUEST DETAILS

Portion Type	Chart/graph/table/figure	Distribution	Worldwide
Number of Charts / Graphs / Tables / Figures Requested	2	Translation	Original language of publication
Format (select all that apply)	Print, Electronic	Copies for the Disabled?	No
Who Will Republish the Content?	Academic institution	Minor Editing Privileges?	Yes
		Incidental Promotional Use?	No
Duration of Use	Life of current and all future editions	Currency	USD
Lifetime Unit Quantity	Up to 499		
Rights Requested	Main product, any product related to main product, and other compilations/derivative products		

NEW WORK DETAILS

Title	CRACK INITIATION AND GROWTH IN SHAPE MEMORY ALLOYS	Institution Name	Bogazici University
		Expected Presentation Date	2023-07-31
Instructor Name	Fatma Mutlu		

ADDITIONAL DETAILS

Order Reference Number	N/A	The Requesting Person/Organization to Appear on the License	Fatma Mutlu

REQUESTED CONTENT DETAILS

Title, Description or Numeric Reference of the Portion(s)	Figure 1.4 and 1.5	Title of the Article/Chapter the Portion Is From	Introduction to shape memory alloys
Editor of Portion(s)	P. K. Kumar and D. C. Lagoudas	Author of Portion(s)	Lagoudas, Dimitris C.
Volume / Edition	2008	Issue, if Republishing an Article From a Serial	N/A
Page or Page Range of Portion	7	Publication Date of Portion	2008-01-01

RIGHTSHOLDER TERMS AND CONDITIONS

Figure A.3. Proof of permission for reuse of Figure 1.2 and 1.4

CCC Marketplace

This is a License Agreement between Boğaziçi University ("User") and Copyright Clearance Center, Inc. ("CCC") on behalf of the Rightsholder identified in the order details below. The license consists of the order details, the Marketplace Permissions General Terms and Conditions below, and any Rightsholder Terms and Conditions which are included below.

All payments must be made in full to CCC in accordance with the Marketplace Permissions General Terms and Conditions below.

Order Date	26-May-2023	Type of Use	Republish in a thesis/dissertation
Order License ID	1358996-1		
ISBN-13	9781441942975	Publisher	Springer
		Portion	Chart/graph/table/figure

LICENSED CONTENT

Publication Title	Shape memory alloys : modeling and engineering applications	Country	United States of America
		Rightsholder	Springer
		Publication Type	Book
Author/Editor	Lagoudas, Dimitris C.	URL	http://rave.ohiolink.edu/ebooks/ebc/9780387476858
Date	01/01/2008		
Language	English		

REQUEST DETAILS

Portion Type	Chart/graph/table/figure	Distribution	Worldwide
Number of Charts / Graphs / Tables / Figures Requested	2	Translation	Original language of publication
Format (select all that apply)	Print, Electronic	Copies for the Disabled?	No
Who Will Republish the Content?	Author of requested content	Minor Editing Privileges?	Yes
		Incidental Promotional Use?	No
Duration of Use	Life of current and all future editions	Currency	USD
Lifetime Unit Quantity	Up to 499		
Rights Requested	Main product, any product related to main product, and other compilations/derivative products		

NEW WORK DETAILS

Title	CRACK INITIATION AND GROWTH IN SHAPE MEMORY ALLOYS	Institution Name	BOGAZICI UNIVERSITY
		Expected Presentation Date	2023-07-31
Instructor Name	FATMA MUTLU		

ADDITIONAL DETAILS

Order Reference Number	N/A	The Requesting Person/Organization to Appear on the License	Boğaziçi University

REQUESTED CONTENT DETAILS

Title, Description or Numeric Reference of the Portion(s)	Figures 1.6 and 1.7	Title of the Article/Chapter the Portion Is From	Introduction to shape meory alloys
Editor of Portion(s)	PK Kumar and DC Lagoudas	Author of Portion(s)	Lagoudas, Dimitris C.
Volume / Edition	2008	Issue, if Republishing an Article From a Serial	N/A
Page or Page Range of Portion	8,9	Publication Date of Portion	2008-01-01

RIGHTSHOLDER TERMS AND CONDITIONS

Figure A.4. Proof of permission for reuse of Figure 1.5



This is a License Agreement between Fatma Mutlu ("User") and Copyright Clearance Center, Inc. ("CCC") on behalf of the Rightsholder identified in the order details below. The license consists of the order details, the Marketplace Permissions General Terms and Conditions below, and any Rightsholder Terms and Conditions which are included below.

All payments must be made in full to CCC in accordance with the Marketplace Permissions General Terms and Conditions below.

Order Date	23-May-2023	Type of Use	Republish in a thesis/dissertation
Order License ID	1357822-1		
ISSN	1369-7021	Publisher	ELSEVIER BV
		Portion	Chart/graph/table/figure

LICENSED CONTENT

Publication Title	Materials today	Rightsholder	Elsevier Science & Technology Journals
Article Title	Crack interaction with microstructure	Publication Type	Journal
Author/Editor	European Materials Research Society.	Start Page	34
		End Page	44
Date	01/01/1998	Issue	9
Language	English	Volume	10
Country	Netherlands		

REQUEST DETAILS

Portion Type	Chart/graph/table/figure	Distribution	Worldwide
Number of Charts / Graphs / Tables / Figures Requested	1	Translation	Original language of publication
Format (select all that apply)	Print, Electronic	Copies for the Disabled?	No
Who Will Republish the Content?	Academic institution	Minor Editing Privileges?	Yes
		Incidental Promotional Use?	No
Duration of Use	Life of current edition	Currency	USD
Lifetime Unit Quantity	Up to 499		
Rights Requested	Main product, any product related to main product, and other compilations/derivative products		

NEW WORK DETAILS

Title	CRACK INITIATION AND GROWTH IN SHAPE MEMORY ALLOYS	Institution Name	Bogazici University
		Expected Presentation Date	2023-07-31
Instructor Name	Fatma Mutlu		

ADDITIONAL DETAILS

Order Reference Number	N/A	The Requesting Person/Organization to Appear on the License	Fatma Mutlu

REQUESTED CONTENT DETAILS

Title, Description or Numeric Reference of the Portion(s)	Figure 1	Title of the Article/Chapter the Portion Is From	Crack interaction with microstructure
Editor of Portion(s)	Kumar, Sharvan; Curtin, William A.	Author of Portion(s)	Kumar, Sharvan; Curtin, William A.
Volume / Edition	10	Issue, if Republishing an Article From a Serial	9
Page or Page Range of Portion	34-44	Publication Date of Portion	2007-09-01

Figure A.5. Proof of permission for reuse of Figure 1.8